EXPLORATIONS INTO THE LIFE OF DICTYOSTELIUM DISCOIDEUM.

A Dissertation

Presented to the Faculty of the Graduate School

of Cornell University

in Partial Fulfillment of the Requirements for the Degree of

Doctor of Philosophy

by

Albert Johann Bae

January 2011

EXPLORATIONS INTO THE LIFE OF DICTYOSTELIUM DISCOIDEUM.

Albert Johann Bae, Ph.D.

Cornell University 2011

In this dissertation, we explore several aspects of the *Dictyostelium discoideum* life cycle: growth, aggregation, and differentiation:

We present experiments that question the conventional wisdom that vegetative *D. discoideum* are solitary individuals. We examine evidence – the cell density dependent transition from lag to exponential growth – which suggests that growth is stimulated by cell to cell interactions. Using a conditioned medium assay, we rule out the possibility that this interaction is through growth factors. Instead, we find that the interactions are short ranged.

Next, we examine chemotactic, aggregation-stage cells. Using a microfluidic platform for cell stimulation, we investigate the timing of the biochemical signals involved in direction sensing, and we attempt to alter this timing. We flatten cells to various degrees and apply an external pulse of chemoattractant. The response is then monitored by imaging a fluorescent protein (PH_{CRAC}-GFP or LimE-GFP) which translocates to the leading edge of the cell. We expect a dependence between the response time and the area of the cell, since the size should affect the time it takes for biochemical messengers to diffuse across the cell. The results were not definitive, because of the large variability in time it takes for the cell to respond to a signal.

The large variability might be due to variations between the time the chemical signal is applied and the time it reaches the cell. To evaluate this possibility, we apply the theory of G.I. Taylor [172] and R. Aris [7] to answer the question of how quickly we are able to apply chemical signals to the target. We show that our platform for cell stimulation is the fastest available, and we rule out the pos-

sibility that the variability in the response times is due to experimental setup. Rather, the source of variability must be biological, either intrinsic to each cell, or due to variability between cells (individuality).

Recently, it was shown that *D. discoideum* cells are also capable of swimming chemotactically [13]. Using low Reynolds number flow simulations, we find evidence that supports the claim that the mechanisms employed by *D. discoideum* to swim are the same mechanisms employed when they crawl.

Finally, we conclude our investigations by examining how *D. discoideum* sort out into regions of prestalk cells and prespore cells. Using a microfluidic flattening device with cells that express a fluorescent protein (CbpD::GFP) only if they are prestalk, we find indications that cell sorting is intrinsically a three dimensional process, as cell sorting was never observed in monolayer aggregates.

BIOGRAPHICAL SKETCH

Albert Johann Bae was born in Vancouver, WA in June, 1981, the youngest of three siblings. He received a Bachelors of Science degree in Physics with a minor in Mathematics from Portland State University in June of 2003. Shortly thereafter, he began his graduate studies at Cornell University. In his free time, he enjoys playing the cello, shooting pocket billiards, and if he can find a good table, playing air hockey.

To my family and friends.

ACKNOWLEDGMENTS

I thank my advisors Eberhard Bodenschatz and Carl Franck for their guidance over the years. From them, I have learned a great deal about what it means to be a scientist. Carl supervised the first half of my graduate work. His good humor and wise counsel helped me through many trying times in my teaching, research, and personal life. Eberhard, who supervised me for the second half, provided me with independence to grow as a scientist. From Eberhard, I learned how to defend my work, and I thank him for enduring my often intense pessimism. I appreciate the deep-seated enthusiasm for science, shared by both Eberhard and Carl, and I am grateful for the many open discussions we have had together.

I thank James Sethna and Carsten Beta for the advice they have given me at various stages of my studies.

I thank Katharina Schneider and Barbara Kaseman for their valuable biological expertise. They run an first rate cell culture laboratory. Without their help, my work would have been much more difficult. I thank Arthur Kubitzek and Andreas Renner for their technical assistance. Also, I am grateful to Angela Meister for her masterful handling of administrative issues.

I thank my colleagues from Cornell: Ben, Duane, and Sharvari; from the Max Planck Institute for Dynamics and Self-Organization: Gabriel A., Greg, Fabio, Azam, Mathieu, Noriko, Walter, Ewe Wei, Gabriel S., Matthias, Mireia, Stephan, Christian, Hengdong and Robert; and from both institutions: Kelken, Amgad, Dario, Haitao and Danica. I am grateful for the time I spent with these wonderful individuals.

I thank my parents, my sisters, and my friends for their love and support.

TABLE OF CONTENTS

LIST OF TABLES

LIST OF FIGURES

CHAPTER 1

INTRODUCTION

The research presented in this dissertation covers a wide range of stages in the life cycle of *Dictyostelium discoideum*. Therefore, let us begin with a brief introduction to the organism:

1.1 The life cycle of *D. discoideum*

Dictyostelium discoideum is an amoeba, $\sim 15\ \mu$m in diameter, which can be found growing in forest soils as well as in many research laboratories. *D. discoideum* typically feeds on bacteria and divides mitotically every 4 hours. Axenic strains have also been isolated. These strains feed on sterile culture medium with a doubling time of approximately 8-12 hours [56, 62, 169]. In nutrient rich environments, *D. discoideum* grow as individuals.[1] When nutrients are depleted, groups of $1.1\times10^4 - 2.7\times10^6$ cells [28] undergo a remarkable transition from unicellularity to multicellularity, ultimately forming a fruiting body that is resistant to the harsh, nutrient-free environment [100]. See figure 1.1.

When starved, each cell downregulates the genes required for growth and upregulates genes used in development. Around four hours into development, the cells enter the aggregation phase. They communicate with each other using a chemical signal relay: Developed cells will spontaneously secrete 3'-5'-cyclic adenosine monophosphate (cAMP), which diffuses outward, towards neighboring cells. When this extracellular cAMP binds to the receptors of the neighboring cells, the cells are stimulated to produce and secrete more cAMP [178, 133]. This cAMP, in turn, diffuses outward and the signal relay continues.

[1] See chapter 3 for a refutation of this commonly accepted viewpoint.

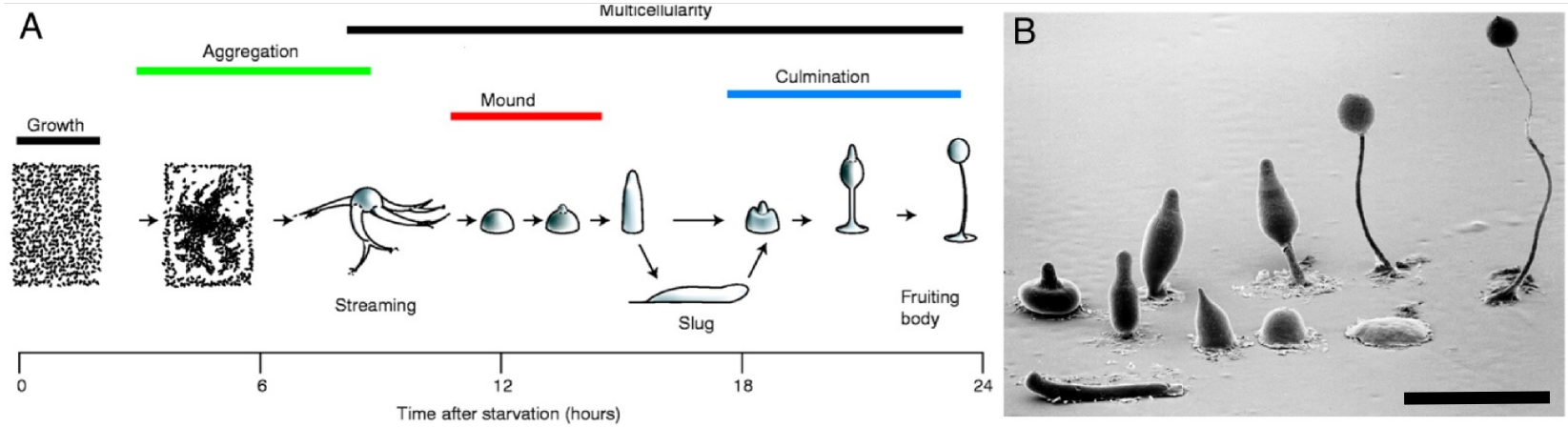

Figure 1.1: (a) Illustration of the stages of *Dictyostelium* development. Reproduced with permission from [38], Copyright (2001), The Company Of Biologists Ltd. (b) SEM images of these develepmental stages. Scale bar ≈ 1 mm. Copyright, M. J. Grimson and R. L. Blanton, Biological Sciences Electron Microscopy Laboratory, Texas Tech University.

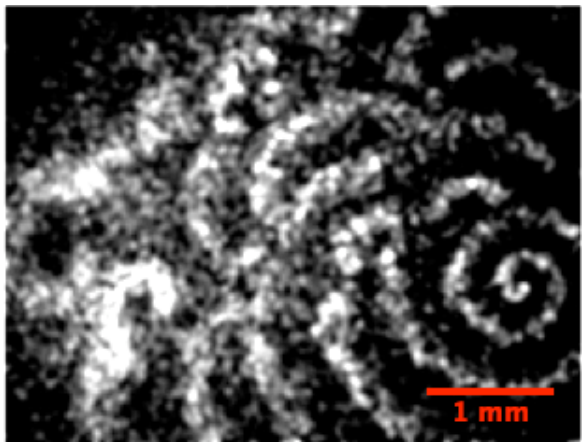

Figure 1.2: Spiral waves propagating in a field of aggregating *D. discoideum*. Spiral waves were visualized by taking the absolute value of the difference between intensity values of two bright field microscopy images taken a minute apart. Brighter values correspond to regions of changing intensity, which in turn correspond to regions where the cells are moving in response to cAMP. This image was produced in collaboration with Duane Loh.

This relay process is responsible for creating a traveling wave in the concentration of extracellular cAMP. In front of the wave, the cells have not yet been stimulated to secrete cAMP, so there, the concentration is low. On the wavefront, the cells have just recently been stimulated to generate cAMP, so the concentration is rising. Behind the wavefront there is a "waveback." Here are cells that have been stimulated, but have adapted to high levels of cAMP. These adapted cells have reduced their secretion of cAMP.[2] Extracellular cAMP phosphodiesterase, an enzyme secreted by these amoeba, degrades the cAMP. As the concentration of cAMP decreases, the cells behind the wave eventually de-adapt, so that another wavefront can pass.

We can recast this signaling relay in the language of excitable media: (i) the cells in front of the wave are **excitable**, (ii) the cells at the wavefront which have been stimulated to make cAMP are **excited**, and (iii) the cells that have adapted

[2]The biochemical details of this adaptation process are still mostly unknown [155].

to high levels of cAMP are **refractory**. The hallmark of an excitable medium is that it can support propagating waves of excitation, but between the passing of successive wavefronts, there is a refractory period during which the medium is unexcitable. Similar to what is seen in excitable systems like the BZ reaction [204, 197] and heart tissue [2], the geometries of the cAMP wavefronts are spirals and targets. Figure 1.2 shows a nice example of a spiral wave that we observed in a Petri dish of aggregating *D. discoideum*.

Developed cells are chemotactic, meaning that cells will move towards higher concentrations of cAMP. So when a wavefront passes by, the cells will walk up the gradient, towards the the origin of the wave – the aggregation center. After the wavefront passes by, it is followed by a waveback, in which the gradient is reversed. One may expect that the cells should reverse their direction of motion during this period, yet experimentally, it has been shown that they do not [163].[3]

As waves pass by, with a periodicity of around 6 min,[4] the cells crawl closer to the aggregation center, and closer to each other. After approximately 20 periods (2 hours), the cells come into end-to-end contact with each other, forming a loose aggregate. The configuration consists of several streams (or strings) which converge at the aggregation center [45, 94]. At this point in time – approximately 6-8 hours into development – cells begin expressing cell-cell adhesion glycoproteins [22, 126, 105]. Over the next couple of hours, the streams shorten as the cells swirl towards the center. A slime sheath, primarily composed of cellulose, forms on the surface [63], and the aggregate becomes a mound.

[3]The gradient in the waveback is weaker, but occurs for a longer duration. If the cells are chemotactically responsive to the waveback, one might expect that the cells walk longer in the wrong direction than the right direction. This is known as the chemotactic paradox [81, 163].

[4]This period varies a bit, depending on the development time and the cell line [132, 154, 155].

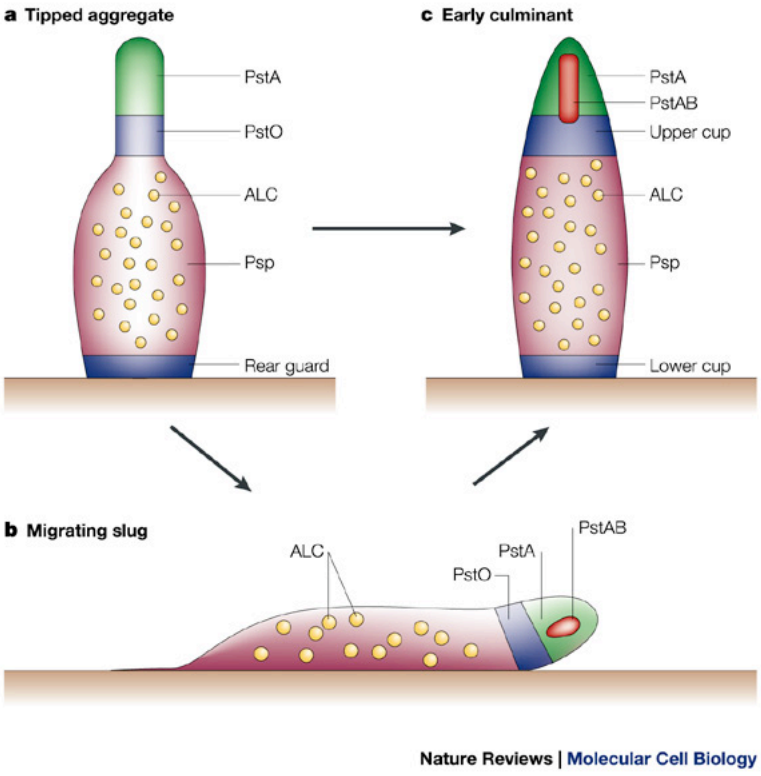

Figure 1.3: Organization of prespore and prestalk cells in the (a) tipped aggregate, (b) migrating slug, and (c) early culminant stages of development. Reprinted by permission from Macmillan Publishers Ltd: *Nature Reviews Molecular Cell Biology*, [34], copyright (2004).

In the mound stage of *D. discoideum* development, cells differentiate into two main types of cells, (i) prespore (PspA) and (ii) prestalk (PstA, PstO, PstAB) cells, in a well-controlled, 80:20 ratio. Initially these cells appear to be randomly distributed throughout the aggregate (salt and pepper pattern). Whether a cell becomes a prespore or prestalk cell is influenced by which phase in the cell cycle it was in when the cell's nutrients were removed [34, 74, 192]. As development progresses, the cells in the mound move and sort into regions of prestalk and prespore cells, and at around 14 hours into development, the sorted prestalk cells form the apical tip of the mound. See figures 1.1a and 1.3a.

Several mechanisms for the sorting of cells have been proposed. Sorting may be driven by chemotaxis towards a chemical signalling center [48, 187]. The prestalk cells have a higher chemotactic velocity, and therefore accumulate at the center, leaving the slower prespore cells in the periphery. In the differential adhesion hypothesis, the prestalk and prespore cells have different intercellular adhesiveness, and when two similar cells run into each other, they stick together [90, 118]. A more recent proposal is that difference in cell motility is what drives sorting [184].

Over the next few hours, the tipped aggregate elongates into a finger. This finger may topple over to form a migrating slug, ~ 1 mm in length and ~ 0.1 mm in diameter. This slug is phototactic [145, 58] and thermotactic [26, 196]. Presumably, the motile response to light and heat is an effort to migrate upwards, from inside the soil towards the surface of the forest floor, where the probability of spore dispersal is optimal [27].

The front of the slug is composed of prestalk cells. The rest of the slug consists primarily of prespore cells, with a few anterior-like (prestalk) cells. See figure 1.3b. The regulation of the cell types is remarkable. If the anterior and posterior ends of the slug are surgically separated, then each half will re-differentiate to restore the proper, 80:20 proportion of prestalk to prespore cells [145, 144].

After the slug's migration ceases,[5] the process of culmination begins. The slug stands up to form the early culminant. The tip of this culminant consists of three types of prestalk cells: PstO, PstA, and PstAB. PstO cells can differentiate into PstA cells. PstA cells can differentiate into PstAB cells. Finally, PstAB cells can differentiate into stalk cells which deposit cellulose, become vacuolated, and die [117]. See figure 1.3c to view the location of these cells.

[5]Amazingly, *Dictyostelium* slugs are capable of migrating for 10 days or longer, depending on the environmental conditions, e.g. temperature, lighting, salt concentration [130, 162]!

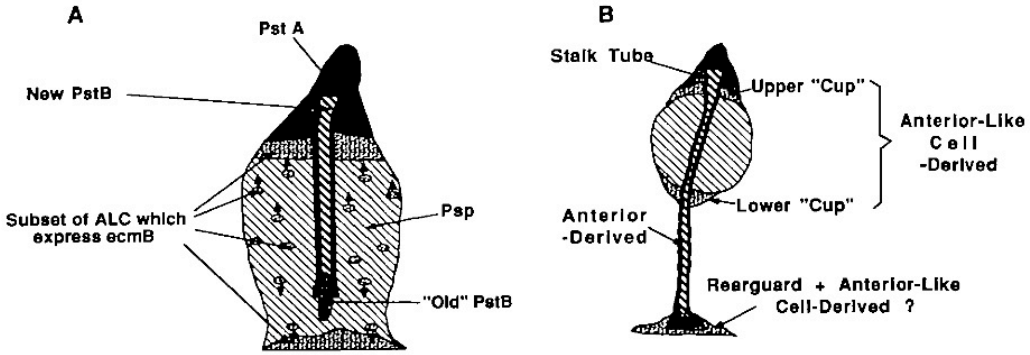

Figure 1.4: Illustration of the culmination process. Note that the cells labeled here as PstB are actually PstAB cells. Reproduced with permission from [89], Copyright (1991), The Company Of Biologists Ltd.

In the tip, PstAB cells form a funnel shaped region along the axis. When PstA cells enter this region, they differentiate into PstAB cells. As new PstAB cells are formed, older cells move downward, forming the stalk tube, which pushes into the region of prespore cells called the sorus (figure 1.4a). PstO cells in the upper cup differentiate in order to replenish the PstA cells which are being converted into PstAB cells. Eventually, this stalk tube grows through the prespore region and plants itself onto the substrate. Now, as the stalk tube grows longer, the sorus is pushed upwards (figure 1.4b), until the structure is ~ 2 mm tall. The prespore cells sporulate, and the harsh environment resistant fruiting body is complete. [89, 117]

The spores are dispersed by rainwater or by birds, insects, and nematodes, who feast on the fruiting bodies, but can not digest the spores [29]. If a spore lands in a damp, warm, and nutrient-rich location, then the spore will germinate, and the life cycle of *D. discoideum* begins again.

1.2 Overview

First, in chapter 2, we introduce the cell culture and microfluidic methods used throughout this work. Following this, experiments are presented in the order according to which stage of the *D. discoideum* life cycle is being explored:

In chapter 3, we discuss some experiments that questioned the conventional wisdom that growing, vegetative *D. discoideum* are solitary individuals. We examine evidence – the cell density dependent transition from lag to exponential growth – that indicated that growing cells actually do interact with each other. Then, using a conditioned medium assay, we investigated which mode of communication might be used.

Next, we examine experiments on chemotactic, aggregation-stage cells. These cells will migrate up gradients of chemoattractant, where the concentration difference between the front and back of the cell is as low as 2% [120, 164]. How these cells are capable of chemotaxing in such gradients is a topic of active research. Therefore, provided in chapter 4 is a primer on the two major aspects of chemotaxis: (i) direction sensing, i.e. how the cell's internal compass aligns itself to the external gradient of chemoattractant and (ii) motility, i.e. how the cell propels itself forward. We review the known biochemical pathways, and present several models for direction sensing. We also briefly review the theories of cell motility.

In chapter 5, we investigate the timing of the biochemical signals involved in direction sensing, and present attempts to alter this timing. Biochemical messengers diffuse from the cell front to the cell back. Consequently, the timing of direction sensing should depend on the cell's area. We flattened cells to various degrees and applied an external pulse of chemoattractant. The response was then monitored by imaging a fluorescent protein (PH_{CRAC}-GFP or LimE-GFP)

which translocates to the leading edge of the cell. We expected to see a systematic dependence between the response time and the size of the cell, and from this dependence, we hoped to evaluate the various models for direction sensing. The results were not definitive, because of the large variability in time it takes for the cell to respond to a signal. Was this variability due to issues with the experimental setup?

In chapter 6, we apply the theory of G.I. Taylor [172] and R. Aris [7] to answer the question of how quickly we were able to apply chemical signals to the target. In this chapter, we also demonstrate that our platform for stimulating cells is the fastest available, and we rule out the possibility that the variations seen in chapter 5 were due to the setup. Rather, the source of variability must have been biological, either intrinsic to a cell, or due to individuality between cells.

The conventional mode of movement for the chemotactic amoebae is crawling. Recently, N. P. Barry and M. S. Bretscher showed that *D. discoideum* cells are also capable of swimming chemotactically [13]. The mechanisms we humans employ for swimming are very different from those we use when we crawl. For *D. discoideum*, however, swimming and crawling are likely to be part of the same motility program. In chapter 7, we show that indeed, the shape changes generated by a crawling *D. discoideum* cell are consistent with swimming.

Finally, in chapter 8 we look at the mound stage. Using a microfluidic flattening device with cells that expressed a fluorescent protein (CbpD::GFP) only if they are prestalk, we investigated the cell sorting process in flattened mounds. These experiments indicate that cell sorting is intrinsically a three dimensional process, as cell sorting was never observed in monolayer aggregates. We discuss a theory by M.S. Hutson et al. that sheds some light on why this may be the case [82].

CHAPTER 2

GENERAL METHODS AND MATERIALS

2.1 Cell culture and development

D. discoideum was grown at room temperature[1] in HL-5 (ForMedium Ltd., 14 g/L peptone, 7 g/L yeast extract, 13.5 g/L glucose, 0.5 g/L KH_2PO_4, 0.5 g/L Na_2HPO_4, [189]) on Petri dishes or in a suspension shaken at 150 rpm. Strains with selection markers were supplemented with the antibiotics genetecin (G418) and/or blasticidin. Cells were maintained in the exponential growth phase (10^4-10^6 cells/mL), and to ensure that the cells don't mutate over time, the cell lines were restored from frozen (-80^o C) stock every month.

D. discoideum used in the experiments of chapter 5 (chemotactic response time) was developed to the aggregation stage on 10 cm Petri dishes. The supernatent HL-5 was removed from a confluent culture. Then, 5 mL of phosphate buffer (pH=6) was gently pipetted onto the dish so that the cells were not rinsed away. The dish was then gently agitated to mix the buffer with the residual HL-5. The supernatent was exchanged again with 5 mL of phosphate buffer. Next, 3.5 mL of supernatent was removed, leaving behind a thin layer of buffer. The cells were then allowed to develop for 7 hours, after which the cells were rinsed off the dish to be used in an experiment.

D. discoideum used in the experiments of subsequent chapters was developed in shaken suspension. Cells were grown in an exponential phase shaking culture to 2×10^6 cells/mL. This culture was centrifuged in a Falcon tube, concentrating into a pellet at the bottom. Using a pipette, the supernatent was

[1]The experiments described in chapter 3 were conducted in the laboratory of C. Franck, where the room temperature was maintained at 19^o C. The experiments described in subsequent chapters took place in the laboratory of E. Bodenschatz, where the temperature was maintained at 22^o C.

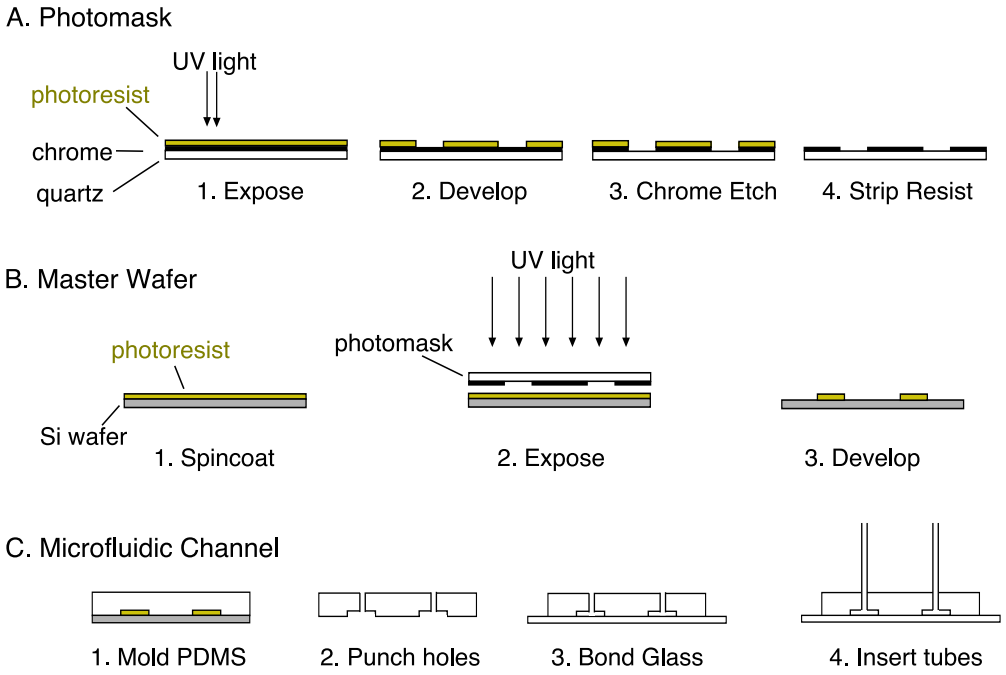

Figure 2.1: Soft Lithography, a side view: (a) generation of the photomask, (b) master wafer production and (c) construction of a microfludic channel. Figure adapted from [176].

removed and replaced with phosphate buffer. The tube was agitated to resuspend the cells. This cell wash was repeated three times. The cell suspension was then placed in an Erlenmeyer flask on the orbital shaker. To induce the cells to develop, a pulse of 50 nM cAMP was supplied every 6 minutes via a peristaltic pump [35, 198]. Cells were developed for 5 hours and then washed once more before they were used in an experiment.

2.2 Microfluidic device fabrication

Microfluidic channels were fabricated using the soft lithographic technique developed by Y. Xia and G. M. Whitesides [199]. The first step was the generation

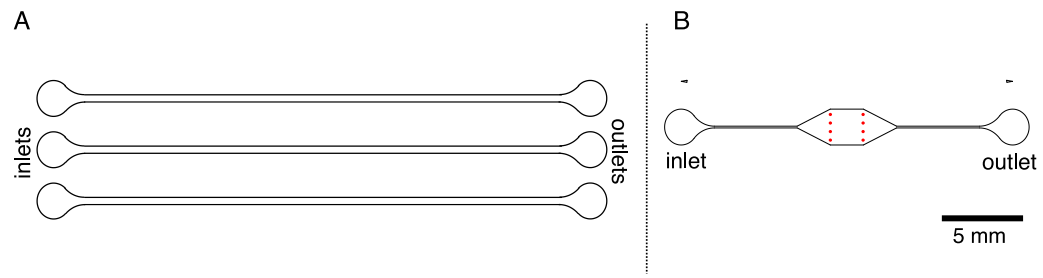

Figure 2.2: Channel geometries: (a) straight channels and (b) the high aspect ratio chamber. Design by D. Wyatt and E. Bodenschatz. Figure adapted from [194].

of the photomask, figure 2.1a.[2] The photomask started out as a quartz glass plate, where one side was plated with a reflective chrome layer. This chrome layer was coated with photoresist. A CAD file containing the channel geometry (figure 2.2) was input into an optical pattern generator (GCA PG3600F), which printed the geometry onto the mask by exposing the photoresist to UV light, one pixel at a time. The mask was removed from the optical pattern generator and placed in a mask processor (Steag Hamatech). The mask processor washed the mask with photoresist developer, dissolving the sections of photoresist that were exposed to light and retaining the sections that were unexposed. Next, chromic acid was applied to remove the chrome that was no longer coated with photoresist. The mask became transparent where the chrome had been removed, i.e. where the channel geometry was printed. The photoresist was stripped off, and the mask was ready for use [198].

The next step was the production of a master wafer, which serves as a reusable mold for the microfluidic devices we built, figure 2.1b. SU-8 photoresist (MicroChem) was spin-coated at 22^o C onto a silicon wafer: A large drop of

[2]The photomasks used in this work were produced by D. Wyatt and G. Amselem in the Cornell Nanoscale Science and Technology Facility (CNF). The master wafers were fabricated by D. Wyatt at the CNF, or with the assistance of G. Amselem and C. Westendorf in the clean room facilities of the Max Planck Institute for Dynamics and Self-Organization

photoresist was placed in the middle of the wafer. To produce a thin, uniform layer of resist, the wafer was then spun up to a few thousand rpm. One can adjust the height of the layer by using photoresists of varying viscosities and by varying the rotation speed and duration. For instance, in order to generate a 50 μm layer, one can spin SU8-50 at 2000 rpm for 35 s [128, 176]. Next, the wafer was baked to remove the solvent from the photoresist, first at 65^o C for 6 minutes, followed by 95^o C for 20 minutes [128]. After a period for cooling and drying had elapsed, the wafer was placed in a mask aligner (EV620). This mask aligner positioned the photomask on top of the wafer, then shined UV light through the mask, exposing the device geometry onto the photoresist. Following a final bake, the wafer was washed with SU-8 developer. The exposed photoresist remained, i.e. the channel geometry formed a positive relief on the wafer. The master wafer was ready for use.

The construction of the microfluidic device came next. We will first describe how the single layer channels were made, as schematically shown in figure 2.1c. Then we will describe the double layer devices, whose principle of construction shares many similarities.

The master wafer was placed in the bottom of a plastic weigh boat, and a 10:1 mixture of poly(dimethylsiloxane) (PDMS) to curing agent was poured on top. This weigh boat was then placed in a vacuum chamber to remove air bubbles. The PDMS was cured in an oven at 80^oC for 1 hour.

A rectangular stamp of PDMS, encompassing the channel was then cut out. Adhesive tape (Scotch Magic, 3M) was placed on the channel side, to protect the device from dust and oil. Holes were then punched, using a sharpened 19 gauge needle, through the PDMS into the channel inlet and outlet. The tape was removed from the PDMS stamp. The stamp and a #1.5 cover glass were

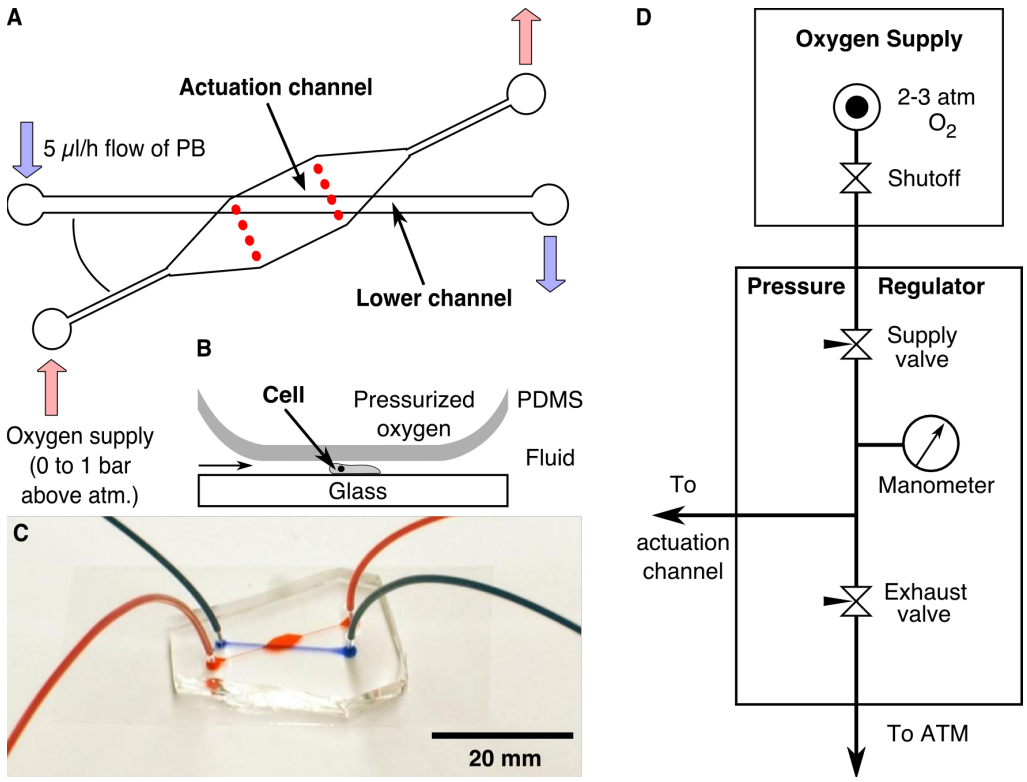

Figure 2.3: Microfluidic through-flow actuator. (a) schematic top view of the device, (b) side view showing the principle of operation, (c) photograph of the device with the top layer filled in red, and the bottom layer in blue, (d) pressure source. Reprinted from [194].

then plasma cleaned (Harrick Plasma) for 30 s, to etch away hydrocarbons and oxidize the surfaces. Immediately after plasma cleaning, the channel side of the stamp was brought into contact with the cover glass, where an irreversible Si-O-Si bond is formed. The channel was ready for use.

We now move on to the double layer devices [194]. These devices were composed of a straight channel (24 μm tall) in the bottom layer, and a wide aspect ratio chamber (28 μm tall) in the upper (actuation) layer. Pressure was applied to the actuation chamber in the upper layer. This pressure caused the elastic membrane separating the upper and lower layers to deform down onto cells situated in the lower layer.

To generate the lower layer, a thin layer of PDMS was deposited onto a straight channel wafer the following way: Two spacers, each constructed of three #1 coverglasses glued together, were placed on the left and right side of the channel geometry. A large, degassed bubble-free drop of PDMS was daubed between the spacers. The long edge of a microscope slide was then slid along the spacers, spreading an even layer of PDMS on the channel geometry. The spacers were then removed, and the wafer was baked in the oven for 45 minutes. This wafer was then set aside until the top layer was ready to be plasma cleaned.

The construction of the top layer was the same as for a single layer device, up until the step at which holes were punched. If the double layer device was a closed-end actuator, only the inlet hole was punched. If the double layer device was a through-flow device, then the inlet and the outlet were both punched. This top layer PDMS stamp was plasma cleaned along with the PDMS coated wafer from earlier.

The channel side of the top layer was then bonded onto the thin PDMS layer in such a way that the chamber on the top layer intersected the bottom layer channel obliquely. (See figure 2.3a). The wafer was then inserted into the 80^o C oven for five minutes. This improved the quality of the bond, and also, as the air in the upper chamber heated up, the chamber ballooned, which prevented the ceiling from collapsing early and bonding irreversibly to the lower layer.

A scalpel was used to score the thin layer of PDMS around the perimeter of the attached stamp. The stamp was then removed from the wafer. The channel side was scotch-taped, and holes were punched through the PDMS into the lower channel's inlet and outlet. The stamp and a #1.5 coverglass were plasma cleaned and bonded together. The double layer device was ready for use.

CHAPTER 3

THE SEARCH FOR GROWTH FACTORS IN *DICTYOSTELIUM DISCOIDEUM*

The population growth, after cells are introduced into a new culture medium, is characterized by four phases: (i) the lag phase, (ii) the exponential phase, (iii) the stationary phase, and (iv) the decline phase. See figure 3.1. Initially, there is a period of time during which the number of cells does not increase significantly. This is termed the lag phase. During this time, the cells are adapting to the new environment by synthesizing ATP, enzymes, cofactors, and ribosomes needed for growth. Also, they may be injured and require time to recover [23, 141]. After the lag phase, the population enters the exponential growth phase, where the cells are growing and dividing at a steady rate. As the cells grow, they consume nutrients and generate waste products. Eventually, the depletion of nutrients and the accumulation of waste lead to a decrease in the growth rate and an increase in the death rate. When these two rates approach one another, the population enters the stationary phase. Finally, the death rate will exceed the growth rate, and the population declines.[1]

In the textbook discussions [23, 141], and in many models (see the review by Swinnen [170]), the lag phase can be viewed as a single cell phenomenon – each cell is adapting to its new environment, and this process takes some time. In this chapter we will present evidence that refutes this classic viewpoint – growth data which shows that the lag time for a cell depends on how many neighbors it has. We will argue that this implies communication between cells. We will then show experimentally that the communication must be short ranged. Finally, we

[1]This chapter contains material from Ref [61]: C. Franck, W. Ip, A. Bae, N. Franck, E. Bogart, and T. Thi Le., *Phys. Rev. E*, **77**:041905, © 2008, The American Physical Society.

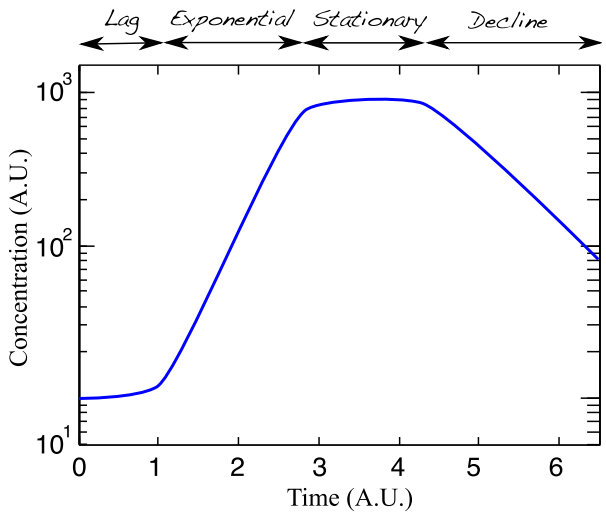

Figure 3.1: The four phases of growth: Lag, Exponential, Stationary, and Decline.

will present a model, based on short range interactions, which can be used to fit the data on cell growth.

3.1 Growth curve experiments

W. Ip, an REU student in C. Franck's lab, collected an impressive 500 hours of population growth data for the AX3 strain of *D. discoideum*. See figure 3.2(a). The starting time, $t = 0$, corresponds to the time at which the cells are inoculated into fresh culture medium. Each growth curve corresponds to a different starting concentration.

By adding the appropriate offsets to the starting times, we find that all the data collapse onto one curve. See figure 3.2(b). In this curve, a transition from lag to exponential phase growth can be seen when the population reaches $\sim 10^4$ cells/mL. Therefore, the exit from lag phase is strongly dependent on the cell density. This implies that, contrary to the conventional wisdom, the lag phase is a multicellular phenomenon.

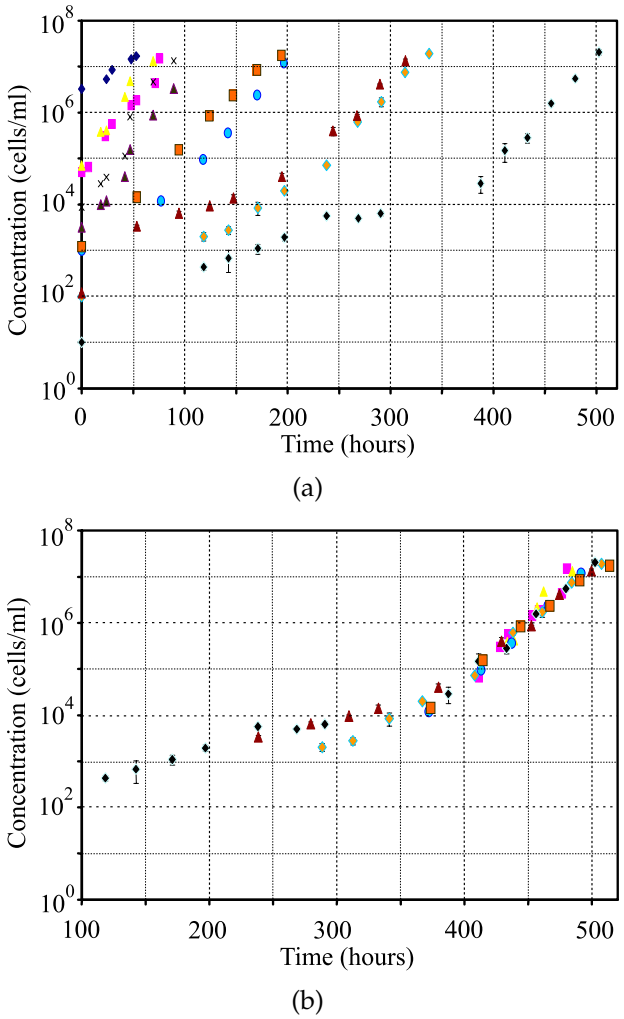

Figure 3.2: (a) W. Ip's growth curves for the AX3 strain of *D. discoideum*. Each marker represents a different starting concentration. (b) The data collapses when the appropriate offsets to time are added.

How can we explain this cell density dependence? There must be some counting mechanism employed by the cells. For this counting mechanism to work, there must be signals which are passed between cells. We postulate that the signaling must occur in one of two ways (i) via some chemical, i.e. a growth factor that accumulates in the growth medium, or (ii) through short range cell-cell signaling. In the next section, we will review my attempt to isolate growth factors.

3.2 Exponential medium reconstitution experiments

For each experiment, AX3 cells were inoculated into an Erlenmeyer flask containing 30 mL of HL-5 culture medium. The flask was placed on an orbital shaker, running at 150 rpm, where the cells were then grown to exponential phase ($\sim 10^6$ cells/mL).

The exponential phase cell culture was passed though a 0.45 μm syringe filter. This filtered, cell-free exponential medium was mixed with equal parts HL-5. Two flasks (which we denote as C and D) were then filled with 20 mL of this reconstituted medium: 50% fresh, unfiltered HL-5, 50% filtered exponential phase medium. Two flasks (which we denote as A and B) were filled with 20 mL of control medium: 50% fresh, unfiltered HL-5, and 50% fresh, filtered HL-5.

These four flasks were then inoculated with a small fixed volume of the original growing cell culture, so that all the bottles contain the same starting cell density. This starting density was always below the transition density of 10^4 cells/mL. The density was measured a few days later to see if there was a difference between growth in reconstituted medium and control medium. This experiment was conducted four times, and the results are summarized in table 3.1.

The idea behind these experiments is as follows: The low starting cell density should bring the cells in the control flasks back down into lag phase growth. If growth factors exist in the exponential medium, then the reconstituted medium should retain these factors. By adding 50% fresh, unfiltered HL-5 to the media, we also ensure that the food supply is not depleted. We expect that the cells in the reconstituted flasks should remain in exponential growth.

In order to make useful comparisons between the experiments and the controls, in the last column of table 1, we display the expected final density (EFD).

Table 3.1: Results of exponential growth medium reconstitution experiments. EFD is the expected final density for exponential growth.

Expt.	Reconstitution?	Starting Density (cells/mL)	Final Density (cells/mL)	Duration (days)	EFD (cells/mL)
1A	Yes	7.0×10^3	7.0×10^5	5	7.2×10^6
1B	Yes	7.0×10^3	1.0×10^6	5	7.2×10^6
1C	No	7.0×10^3	7.8×10^5	5	7.2×10^6
1D	No	7.0×10^3	6.6×10^5	5	7.2×10^6
2A	Yes	2.0×10^3	3.3×10^6	8	1.3×10^8
2B	Yes	2.0×10^3	1.3×10^6	8	1.3×10^8
2C	No	2.0×10^3	1.8×10^4	8	1.3×10^8
2D	No	2.0×10^3	4.0×10^4	8	1.3×10^8
3A	Yes	4.0×10^3	1.2×10^6	5	4.1×10^6
3B	Yes	4.0×10^3	1.3×10^6	5	4.1×10^6
3C	No	4.0×10^3	1.4×10^6	5	4.1×10^6
3D	No	4.0×10^3	1.1×10^6	5	4.1×10^6
4A	Yes	2.1×10^3	3.5×10^5	3	1.3×10^5
4B	Yes	2.1×10^3	1.0×10^5	3	1.3×10^5
4C	No	2.1×10^3	2.6×10^5	3	1.3×10^5
4D	No	2.1×10^3	1.8×10^5	3	1.3×10^5

The expected final density assumes that the cells have been continuously growing with a 12h doubling time:

$$\text{EFD} = (\text{Starting Density}) \times 2^{(\text{Duration})/12h}. \tag{3.1}$$

If the final density is much lower than the EFD, then the cells have spent considerable time in the lag phase, otherwise, they have not. So in order to find evidence for a growth factor, we need to find cases where the controls have densities well below the EFD, and the reconstitution experiments have densities comparable to the EFD.

Experiment 4 does not fit these criteria, because the final densities of the controls are comparable (they actually exceed) the EFD. This indicates that the controls are growing exponentially already, so we should not expect to see any

improvement in the reconstituted medium. In fact, the densities between the controls and the experiments are quite comparable.

Experiments 1, 2, and 3 are potentially good candidates for seeing an effect, because, the average final control densities are (respectively for each experiment) a factor of 10, 4500, and 3.3 lower than the corresponding EFD. Therefore, in these controls, the cells have been growing in lag phase. The ratios between the average final reconstitution and average final control density in these three experiments are 1.2, 79, and 1.0. As these ratios are considerably smaller than the EFD to control ratios, we can conclude that the reconstituted material did not strongly promote exponential phase growth—the experiments failed to demonstrate the existence of growth factors in the medium.

C. Franck further confirmed my null result by growing cells in a microfluidic device. He reasoned that if there are growth factors produced by cells, then one could wash these away by flowing in fresh growth medium. Depending on the flow speed, one would expect that the growth rate should depend of the flow rate. Yet, he observed no marked difference in growth.

3.3 Theory of contact mediated growth

Based on the idea that cells are communicating via close range signaling, C. Franck developed an elegant theory to describe the transition from lag to exponential growth. He assumed that a cell needs to make a certain number of collisions, N_c per measurement time T_M in order to grow normally with rate γ. If we call P_G the probability that this criterion is met, then the cell density n increases according to the following expression:

$$\dot{n} = \gamma P_G n. \tag{3.2}$$

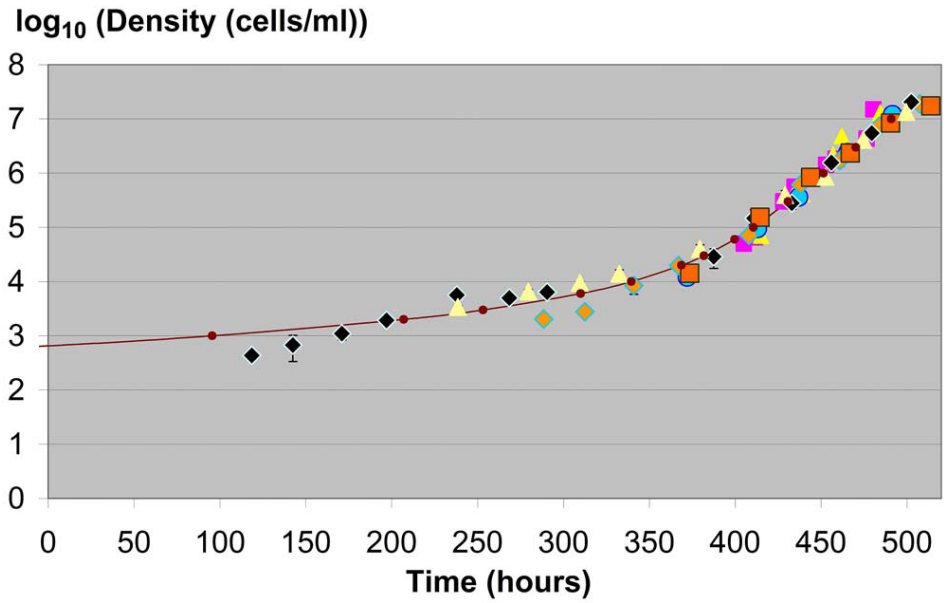

Figure 3.3: Contact mediated theory: Setting $a = 10\,\mu$m, $T = 0.4$ s, $N_c = 1$ and $T_M = 6$ min, we get the solid line fit to the data.

We are left with the task of determining P_G. This is done with scaling arguments. Assuming that the cell motion is a Brownian type of motion, then the time τ between collisions should scale with the square of average distance between cells ($\tau \sim n^{-2/3}$). The collision time should also depend inversely on the cross-sectional area ($\tau \sim a^{-2}$, where a is the cell diameter). Finally, the time between collisions should decrease as the stirring rate increases, i.e., it should scale with the period of the orbital shaker ($\tau \sim T$). Putting these dependencies together, we get

$$\tau \approx a^{-2} n^{-2/3} T. \tag{3.3}$$

Now, if we define the average number of collisions per measurement time as $\lambda \equiv T_M/\tau$, then we get the Poisson probability for having k collisions in the measurement time:

$$p(k, \lambda) = \exp(-\lambda)\lambda^k/k! \tag{3.4}$$

Finally, we get the probability for getting at least N_c collisions per measurement time:

$$P_G = p(N_c, \lambda) + p(N_c + 1, \lambda) + p(N_c + 2, \lambda) + \dots \tag{3.5}$$

$$= 1 - \exp(-\lambda) \sum_{k=0}^{N_c - 1} \lambda^k / k! \tag{3.6}$$

The size of a typical cell is on the order of $a = 10\mu$m. Since the culture was shaken at 150 rpm, the period is $T = 0.4$ s. By choosing $N_c = 1$ and $T_M = 6$ min, we were able to fit the data of W. Ip quite nicely. See figure 3.3. Therefore, the theory predicts that every six minutes there should be at least one collision in order for cell growth to occur.

This model is testable. In future experiments, we could change the period T of the orbital shaker and observe how the growth curves change. Will the theory still fit the data?

CHAPTER 4

A PRIMER ON CHEMOTAXIS

A fundamentally important biological process is the directed motion of cells in response to a chemical gradient, or chemotaxis. Chemotaxis plays a key role in morphogenesis [41], wound healing [36], immune response [127], and cancer metastasis [95]. In the soil, a *D. discoideum* amoeba chases after its food source by following the trail of folic acid left behind by bacteria. After the food supply is exhausted, *D. discoideum* cells rely on chemotaxis up gradients of cyclic adenosine 3′, 5′-monophosphate (cAMP) to aggregate with each other.

Chemotaxis has been intensely studied in both prokaryotes and in eukaryotes. Although this dissertation focuses on the eukaryote *D. discoideum*, it is worthwhile to breifly mention the differences between chemotaxis in these two different groups of cells. The mechanism for gradient sensing in prokaryotes is generally thought to be completely temporal,[1] i.e. these cells sense the gradient by swimming around and detecting changes in concentration as they move, whereas in many eukaryotes,[2] like mammalian leukocytes, fibroblasts, and *D. discoideum*, there exists a spatial component to gradient sensing – they are able to detect the gradient without moving.

[1] H. Berg and E.M. Purcell [17] argue that the difficulty with spatial gradient sensing is that prokaryotes swim, and an apparent gradient will be generated across a moving cell, even if the cell is in a uniform concentration of chemoattractant, because the front of the cell will be hit with more molecules than the back. Furthermore, Y. Tu points out that temporal sensing is more efficient for a swimmer: a cell using spatial sensing measures the concentration differences across its length, whereas a cell employing a temporal sensing mechanism measures concentration differences across a much larger length – the length it swims over its integration time (its memory) [180]. It been shown theoretically, however, that there are situations where spatial sensing is superior to temporal sensing in bacteria [50], and there has been some experimental evidence that supports this [174].

[2] Eukaryotic swimmers (flagellates and cilliates) move quickly and are subject to the considerations of the previous footnote. These swimmers are thought to rely solely on temporal gradient sensing mechanisms [3, 24, 55]. On the other hand, cells that crawl along a substrate can use spatial gradient sensing mechanisms because they move too slowly for the motion–induced apparent gradient to be noticeable.

The model organism for studying prokaryotic chemotaxis is *E. Coli* [19]. Each bacterium has about six flagella. When the flagella rotate clockwise, they group into a bundle that propels the cell steadily forward (running mode), but when the flagella rotate counterclockwise, the bundle breaks up, and the flagella lose their organization, causing the cell to move erratically (tumbling mode). The bacterium executes a random walk by switching back and forth between running and tumbling. When it senses the concentration of chemoattractant (e.g. glucose) increasing with time, the frequency of tumbling decreases, and it moves in a straighter path. Conversely, when the concentration decreases, the frequency of tumbling increases, and the path becomes more jagged. This temporal response to changing concentrations biases the bacterium's random walk up gradients of chemoattractants. [18, 158]

In eukaryotes, the components of chemotaxis are: (i) receptor binding, (ii) direction sensing, and (iii) migration. First, the molecules of the chemoattactant bind to the receptors on the cell membrane. Next, the cell aligns an internal biochemical compass in the direction where the concentration of bound receptors is highest. Finally, the cell protrudes a pseudopod in the gradient direction, and moves forward.

D. discoideum provides a model organism for studying these components of chemotaxis. Developed cells are sensitive to gradients of cAMP with concentration differences as low as 2% between front and back [120, 164] and move quickly ($\sim$10 μm/min as opposed to $\sim$0.5 to 1 μm/min in fibroblasts [157]). Powerful genetic and biochemical techniques have been developed for uncovering the signal transduction pathways [102]. Furthermore, *D. discoideum* chemotaxis is similar to that in other eukaryotes [100, 46, 133, 44].[3]

[3]Although *Dictyostelium* cells and mammalian neutrophils are separated evolutionarily by a billion years [54], they share many conserved signaling pathways [46], and the models for *Dictyostelium* are usually written to apply for both systems.

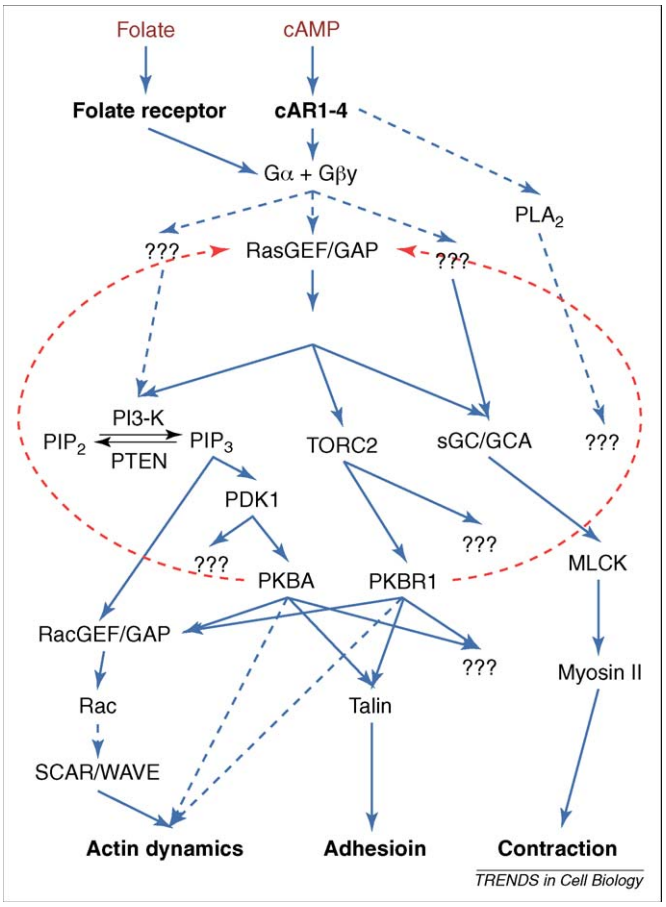

Figure 4.1: Signal transduction pathways involved in chemotaxis. Reprinted from [103]: *Trends in Cell Biology*, 19:523-30, Copyright (2009) with permission from Cell Press.

4.1 Biochemical pathways for direction sensing

Along the surface of a developed chemotactic *D. discoideum* cell are $\sim 7 \times 10^4$ seven-transmembrane G-protein coupled cAR1 receptors [93].[4] When a cAMP molecule binds to cAR1 outside of a cell, it induces a conformal change in the receptor. On the intracellular side, this receptor interacts with a heterotrimeric G-protein ($G\alpha\beta\gamma$), enabling the exchange of GDP for GTP on the α subunit

[4]There are four distinct 7TM cAMP receptors, cAR1–cAR4, but gene knockout experiments show that cAR1 is the only one essential for chemotaxis in the aggregation stage [133, 92, 156, 114]

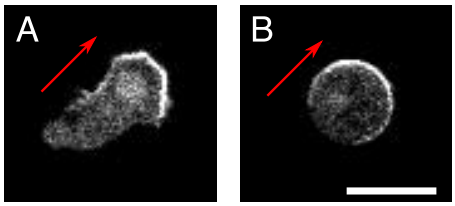

Figure 4.2: PH_{CRAC}-GFP localization in (a) an untreated cell, and (b) in a cell treated with LatA. The red arrow indicates the direction of the cAMP gradient. Images graciously provided by Gabriel Amselem.

of the G-protein [201]. This leads to the dissociation of the G-protein into GTP-Gα and G$\beta\gamma$. Downstream of the G-protein dissociation is the activation of PI3K (phoshodylinisotol 3-kinase), and PTEN (phosphatase and tensin homolog) [76, 65]. The PI3K phosphorylates PI(4,5)P_2 (phosphatidylinisotol-4,5-bisphosphate), making PI(3,4,5)P_3 near the cell membrane. The PIP_3 act as binding sites for proteins that contain a pleckstrin homology (PH) domain [97], like CRAC, PhdA, and Akt/PKB (PKBA). The PTEN is an antagonist to PI3K – it dephosphorylates PIP_3 to PIP_2. See figure 4.1.

Through the use of fluorescent protein constructs, we can observe the localization of various proteins in the signaling pathway. When the cells are placed in a gradient of cAMP, the cAR1 receptors remain uniformly distributed around the cell, the G$\beta\gamma$ proteins are slightly localized in the front (where there is more cAMP) [91], but PTEN clearly localizes to the back of the cell [65, 84]. Higher activity of PTEN in the back and PI3K in the front of the cell induces a gradient in PIP_3. This response can be seen in PH-GFP constructs: When a gradient of cAMP is applied to a PH_{CRAC}-GFP cell, within the first 10 s, the entire cell perimeter begins to fluoresce, which indicates that PH domain proteins are recruited to the front and the back of the cell [88, 202]. Over the next minute, the fluorescence at the back of the cell dies down, while the front of the cell remains bright (see figure 4.2a).

One PH domain protein in particular, PKBA (Akt/PKB), was shown to be an important bridge between direction sensing and motility – pkbA null cells were shown to be chemotactically deficient, as were cells that overexpressed membrane targeted PKBA [121]. These observations made it appear as though PIP_3 localization was the internal compass that guided the cell, with the biochemical machinery for motility working downstream of this pathway.

This viewpoint, was questioned by N. Andrew and R. H. Insall (2007) who observed that cells treated with the PI3K inhibitor LY294002 were still chemotactic [5]. The *coup de grâce* was dealt by O. Hoeller and R. R. Kay (2007), who knocked out all five PI3Ks and PTEN, thereby eliminating the ability of the cell to produce PIP_3 gradients. These cells were still able to chemotax accurately, albeit more slowly, up a gradient of cAMP [80].

Since the cells are able to sense direction in the absence of PIP_3 gradients, there must be alternate pathways in play. A hint is given by the Ras proteins [98]. Ras is rapidly activated (in ~ 2 s) and was demonstrated to be an upstream regulator of PI3K; removing Ras function removes directional movement [153]. The protein TorC2 (target of rapamycin complex 2), like PI3K, is also regulated by Ras. In an impressive effort, Y. Kamimura et al. worked out many details of this TorC2 pathway [96]. They showed that TorC2 acts on PKBR1 which mediates the phosphorylation of Talin, which in turn, plays a role in adhesion by interacting with integrin-like proteins. Also activated are two Ras GEFs and RhoGap. These have been hypothesized to play a role in the activation of the suppressor of cAMP receptor (SCAR), which in turn plays a role in the activation of the actin related protein-2/3 (Arp2/3) complex [103]. In §4.3, we will discuss the role Arp2/3 plays in cell motility.

Genetic screening for mutants that are sensitive to reductions in PI3K activity also suggests that phospholipase A_2 (PLA_2) plays an important role in chemotaxis. Deleting PLA_2 and PI3K impaired a cell's ability to chemotax [33], however, the PLA_2 pathway is still unclear. See [103] and references therein for more information about the parallel pathways to PIP_3.

4.2 Biological models for direction sensing

Now that we have seen some of the biochemical actors known to play a role in chemotaxis, we will review the different types of models for direction sensing:[5] 1. Pilot pseudopod, 2. First hit inhibition, 3. Mechanical restriction, 4. Positive feedback, 5. Intermediate depletion, 6. Local excitation, global inhibition, and 7. Phenomenological. In table 4.1 we summarize the properties of these models.

Pilot pseudopod: In these models [71, 46, 186, 190], cells use a temporal mode of gradient sensing, similar to bacteria. Chemotactic cells extend pseudopodia in a random directions. Pseudopods that sense an increase in chemoattractant concentration are reinforced, whereas pseudopods that feel a decrease in concentration are retracted. This biased random walking of pseudopods leads to a net motion up the gradient. Although in the past, this model was dismissed – when a chemotactic cell is placed into a gradient, it was assumed that the cell will first sense the gradient, and then generate a pseudopod pointing in the correct direction – recent work suggests that this biased random pseudopod walk is used by cells climbing up shallow gradients [5, 186].

[5] The classification scheme for the first six models is from Devreotes and Janetopoulos (2003) [44].

Table 4.1: Biological models for direction sensing. Here we list whether the model is based on a biochemical pathway, if it produces a strong, switch-like front to back asymmetry, and if the response reverses direction when the external gradient is reversed. (*) Note that in the geometric model of [152], the response contribution from the external gradient is reversable, but the internal polarization component remains fixed. Table adapted from [4].

Model	References	Biochemical	Switchlike?	Reversible?
1. Pilot Pseudopod	[46, 71, 186, 190]	N/A	N	Y
2. First Hit	[149]	cAMP/cGMP	Y	Y
3. Mechanical Restriction	N/A	N/A	Y	Y
4. Positive Feedback	[122]	$Ca^{2+}/H^{+}/InsP_3R$	Y	Y
	[129]	PI cycle	Y	N
	[20]	N/A	Y	Y
	[125]	Rho-GTPase	Y	Y
	[66]	PI3K/PTEN	Y	N
5. Intermediate Depletion	[140]	N/A	For high backgrounds.	Y
6. LEGI type	[111, 116]	Pi3K/PTEN	N	Y
	[146]	G-protein	Y	Y
7. Phenomenological	[152]	N/A	N	Y*

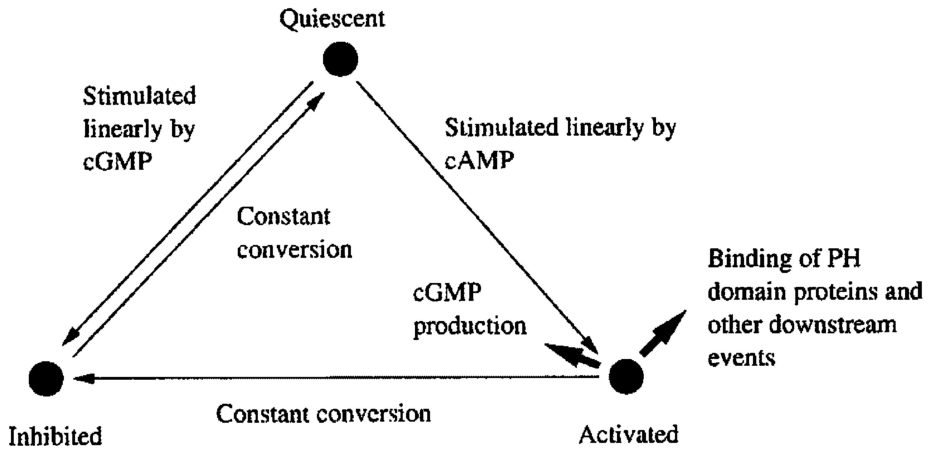

Figure 4.3: Schematic of the first hit model. The membrane can be in three states, and the transitions between states are mediated by cAMP (activator) and cGMP (inhibitor). Reprinted from [149]: *Biophysical Journal* 83:1361-7, Copyright (2002), with permission from The Biophysical Society.

First hit: When the cells are detecting direction, and deciding which way to move, they should select a definite front and back. This definite, switch-like nature of gradient sensing can be seen at an early stage in the signal transduction pathway. Experiments with PH-GFP show that when cells are in a gradient of cAMP, the PH domain proteins are highly localized to the front of the cell (figure 4.2). W.-J. Rappel et al. proposed the first hit model to explain this strongly asymmetric response (figure 4.3) [149]. When the gradient is generated, the leading edge of the cell gets hit with cAMP first. This activates the front of the cell, and releases an inhibitor that quickly diffuses across the cell. The back of the cell is inactivated by the inhibitor. This inhibitor was proposed to be the nucleotide cGMP, (i) because of its high diffusion coefficient, (ii) because it rapidly accumulates when a cell is exposed to cAMP, (iii) and because mutants impaired in the ability to synthesis cGMP are also aggregation impaired [151].

Unfortunately, several experiments do not support this model [146]. As we discussed previously, when a gradient of cAMP is applied to a PH_{CRAC}-GFP cell, within the first 10 s, the entire cell perimeter begins to fluoresce, which indicates that PH domain proteins are recruited to the front and the back of the cell [88, 202].[6] Over the next minute, the fluorescence at the back of the cell dies down, while the front of the cell remains bright. This is in contradiction to the theory, which would predict that the sharp anterior–posterior asymmetry exists throughout the gradient sensing process – the first hit model does not predict the observed translocalization response.

Mechanical restriction: In these models [44], a pseudopod extension at the front of the cell is coupled, via the cytoskeleton, to uropod retraction in the back of the cell. For instance, when a chemoattractant is applied to a *Physarum polycephalum* amoeba with multiple pseudopods, the pseudopods closest to the source of chemoattractant are selectively stabilized. However, when these cells are treated with the microtubule inhibitor nocodazole, the stabilization disappears – the cells still produce pseudopods, but they do not produce any net chemotactic response [182]. In neutrophils, nocodazole drastically reduces the chemotactic accuracy [200]. These experiments hint that mechanical restriction might play an important role in chemotaxis, but until this mechanism is better elucidated with experiments, there probably will not be a quantitative theory of mechanical restriction.[7]

[6] Note that in our discussions we will compare many of the models with PH-GFP experiments which probe the PIP_3 signaling pathway, and not TorC2 or PLA_2. This is because much less is known about these alternate pathways.

[7] Devreotes and Janetopoulos list this as one of the direction sensing models, but they only state it qualitatively. I couldn't find any theoretical models of mechanical restriction.

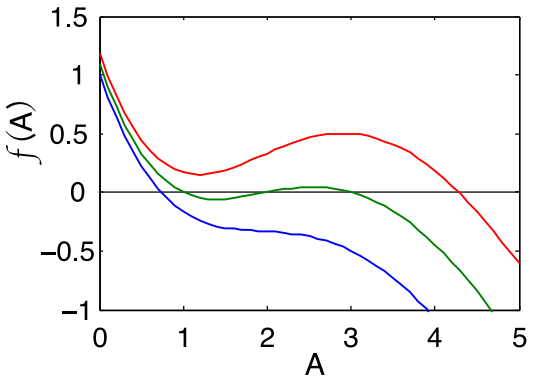

Figure 4.4: Model of a bistable switch: A phase diagram, showing $\frac{dA}{dt}$ versus A. Different curves correspond to different values of s. Adapted from [83]. Copyright (2002) American Association for the Advancement of Science.

Positive feedback: This large class of models contains (i) Turing models [122, 129, 168], based on the theory of pattern formation by A. Turing [181], A. Gierer, and H Meinhardt [73], (ii) trigger wave propagation models [20, 125], and (iii) phase separation models [66, 67, 68]. The key feature in all these models is a strong, nonlinear amplification that arises from the autocatalytic feedback of a chemical species, called the activator. This feedback is embodied in the following equation [83]:

$$\frac{dA}{dt} = -\alpha A + s\left(\frac{A^2+\beta}{A^2+\gamma}\right) \equiv f(A). \tag{4.1}$$

The concentration of the autocatalytic species is A. The first term, $-\alpha A$, describes a constant decay. In the second term, s corresponds to a signal that mediates the activator response. The numerator contains the autocatalysis term, A^2, and a basic production term, β, which initiates autocatalysis when $A = 0$. The denominator allows for saturation to occur when $A^2 \gg \gamma$.

A sample phase portrait is shown in figure 4.4 where the parameters are set at $\alpha = 2$, $\beta = 1$, $\gamma = 11$. The three curves correspond to varying levels of signal – blue corresponds to $s = 11$, green to $s = 12$, and red to $s = 13$. Steady states occur when $f(A) = 0$. These states are stable when the slope, $df/dA < 0$, and

unstable otherwise. When the signal is set to 12, the system is bistable at $A = 1$ and $A = 3$. When the signal is lowered to 11, the higher branch is lost, leaving one stable state at $A = 0.732$. When the signal is raised to 13, the lower stable state is lost, leaving a stable state at $A = 4.29$. We see a huge amplification when a signal pushes the system past the bistable state. When $s = 11 \rightarrow 13$, the activator jumps: $A = 0.732 \rightarrow 4.29$: an 18% increase in s translates into a 490% increase in A.

This switch-like feedback alone is inadequate to explain gradient amplification by chemotactic cells. If a cell is placed in a shallow gradient, the signal should be strongly amplified in the front, but not in the back. As we saw above, the switch-like mechanism allows strong amplification of the signal (e.g. cAR1 occupancy) when the system crosses the very narrow bistable state, and if we require this "switch to be flipped on" in the front but not in the back, then we can only detect gradients with a very narrow range of midpoint concentrations. In the **Turing models**, this problem is solved by adding a quickly diffusing inhibitor, H, that is synthesized with the activator. For example (cf. [73], eqn 16):

$$\frac{\partial A}{\partial t} = s\left(\frac{A^2/H + \beta}{A^2 + \gamma}\right) - \alpha A + D_a \nabla^2 A \tag{4.2}$$

$$\frac{\partial H}{\partial t} = ksA^2 - \eta H + D_h \nabla^2 H, \tag{4.3}$$

where $D_a \ll D_h$. Now, if the parameters have been appropriately chosen, when a cell is put into a shallow gradient with a moderate midpoint concentration, the activator begins to increase quickly at both the front and the back of the cell, with much more being made at the front. As the activator increases, so does the inhibitor, again with more being made in the front than in the back, but the diffusion of the inhibitor is quick, so it diffuses away from the front, allowing more activation to occur. This inhibitor that diffused away from the front of the cell inhibits the back, preventing the posterior activator concentration from catching

up to the anterior. A stable spatial pattern forms with activator strongly localized to the front. Unfortunately, these structures are often too stable, and they tend to lock into place even when the external stimulus (i.e. gradient direction) changes.

The first to apply the Turing model to cells was H. Meinhardt [122]. In his model, there is a nondiffusing ($D_a = 0$) activator, and a global ($D_h = \infty$) inhibitor. As mentioned above, the interplay between these two elements is used to detect the direction of the chemotactic signal, but in order to prevent the freezing of the response, a third localized, nondiffusing inhibitor was added. This local inhibitor works on a much slower time scale than the global inhibitor, and over time removes long lived structures. Meinhardt suggested that the positive feedback activator is Ca^{2+}-induced-Ca^{2+} release at voltage-gated channels, the global antagonist is H^+, and the local antagonist is the inositol 1,4,5-trisphosphate receptor. The identification for the activator was contradicted by experiments on *D. discoideum*, which showed that cells are capable of chemotaxis when Ca^{2+} release was inhibited [111, 185].

A. Narang et al., attempted to develop a more biologically realistic Turing model [129, 168]. See figure 4.5a. They modeled the transfer of phosphoinositides (PIs) from the ER to the membrane as a positive feedback process mediated by the input signal, and inhibited by the rapidly diffusing cytosolic inositol, whose role is to return membrane PIs to the ER. The model agrees with several experimental observations: it explains polarized sensitivity, i.e., if the direction of a gradient is changed, a polarized cell is more likely to turn than it is to repolarize [44] and it also is able to explain spontaneous polarization in uniform chemoattractant concentrations [138, 139, 202], however, it does not explain why in latrunculin treated cells, this polarized sensitivity disappears. Furthermore,

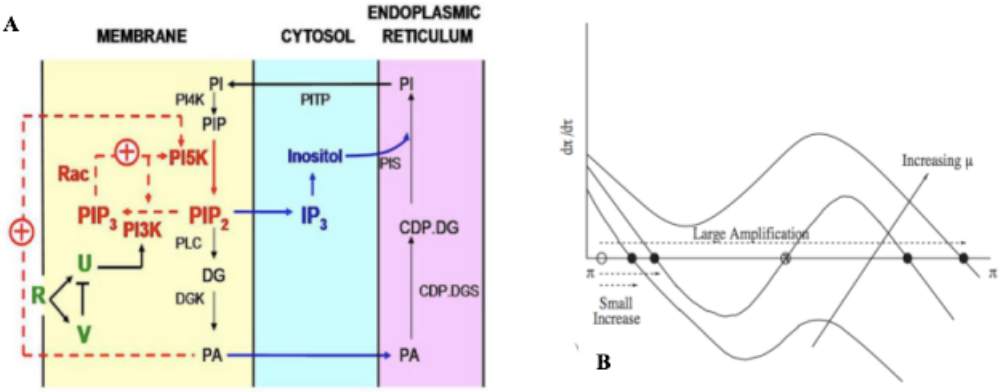

Figure 4.5: The model of Narang, Subramanian, and Lauffenburger. (a) The phosphoinisotide metabolism cycle. (b) The nonlinear dynamics of the model: π is the (dimensionless) density of phosphoinositides in the membrane, and τ is dimensionless time. Reprinted from [168]: *Journal of Theoretical Biology*, 231:49-67, Copyright (2004), with permission from Elsevier.

there are controversies concerning the identities of the local activator and global inhibitor.

The **trigger wave** models are based on the concept that, in a spatially extended bistable system, the interface between regions of the two stable states moves like a wave. As before, the autocatalytic bistable system can be written as

$$\frac{\partial A}{\partial t} = D_a \frac{\partial^2 A}{\partial x^2} + f(A), \tag{4.4}$$

where f has three roots $A_1 < A_2 < A_3$, with A_1 and A_3 corresponding to the stable fixed points. Traveling wave solutions are of the form

$$A(x,t) = g(x - ct), \tag{4.5}$$

where $A(-\infty, t) = A_3$, $A(+\infty, t) = A_1$, and the speed is given by

$$c = \frac{\int_{A_1}^{A_3} f(A)dA}{\int_{-\infty}^{\infty} [dg(\zeta)/d\zeta]^2 d\zeta}. \tag{4.6}$$

Note that the direction of the wave is determined by the sign of the numerator:

$$\text{Sign}(c) = \text{Sign}\left(\int_{A_1}^{A_3} f(A)dA \right). \tag{4.7}$$

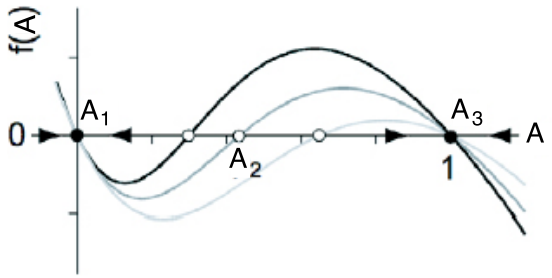

Figure 4.6: Phase diagram for the autocatalytic species A in the trigger wave model of direction sensing. The three cases shown here, in the order of increasing A_2, correspond to a positive (black), zero (gray), and negative (light gray) trigger wave velocity. Adapted from [20], Copyright (2008) with permission from IOP Publishing Ltd.

In the trigger wave model of Beta et al. [20], a biochemical species R, whose concentration reflects the external gradient, is coupled into the dynamics of the bistable species A, such that the level of R adjusts the unstable fixed point A_2, while keeping A_1 and A_3 fixed. See figure 4.6. Parameters in this model are chosen so that at the front of the cell, a high value for R leads to a low value of A_2, and consequently, positive trigger velocities, whereas at the back, a low value of R leads to a high value of p_2 and negative trigger wave velocities. Thus, the interface between the regions of high concentration and low concentration is pushed towards the middle of the cell. A novel aspect of this model is that noise drives the system. It is noise that generates the different regions of high and low concentration, and it is noise that prevents the system from locking up under gradient reversals. The limitation with this model, however, is the particularity in the choice of parameters that is necessary to make the model work.

The trigger wave model of Mori et al. [125] is composed of A, a slowly diffusing autocatalytic activator and B, a rapidly diffusing promoter that is consumed

as A is created:

$$\frac{\partial A}{\partial t} = D_a \frac{\partial^2 A}{\partial x^2} + f(A, B), \tag{4.8}$$

$$\frac{\partial B}{\partial t} = D_b \frac{\partial^2 B}{\partial x^2} - f(A, B). \tag{4.9}$$

In this model, the integral

$$I(B) \equiv \int_{A_1}^{A_3} f(A, B) dA \tag{4.10}$$

increases monotonically with B. Initially, A is low, and B is high. Then a high concentration of chemoattactant at the cell front induces A to jump to the high state A_3. This region propagates as a trigger wave towards the back of the cell. However, as A is generated and B is depleted, eventually $I(B)$ approaches zero, and the wave front stops – the wave is pinned. Provided that the parameters are chosen properly, this occurs somewhere in the middle of the cell. This model predicts that the region of polarization is independent of signal strength.

In the **phase separation** model, the the following reactions of the PIP_3 were modeled stochastically:

$$\text{PI3K(cytosol)} + \text{Rec}(i) \rightleftharpoons \text{PI3K} \cdot \text{Rec}(i), \tag{4.11}$$

$$\text{PTEN(cytosol)} + \text{PIP}_2(i) \rightleftharpoons \text{PTEN} \cdot \text{PIP}_2(i), \tag{4.12}$$

$$\text{PI3K} \cdot \text{Rec}(i) + \text{PIP}_2(i) \rightarrow \text{PI3K} \cdot \text{Rec}(i) + \text{PIP}_3(i), \tag{4.13}$$

$$\text{PTEN} \cdot \text{PIP}_2(i) + \text{PIP}_3(i) \rightarrow \text{PTEN} \cdot \text{PIP}_2(i) + \text{PIP}_2(i), \tag{4.14}$$

$$\text{PIP}_2(i) \rightarrow \text{PIP}_2(j), \text{ and} \tag{4.15}$$

$$\text{PIP}_3(i) \rightarrow \text{PIP}_3(j) \tag{4.16}$$

Here $\text{Rec}(i)$ represents an active receptor, i represents a site on the plasma membrane, and j is a neighboring site. Note that equations 4.15 and 4.16 represent diffusion (random walk). The positive feedback occurs in equations 4.12 and

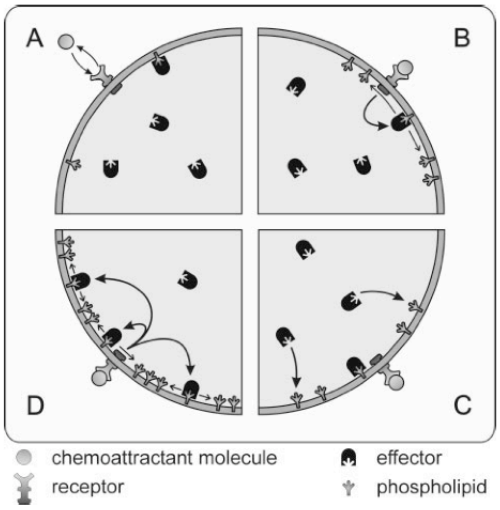

Figure 4.7: Intermediate depletion model. (a) Receptor activation (b) Second messenger production (c) Effector translocation (d) Amplification. Reprinted from [140]: *Biophysical Journal*, 81:1314-23, Copyright (2001) with permission from the Biophysical Society.

4.14: PIP_2 recruits PTEN from the cytosol to the membrane, where the PTEN produces more PIP_2. Simulations show that in uniform concentrations, the membrane spontaneously separates into two phases, PIP_3-rich or PIP_2-rich. In a gradient of chemoattractant, the PIP_3-rich regions occurs at the cell front.

Intermediate depletion: This model contains an activator that is amplified via a positive feedback loop, but it lacks the quickly diffusing inhibitor seen in the previous models [140]. Rather, it is assumed that the activator is a limited resource, and inhibition in the back of the cell is due to the front using up this resource. More specifically, there are slowly diffusing membrane bound phospholipids, and quickly diffusing cytosolic effector (or activator) molecules that bind to these phospholipids. When a chemoattractant molecule binds to a receptor, the membrane is stimulated, which, with the aid of local effector–phospholipid complexes leads to the production of more phospholipids (figure 4.7b). These

phospholipids bind effector molecules (figure 4.7c), which in turn aid in the production of more effector–phospholipid complexes (figure 4.7d), thus closing the feedback loop. At the front of the cell, this process takes off. The effector molecules are quickly sequestered from the cytosol to the leading edge. This depletion of cytosolic effector inhibits the build-up of effectors in the back.

The weakness of this model is the dependence of the depletion mechanism on the average concentration of the chemoattractant. For low background concentrations, no depletion will occur. This contradicts experiments which show that cells are capable of chemotaxis over a wide range of average (midpoint) concentrations [88, 164].[8]

Local excitation, global inhibition: When a cell walks up a gradient of chemoattractant, the midpoint concentration increases, but the cell's ability to sense the gradient should not be seriously affected. The cell should adapt by subtracting the constant background from the signal. The LEGI models [134, 111, 106, 116], were proposed to explain how this adaptation mechanism might work. These models are similar to the positive feedback models in that there is a localized activator, and a rapidly diffusing, global inhibitor, however, there is no autocatalysis. The essence of LEGI is captured in figure 4.8a:

A signal, S, (i.e. receptor binding), induces the synthesis of an activator enzyme, A, and an inhibitor enzyme, I. The activator is localized, and its concentration reflects the signal generating it. The inhibitor on the other hand is a fast diffuser, and its concentration reflects a spatial average of the signal. The activator catalyzes the activation of a response molecule from an inactive (R) to an active state (R^*). The inhibitor catalyzes the reverse reaction. This antagonistic relation between local excitation and global inhibition will be reflected

[8]This is thought to be true for *D. discoideum* and neutrophils, but not fibroblasts [157].

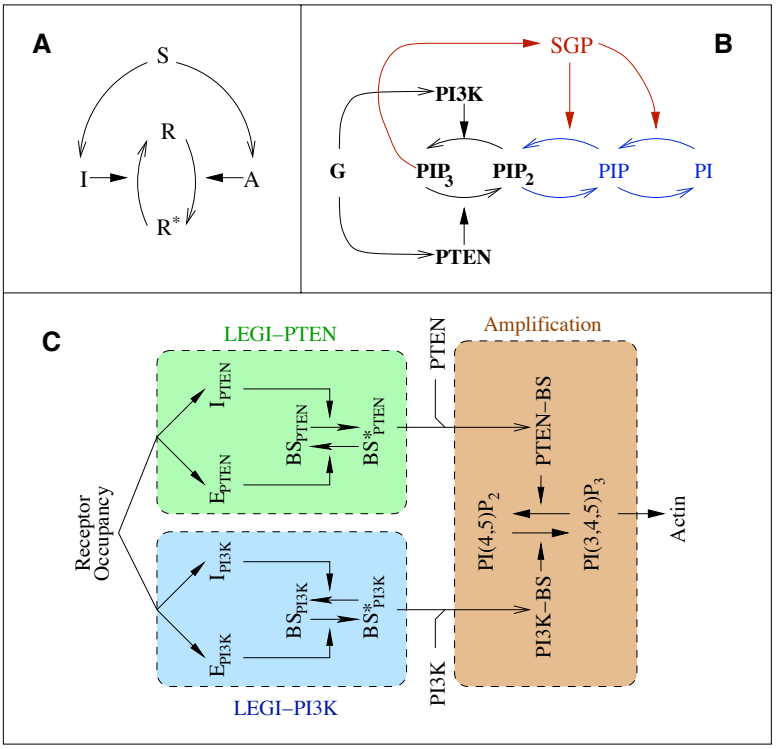

Figure 4.8: The LEGI models: (a) Basic LEGI mechanism, (b) LEGI model of A. Levchenko and P. Iglesias 2002. (c) Two complementary LEGI model of L. Ma et al. 2004. Figures (a) and (b) are adapted from [111]: *Biophysical Journal*, 82:50-63, Copyright (2002) with permission from the Biophysical Society. Figure (c) is adapted from [116]: *Biophysical Journal*, 87:3764-74, Copyright (2004) with permission from the Biophysical Society.

in the response the following way: since the activator that generates the response is graded, the response will reflect the gradient of chemoattractant, but the response should not be dependent on the actual level of the concentration, because the inhibitor "subtracts" away the average background.[9] Notice that because there is no positive feedback in this model, the response does not freeze as it does in the Turing models.

[9] Actually, we will see that inhibitor divides the background away. However, the word *subtract* sounded more appropriate than *divide*.

The equations that describe this process are

$$\frac{\partial A}{\partial t} = -k_{-a}A + k_a S, \tag{4.17}$$

$$\frac{\partial I}{\partial t} = -k_{-i}I + k_i S + D\nabla^2 I, \text{ and} \tag{4.18}$$

$$\frac{\partial R^*}{\partial t} = -k_- I R^* + k_+ A R, \tag{4.19}$$

where the k's are the rate constants for decay or creation of a chemical species, and D is the diffusion coefficient of the inhibitor. Let's look at the steady state case, and for simplicity, let's assume the diffusion coefficient is infinitely large. Also, let $R + R^* = R_{tot} = \text{const}$. Then,

$$A_s = \frac{k_a}{k_{-a}} S \tag{4.20}$$

$$I_s = \frac{k_i}{k_{-i}} \bar{S} \tag{4.21}$$

$$R_s^* = \frac{k_+ A_s / I_s}{k_- + k_+ A_s / I_s} R_{tot}, \tag{4.22}$$

where $\bar{S}$ is the spatial average of the signal. Notice that the the signal only shows up in steady state response as the ratio $S/\bar{S}$, so we see that, as long as the relative gradient is held fixed, the response is independent of the midpoint concentration. This gradient sensing model allows for perfect adaptation.

Levchenko and Iglesias [111] originally identified the signal as being the activation of G-proteins by occupied receptors. This in turn leads to the activation of PI3K and PTEN, which in this model are respectively identified as the activator and the inhibitor (figure 4.8b). The excitation process is the phosphorylation of PIP_2 to PIP_3. The inhibition process is the dephosphoylation of PIP_3. This model suffers from a fatal flaw – since the diffusion coefficient is finite, the inhibitor must localize slightly towards the front,[10] however experiments show that the proposed inhibitor, PTEN, accumulates at the back of the cell [65, 84].

[10] More inhibitor is generated in the front so there must be more there.

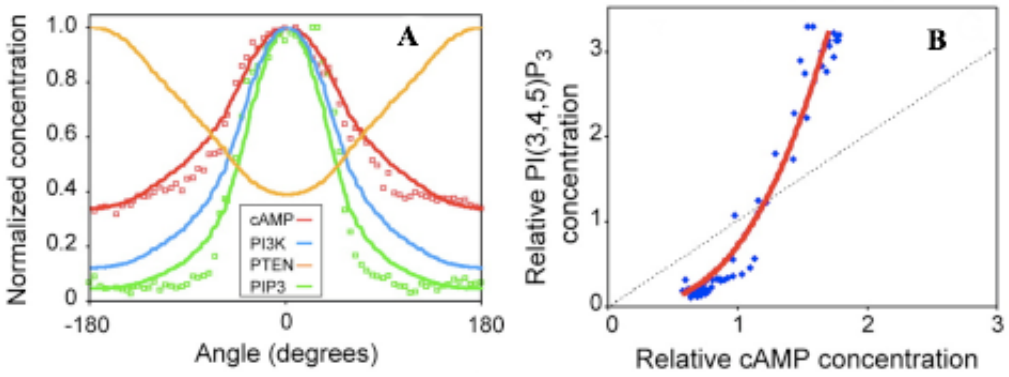

Figure 4.9: (a) Response of the complementary LEGI model vs. position along cell membrane. Data are normalized to the maximum value. (b) PIP_3 concentration along the membrane vs. cAMP concentration. Both axes have been normalized to the average values. Blue dots represent experimental data. Reprinted from [116]: *Biophysical Journal*, 87:3764-74, Copyright (2004) with permission from the Biophysical Society.

LEGI was rescued from this fatal flaw by Ma et al. (2004) [116]. See figure 4.8c. In this model, two complementary LEGI mechanisms are activated by occupied receptors. One of the LEGI modules, LEGI-PI3K works to activate binding sites at the front of the cell, while the other LEGI module, LEGI-PTEN works to deactivate binding sites for PTEN. These two modules explain the complementary localization patterns of PI3K in the front, and PTEN in the rear. The LEGI mechanism itself does not amplify the gradient, so the PI3K and PTEN are not strongly localized. However, their complementary localization and their antagonistic roles in $PIP_2 \rightleftharpoons PIP_3$ conversion leads to an amplified response in the localization of PIP_3 to the front of the cell. (See figure 4.9a.)

The actual biochemical identities of the binding sites and their activator/inhibitors, were left as unknowns with certain reactive and diffusive properties: the inhibitor diffusion rates are estimated to be 50 $\mu m^2/s$, a typical value for free cytosolic proteins, and the reaction rates were determined by fitting the model to experimental data of homogeneously stimulated cells. With these assump-

tions, this model fits data showing the localization of PIP_3 along the membrane of a cell that has been exposed to a gradient (figure 4.9). The model's response is not switchlike – steeper gradients elicit greater responses, and since this model relies on LEGI modules, it predicts that chemotactic cells respond to relative gradients, not absolute gradients. This statement is supported by some experiments [57, 88], but contradicted by recent work [164].

A modified version of LEGI, termed the **balanced inactivation** model was developed by H. Levine et al. (2006) to produce a strong switch-like amplification. As in the LEGI scheme, there is a localized activator and global inhibitor. This time, however, the activator and inhibitor react directly and annihilate each other on the cell membrane.[11] The equations that describe the balanced inactivation model are

$$\frac{\partial A}{\partial t} = k_a S - k_{-a} A - k_i A B_m \qquad \text{at the membrane,} \tag{4.23}$$

$$\frac{\partial B_m}{\partial t} = k_b B - k_{-b} B_m - k_i A B_m \qquad \text{at the membrane,} \tag{4.24}$$

$$\frac{\partial B}{\partial t} = D\nabla^2 B \qquad \text{in the cytosol, with} \tag{4.25}$$

$$D\frac{\partial B}{\partial n} = k_a S - k_b B \qquad \text{as the boundary condition.} \tag{4.26}$$

In these equations, S is the signal (i.e. density of bound receptors). A represents the density of activator. The inhibitor is represented by B_m if it is bound to the membrane, and by B if it is freely diffusing in the cytosol. Activation of the chemoreceptors causes equal amounts, $k_a S$, of membrane bound activator and cytosolic inhibitor to be generated. The activator remains in place, while the cytosolic inhibitor diffuses around inside the cell. At the boundary, the cytosolic inhibitor can bind to the membrane with a rate $k_b B$. Membrane bound activator

[11] Recall that in LEGI, the activator and inhibitor did not directly interact with each other, rather they played antagonistic roles in the activation/deactivation of a third biochemical species, the response.

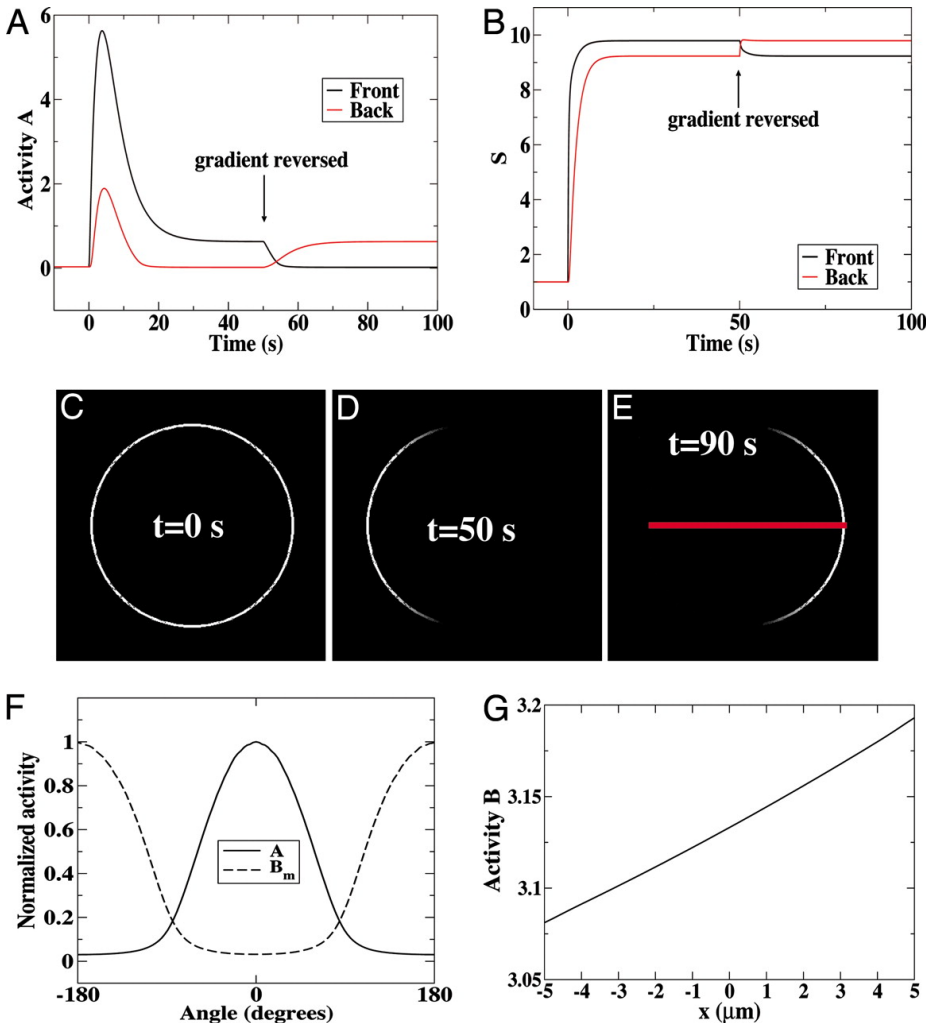

Figure 4.10: Results of the balanced inactivation model. (a) The activator concentration in the front and back of the cell vs. time, in response to a shallow gradient, (b) of chemoattractant generated at $t = 0$ and flipped at $t = 50s$. (c), (d), and (e) show the spatial distributions of activator at various times. (f) shows the localization of activator to the front of the cell, and the (membrane bound) inhibitor to the back of the cell. (g) The cytosolic inhibitor concentration across the cell. Reprinted from [112]. Copyright (2006) The National Acadamy of Sciences of the USA.

and inhibitor annihilate each other with rate $k_i AB_m$. In these equations, A and B_m decay at a rate of $k_{-a}A$ and $k_{-b}B$ respectively.

When a cell is exposed to a gradient of chemoattractant, the signal is greater at the front of the cell than at the back, so more activator is produced in the front. The cytosolic inhibitor is generated at the same rate as the activator, but since it is quickly diffusing, its value roughly equals the spatial average of the activator. At the boundaries, this inhibitor binds to the membrane. At the front of the cell, the activator concentration will exceed that of the bound inhibitor, while at the back, the inhibitor concentration will exceed the activator concentration. The inhibitor and activator will undergo mutual annihilation (with a high rate constant k_i), and the one with a higher concentration survives. Therefore, we expect the activator to be strongly localized to the front, whereas the inhibitor should be strongly localized to the back, as is seen in figure 4.10f. When the gradient is switched (figure 4.10b), notice that the localization of activator flips—it doesn't freeze (figure 4.10a). Furthermore, the model is consistent with the experimental observation that plagued the first hit model: when a cell is placed into a gradient, there is a large initial response along the cell membrane, followed by a decay into a steady, localized response (figure 4.10).

This model depends on a delicate balance between the activator and the inhibitor. If the total amount of inhibitor was greater than activator, then the inhibitor might wipe out the activator everywhere, including the front, and conversely, as well. To ensure a balance between activator and inhibitor, the activator and inhibitor are generated at the same rate ($k_a S$). Therefore, Levine et al. identified the activator as Gα and the inhibitor as G$\beta\gamma$. The creation and annihilation is the disassociation and reassociation of these subunits. The problem with this identification, is that fluorescence resonance energy transfer (FRET)

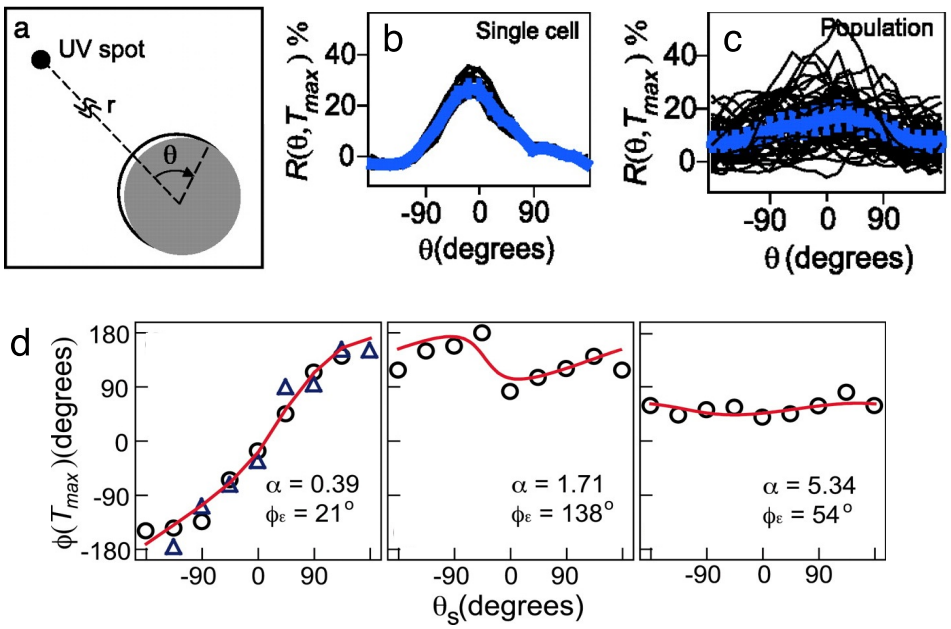

Figure 4.11: The geometric model for direction sensing. (a) PH_{CRAC}-GFP cells were stimulated by uncaging cAMP with a UV spot. (b) The translocation response of a single cell is highly reproducible, whereas (c) in a population, the response varies widely. (d) The polarization angle ϕ as a function of the direction of the applied gradient, θ for three different cells. The red lines show the fit provided by the geometric model. Adapted from [152], Copyright (2006) The National Acadamy of Sciences of the USA.

experiments have shown that the $G\alpha$ and $G\beta\gamma$ subunits remain disassociated as long as a cAMP signal is applied [87, 200, 201]. Therefore adaptation does not occur at the G-protein level.

Phenomonological model: All of the previously mentioned models treat each cell identically. Experiments exposing latrunculin-treated PH_{CRAC}-GFP cells to a well defined gradient of cAMP, however, show that there is a great deal of individuality between cells (figure 4.11a). In figures 4.11b and 4.11c, the translocation of PH_{CRAC}-GFP is plotted as a function of position along the membrane. Notice that for a single cell, the response is highly reproducible, but for a population of cells, the response varies widely [152].

To account for this individuality in cell response, A. Samadani et.al. devised the **geometric model** [152]. They proposed that the polarization response of a chemotactic cell is the product of an external signal with an internal signal:

$$S_{ext} = S_0 + S_1 \cos\theta, \tag{4.27}$$

$$S_{int} = 1 + \varepsilon \cos(\theta - \phi_\varepsilon), \tag{4.28}$$

$$S = S_{ext} \times S_{int} \tag{4.29}$$

Defining

$$L = S_0 + \frac{\varepsilon}{2} S_1 \cos\phi_\varepsilon, \tag{4.30}$$

$$P_x = S_1 + \varepsilon S_0 \cos\phi_\varepsilon, \tag{4.31}$$

$$P_y = \varepsilon S_0 \sin\phi_\varepsilon, \tag{4.32}$$

and using the approximation $\cos^2\theta \approx 1/2$, one finds that

$$S \approx L + \vec{P} \cdot \hat{r}. \tag{4.33}$$

In this model, the polarization response $\vec{P}$ of the cell lends itself readily to geometric interpretation: it is the sum of the applied polarization signal, $S_1 \exp(0i)$, and the internal polarization signal, $\varepsilon S_0 \exp(\phi_\varepsilon i)$. (Here we chose the x-axis to point along the gradient.) This model fits experimental data well, when an appropriate value for the internal polarization vector is chosen. See figure 4.11d.

Stochasticity: It has been shown that a population of *D. discoideum* cells is capable of chemotaxis in weak gradients, where the average difference in the number of receptors in the front versus the back of a cell was estimated to be around 10 [164]. As the number of molecules involved in chemotaxis can be quite small, noise plays an important role in the direction sensing process [17]. Recently, there has been a great theoretical effort to examine the properties of the

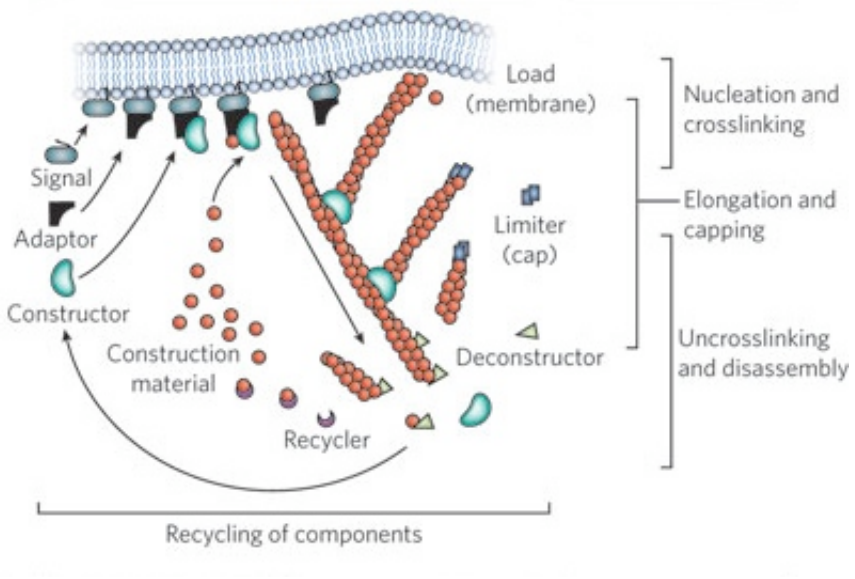

Figure 4.12: Assembly of branched filamentous actin networks. Existing filaments elongate until they are capped. At the front, new filaments are nucleated by Arp2/3, and stabilized by crosslinkers. To free up actin monomers, the filaments uncrosslink and disassemble at the back. Reprinted by permission from Macmillan Publishers Ltd: [59], Copyright (2010).

extrinsic (receptor-level) and intrinsic (e.g. amplification by LEGI or balanced inactivation mechanism) noise, and to investigate how the cells are able to optimally filter this noise. For more information, consult references [6, 147, 183, 64].

4.3 Motility

Once the cell has determined which direction to move, it undergoes amoeboid motility: (i) The cell, rigidly attached to the substrate, extends a membrane protrusion at the leading edge. (ii) This protrusion, called a pseudopod, adheres to the the substrate. (iii) The cytosol flows into the pseudopod and the cell's center of mass moves forward. (iv) Finally, the rear of the cell detaches from the substrate [123].

What is the driving force for the membrane protrusion at the leading edge? The prevailing theory is actin polymerization. Nucleation promoting factors SCAR (WAVE) and WASP activate the Arp2/3 complex at the front of the cell. This activated Arp2/3 complex forms a nucleation site for actin polymerization off the side of a pre-existing actin filament. The elongation of existing filaments and the nucleation of daughter filaments create a dendritic meshwork of actin that grows against the leading edge, pushing out the pseudopod. This meshwork is stabilized by crosslinkers acting at the leading edge. Near the rear of this network, the filaments uncrosslink and disassemble to free up monomeric actin to be used at the at the front. See figure 4.12 and references [59, 72, 98, 124, 136] for more details on actin polymerization.

Another mechanism for membrane protrusion is blebbing. A bleb forms when a portion of the membrane detaches from the actin cytoskeleton. The hydrostatic pressure inside the cell causes this detached membrane to balloon into a bubble, called a bleb. Although blebbing has often been dismissed as a sign of pathology in the past, it has gained much attention recently, as an important component to cell motility [32]. K. Yoshida and T. Soldati (2006), have shown that blebs form at the leading edge of chemotactic *D. discoideum* cells, and when blebbing is suppressed by raising the solution's osmolarity, the chemotactic velocity decreases [203]. Still, little is known about how the chemotactic pathways regulate blebbing [98].

A noteworthy, but more controversial model for cell migration is the membrane flow hypothesis [30, 31, 77]. In this model, membrane is taken up throughout the cell via endocytosis and re-deposited to the leading edge via exocytosis. The adhesion proteins are also taken up in this process and redeposited in the front. From the reference frame of the cell, there is a net backwards flow: mem-

brane is deposited in the front, and then moves backwards until it is taken up. Early evidence for this membrane flow was seen with the rearward movements of particles attached to the dorsal surface of fibroblasts [1] and the rearward movement of cross-linked antigen patches on lymphocytes [173].

In the actin cytoskeleton model presented above, there is no such membrane flow relative to the cell. Instead, the cell membrane is dragged along with the cell. This means that the membrane on the ventral side is sliding forward with respect to the substrate. What then, is pushing back on the substrate in order to propel the cell forward? It must be transmembrane adhesion proteins which link the actin cytoskeleton to the substrate below. Experimental evidence for the anchoring of the cytoskeleton to the substrate was observed using fluorescence activation in goldfish keratocytes [175]. These cells were injected with CR-actin, which becomes fluorescent when activated with short wavelength light. A bar shaped region was activated in the lamellopod (the frontal protrusion), and tracked. Over time, this region remain fixed relative to the substrate.[12]

In the membrane flow model, there is a net backwards flow of membrane relative to the cell. In the actin cytoskeleton model, it isn't the membrane that is moving backwards; rather it is the actin cytoskeleton that moves backwards with respect to the cell. Particles and antigen patches were observed to move backwards because they were being linked, via an adhesion protein, to the backward moving cytoskeleton—they were being *raked* backwards [31]. This claim has been supported by a detailed investigation in which the movement of individual gold particles on keratocytes was tracked [107]. Two types of motion were observed: (i) a systematic rearward drift, or (ii) random diffusion with no drift. The random motion would seem to correspond to the particle siting on the

[12]This is similar to what we have observed in *D. discoideum* – often a lateral pseudopod will remain in place with respect to the substrate; as the cell moves forward these lateral protrusions eventually are absorbed into the back of the cell.

plasma membrane, whereas the directed rearward motion would correspond to a particle that has been linked to the underlying cytoskeleton. Experiments tracking photobleached membrane regions in leukocytes [110] and *D. discoideum* [179] cast further doubt on the membrane flow hypothesis. Yet, this matter is not closed, as some evidence for directed endocytic recycling in leukocytes has also been reported [137].

CHAPTER 5

CHEMOTACTIC RESPONSE TIME VERSUS CELL SIZE

As we saw in §4.2, most models for direction sensing depend on a rapidly diffusing global inhibitor to facilitate the communication between the front and the back of the cell. The characteristic time scale for this diffusion is $\sim L^2/D$, where L is the length of the cell and D is the diffusion coefficient of the biochemical messenger. D ranges from about $10\,\mu\text{m}^2/\text{s}$ for small proteins up to $100\,\mu\text{m}^2/\text{s}$ for small molecules like nucleotides [9], while the typical size of a cell is 10 μm. Therefore, the time scale for diffusion across the cell is on the order of 1-10 s, which coincidentally, is also the time scale at which we see the translocalization of many proteins in response to an external cAMP signal. Consequently, we decided to stimulate cells, flattened to various degrees, with photo-activatable (caged) cAMP to look for a dependence between the characteristic response time for protein translocalization and the size of the cell. If we could determine this relationship, then we would gain some insight into direction sensing.

5.1 Materials and methods

We examined the timings in the PIP_3 pathway by using PH_{CRAC}-GFP cells, and the timings of events further downstream with cells containing LimE-GFP, a marker for filamentous actin. A syringe, containing developed PH_{CRAC}-GFP or LimE-GFP cells, was connected to the inlet of a nominally 5 μm tall, single layer, high aspect ratio chamber (figure 2.2b) via 24 gauge tubing. Cells were then injected into the chamber, and allowed to settle over 10-15 minutes. After the cells settled, the loading syringe was removed, and replaced with a syringe containing a 5 μM DMNB-caged cAMP solution. For the experiments

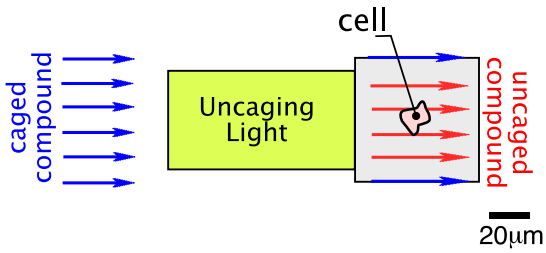

Figure 5.1: Geometry of the uncaging (yellow) and imaging (light gray) regions. Adapted from [10] – Reproduced by permission of The Royal Society of Chemistry (RSC).

that did not involve cell flattening, the syringe was driven by a syringe pump (PHD2000, Harvard Apparatus) to infuse the solution through the chamber at a rate of 3 μL/hr. For cell flattening experiments, a reservoir of caged cAMP was connected to the outlet, and the syringe pump was set to withdraw fluid at a rate of 3-6 μL/hr. Withdrawing fluid through the microfluidic device caused the pressure inside the chamber to drop below atmospheric pressure. This pressure differential induced the elastic chamber ceiling to collapse into the cells. By varying the flow rate, the degree of flattening could be adjusted [194].

Imaging of the cells was performed on an inverted confocal laser scanning microscope (FV1000, Olympus) equipped with two scanning units. One scanning unit was used for imaging a cell, while the other was used for quickly applying a stimulus to the cell with a technique developed in our laboratory, termed *flow photolysis* [21]: Caged cAMP is physiologically inert until it is activated in a microflow by short wavelength light. This light induces the cleavage of a photoliable bond, freeing the cAMP from its molecular cage. The active cAMP is then carried downstream to the cell for stimulation. The photoactivation region was chosen to be $93\,\mu\text{m}\times 50\,\mu\text{m}$ (150 $\times$ 80 pixels), directly upstream to the $62\,\mu\text{m}\times 62\,\mu\text{m}$ (100 $\times$ 100 pixels) imaging region. Images were taken at a frame rate $f = 6/\text{s}$.

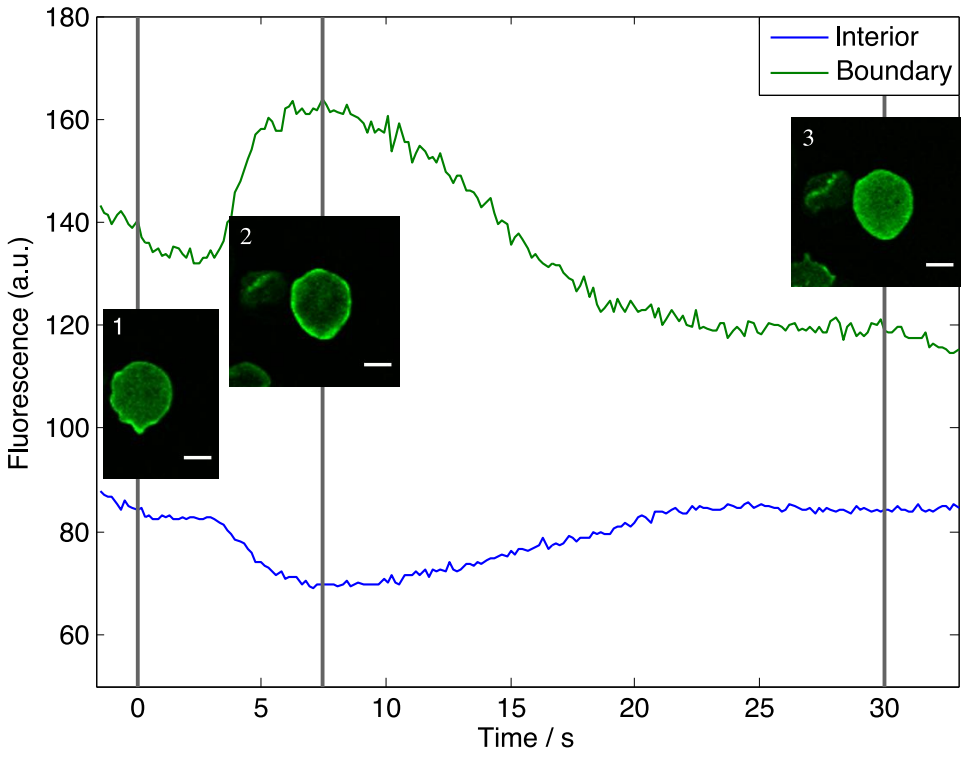

Figure 5.2: The translocalization of LimE-GFP to the cell cortex. The average fluorescence intensities along the boundary (green) and in the interior (blue) versus time. At $t = 0$, a continuous cAMP signal is applied. The insets show the cell (1) initially, (2) when the LimE-GFP translocation is maximal, and (3) after recovery. Scale bar=10 μm.

5.2 Results

The images were thresholded to separate the background region from the foreground, which corresponds to the cell. The average cell size was then calculated over time. The cell image was subsequently segmented into a 2 μm thick[1] boundary region and the interior to the boundary. The average intensity in each region was calculated over time. In figure 5.2, we see that the average intensity in the boundary region reflects the accumulation of LimE-GFP in the cortex, while the intensity in the interior reflects the depletion of LimE-GFP in the cytosol. Next we defined the response as the ratio of the average intensity in the

[1]Although the boundary 2 μm thickness is a somewhat arbitrary, rest assured the time at which the maximal response occurs is relatively insensitive to the value chosen.

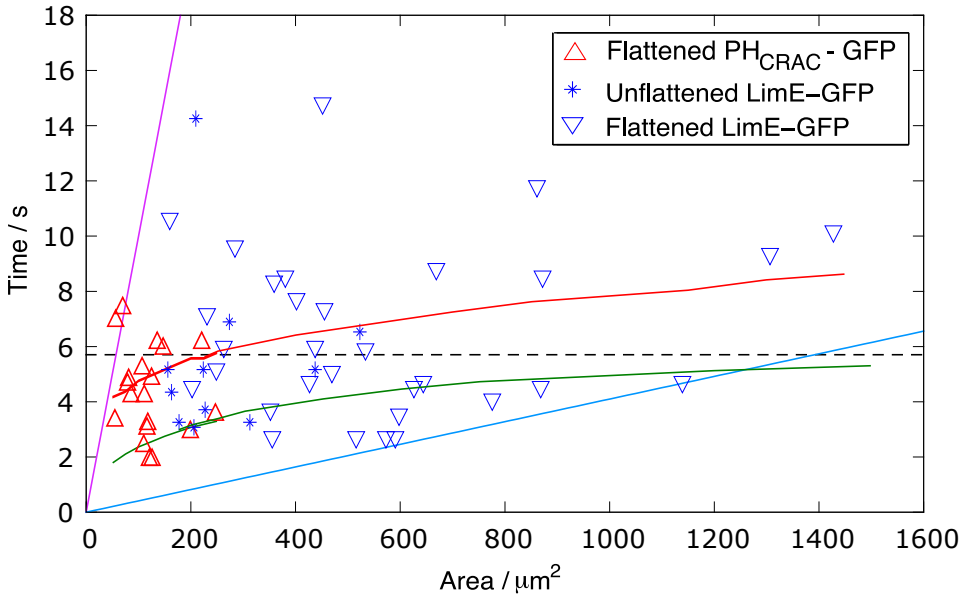

Figure 5.3: The time between cAMP stimulation and maximal response for PH_{CRAC}-GFP (red triangles) and LimE-GFP localization (blue triangles and asterisks). Note that the LimE response is thought to be downstream of the PH_{CRAC} response; therefore, there might be a slight delay between the two (not adjusted here). The dashed horizontal line shows the average response time, 5.7 s. The solid magenta and blue lines would provide the lower limits for switching if the response was diffusion limited with diffusion coefficients of $D = 10\,\mu m^2/s$ and $D = 244\,\mu m^2/s$, respectively. The solid green and red curves show the expected response times based on the balanced inactivation theory [146], and the LEGI model of [116]. An offset of 1.4 s was subtracted from the data to account for the time it takes to apply the signal (see §6.5).

the boundary to the average intensity in the interior. We recorded the time for maximal response.

This maximal response time and cell area were measured for several different cells (figure 5.3). The data are highly scattered, showing little correlation between response time and area: for PH_{CRAC}, the correlation coefficient is r = -0.16 with p = 0.52, and for LimE-GFP, r = 0.16 with p = 0.31.

If diffusion provided the bottleneck in the response times, as we initially assumed, then the data points in figure 5.3 should lie above the line $t = D^{-1}A$, where A is the cell's area, and D is the diffusion coefficient of the communication

molecule. In figure 5.3, we see that the lowest diffusion coefficient that meets this criterion is $D = 244\,\mu\text{m}^2/\text{s}$. We might then conclude that the chemotactic messenger has a diffusion coefficient greater than this number.

The actual situation is a bit more subtle. In figure 5.3, we display the theoretical predictions from two of the direction sensing models: the green curve corresponds to the activator response time in the balanced inactivation model [146], and the red curve corresponds to the PIP_3 response time in the two complementary LEGI mechanism model [116]. These models contain a diffusive inhibitor ($D \sim 10\,\mu\text{m}^2/\text{s}$) that facilitates communication between the front and back. Note that for the values of A we consider, these model curves lie beneath the line $t = D^{-1}A$, so in the context of these models, diffusion is not the bottleneck. Although the LEGI model appears in better agreement with the data, the results are not definitive. There is simply too much variability in the data.

The large variability in the time it takes for the cells to respond (i) may be intrinsic to each cell, (ii) may be due to variability between cells (individuality), or (iii) may simply be due to a fault in the experimental design. Maybe the time it takes for the external cAMP signal to reach the cell is highly variable. In the next chapter we examine the speed of flow photolysis to ultimately rule out the third possibility.

CHAPTER 6

LIMITS TO HOW QUICKLY A CHEMICAL SIGNAL CAN BE APPLIED

In this chapter, we ask ourselves how quickly can we apply a chemical signal using flow photolysis? What factors limit the speed? And how does our method compare with the other techniques for applying a temporally varying chemical signal? In this chapter, we answer these questions by applying the theory of G.I. Taylor [172] and R. Aris [7].[1]

6.1 Taylor-Aris theory

In a seminal work, G.I. Taylor examined how a plug of diffusible solute evolves in laminar fluid flow through a small-bore cylindrical tube [172]. He showed that the plug remains plug-like, moving with the mean fluid velocity, and spreading axially with an effective diffusion coefficient that is proportional to the squared mean velocity, and inversely proportional to the solute's diffusion coefficient.

This is a remarkable, somewhat counter-intuitive result. Assume that you have water flowing in such a pipe, and that at some location along the pipe, there is a small plug of dyed water. The flow profile is parabolic, with the speed being zero at the boundary, and twice the mean along the center. Taylor says that the plug of dye moves with the mean velocity. So, along the center of the pipe, the clear water behind the plug is moving at twice the speed of the plug. This water would appear to catch up to the plug, pick up some color, and then pass through plug becoming clear again. Similarly, the water near the boundary isn't moving, so it appears as though the plug is moving through this clear water, leaving behind a trail of clear water. Furthermore, we would expect that the

[1]This chapter contains material published in Ref [10]: A. J. Bae, C. Beta, and E. Bodenschatz, *Lab Chip* **9**:3059-65 – Reproduced by permission of The Royal Society of Chemistry.

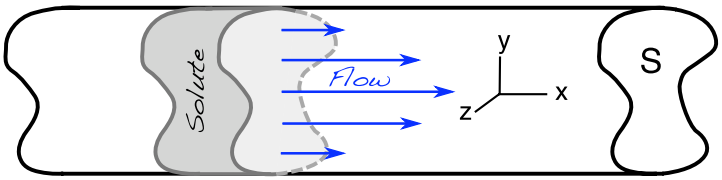

Figure 6.1: Geometry for the Aris theory. A solvent flows through a uniform pipe with arbitrary cross-section S. A section of this pipe contains a plug of diffusible solute. We choose the x coordinate to run along the direction of flow, and look at how the plug of solute evolves with time.

rate at which the dye spreads should be directly proportional to the diffusion coefficient, and not inversely proportional.

Without going into the details of Taylor's derivation, we can understand what is happening the following way. In absence of diffusion, the concentration profile would reflect the flow profile. As time evolves, axial spreading of the plug occurs: the solute next to the boundaries does not move, whereas the center of the plug is convected at twice the mean flow velocity. Now, when we take diffusion into account, we see that diffusion in radial direction will attempt to make the concentration uniform along a cross-section. This prevents the formation of a parabolic concentration profile. It is diffusion that keeps the plug together—convection tries to spread the plug axially, and diffusion prevents this from occurring. Hence, we get the result that the effective diffusion coefficient is inversely proportional to the solute's diffusion.

To visualize this, we return to the example of dyed water being convected through a pipe. Let's look at the concentration front. At the center of the pipe, the dye is convected forward at twice the mean velocity. Along the boundaries, however, there is no convection to move the dye forward. As the dye in the center of the pipe moves forward, it quickly gets diluted because it diffuses radially outward towards the boundaries. Along the back of the plug, the water along the pipe boundary isn't moving, but there is fresh water being supplied

along the center. So in the back, the diffusion causes the dye to move in radially. Taylor's initially counter-intuitive result should now make sense.

R. Aris generalized Taylor's result to tubes of arbitrary, uniform cross-section [7]. Here, we will follow his derivation for calculating the effective diffusion coefficient. Consider a pipe with uniform cross-section S, containing a plug of solute (figure 6.1). Let's denote the cross-sectional area as A, and let's choose $\hat{x}$ to run in the direction of flow.

Under laminar flow conditions, the flow velocity $\vec{u}$ contains no x dependence, so we can write:

$$\vec{u}(x,y,z) = \overline{u}\left[1 + \chi(y,z)\right]\hat{x}. \tag{6.1}$$

Here, $\overline{u} = \frac{1}{A}\iint_S u(y,z)dydz$ is the mean speed.[2] The function $\chi : S \to [-1,\infty)$, therefore, represents the deviation from the mean velocity.

The solute concentration c, will evolve according to the convection-diffusion equation:

$$\begin{aligned}\frac{\partial c}{\partial t} &= D\nabla^2 c - \vec{u}\cdot\vec{\nabla}c \\ &= D\nabla^2 c - \overline{u}\left[1+\chi(y,z)\right]\frac{\partial c}{\partial x},\end{aligned} \tag{6.2}$$

with the no flux boundary condition on ∂S

$$\frac{\partial c}{\partial n} = 0, \tag{6.3}$$

and initial condition

$$c_0(x,y,z) = c(x,y,z,0). \tag{6.4}$$

We denote the normal derivative as $\partial/\partial n$.

[2]For the remainder of this chapter, we will represent averages over the cross-sectional area with an over-bar.

To simplify the analysis, let's use non-dimensional variables and shift reference frames to one moving with the mean velocity:

$$\begin{aligned} x' &= (x - \bar{u}t)/a, \\ y' &= y/a, \\ z' &= z/a, \\ t' &= Dt/a^2, \end{aligned} \tag{6.5}$$

and

$$c'(x', y', z', t') = \frac{a^3\, c(x, y, z, t)}{\int_{-\infty}^{\infty} dx \iint_S c\, dydz}.$$

Here, a is a characteristic length scale for the cross-section. In addition, let us define the Péclet number $Pe_a = \bar{u}a/D$.

With this variable change, the convection-diffusion equation (6.2) becomes

$$\frac{\partial c'}{\partial t'} = \nabla'^2 c' - Pe_a \chi \frac{\partial c'}{\partial x'} \tag{6.6}$$

with boundary condition

$$\frac{\partial c'}{\partial n'} = 0 \quad \text{on} \quad \partial S, \tag{6.7}$$

and initial condition

$$c'_0(x', y', z') = c'(x', y', z', 0). \tag{6.8}$$

For the sake of convenience, we will drop the prime notation for the remainder of this section, with the understanding that we are working with these dimensionless variables.

Let us define the moment functions:

$$\mathfrak{c}_p(y, z, t) = \int_{-\infty}^{\infty} x^p c(x, y, z, t) dx \tag{6.9a}$$

$$\mathfrak{m}_p(t) = \frac{1}{A} \iint_S \mathfrak{c}_p dydz \tag{6.9b}$$

Combining (6.9a) with (6.6) and integrating by parts, we get

$$\frac{\partial \mathfrak{c}_p}{\partial t} = \nabla^2 \mathfrak{c}_p + p\, Pe_a \chi \mathfrak{c}_{p-1} + p(p-1)\mathfrak{c}_{p-2} \tag{6.10}$$

with boundary condition

$$\frac{\partial \mathfrak{c}_p}{\partial n} = 0 \quad \text{on} \quad \partial S, \tag{6.11}$$

and initial conditions

$$\mathfrak{c}_{p0}(y', z') = \mathfrak{c}_p(y', z', 0). \tag{6.12}$$

Averaging (6.10) over S, and using Greens theorem with (6.11), we get

$$\frac{d\mathfrak{m}_p}{dt} = p\, Pe_a \overline{\chi \mathfrak{c}_{p-1}} + p(p-1)\overline{\mathfrak{c}_{p-2}}. \tag{6.13}$$

We express the initial conditions as

$$\mathfrak{m}_{p0} = \mathfrak{m}_p(0). \tag{6.14}$$

Now, let's examine the $p = 0$ moment. From (6.13), we see that $\mathfrak{m}_0$ is constant in time. Furthermore, due to how we redefined our concentration in (6.5), $\mathfrak{m}_0 = 1$. If we plug $p = 0$ into (6.10), we have that

$$\begin{aligned} &\tfrac{\partial \mathfrak{c}_0}{\partial t} = \nabla^2 \mathfrak{c}_0 \\ &\tfrac{\partial \mathfrak{c}_0}{\partial n} = 0 \quad \text{on} \quad \partial S \\ &\mathfrak{c}_0(y', z', 0) = \mathfrak{c}_{00}(y', z'). \end{aligned} \tag{6.15}$$

Without much loss of generality, we can write the solution as

$$\mathfrak{c}_0(y, z, t) = 1 + \sum_{n=1}^{\infty} A_n \nu_n(y, z) \exp(-\lambda_n t), \tag{6.16}$$

where $\{\nu_n(y, z)\}$ is a complete sequence of eigenfunctions with a positive increasing sequence of eigenvalues $\{\lambda_n\}$ for the boundary value problem. The A_n are chosen to satisfy the initial conditions. From this solution, we see that the concentration will become uniform across a cross-section of the tube with a relaxation time on the order of $1/\lambda_1$.

Moving onto the first moment, $p = 1$, and noting that $\overline{\chi} = 0$, we get that

$$\mathfrak{m}_1 = Pe_a \sum_{n=1}^{\infty} \int_0^t A_n \exp(-\lambda_n t) \overline{\chi \nu_n} dt, \tag{6.17}$$

For $t \gg 1/\lambda_1$, this approaches a steady value of

$$\mathfrak{m}_{1\infty} = \sum_{n=1}^{\infty} A_n \lambda_n^{-1} \overline{\chi \nu_n} dt. \tag{6.18}$$

The first moment corresponds to the center of mass. Since we are in a reference frame moving with the mean flow velocity, the fact that the center of mass approaches a constant value indicates that a plug of solute will move with the mean flow.

For large times, $\mathfrak{c}_1$ should also approach a steady state. We can write $\mathfrak{c}_1 = \overline{\mathfrak{c}_1} + Pe_a \varphi(y, z)$, where $\overline{\varphi} = 0$. Neglecting the decaying terms, we end up with $\overline{\mathfrak{c}_1} = \mathfrak{m}_{1\infty}$. Futhermore, since $\mathfrak{c}_0 \approx 1$, equation (6.10) gives us that

$$\begin{aligned} \nabla^2 \varphi &= -\chi \\ \frac{\partial \varphi}{\partial n} &= 0 \quad \text{on} \quad \partial S. \end{aligned} \tag{6.19}$$

For time $t \gg \lambda_1^{-1}$, the evolution for the second moment now can be written as

$$\frac{1}{2} \frac{d\mathfrak{m}_p}{dt} = 1 + \overline{\chi \varphi} Pe_a^2. \tag{6.20}$$

Defining the effective diffusion constant K as half the growth rate of the variance and restoring dimensions, we get

$$\begin{aligned} K &= D(1 + \kappa Pe_a^2) \\ &= D + \kappa \frac{\overline{u}^2 a^2}{D} \end{aligned} \tag{6.21}$$

The constant $\kappa = \overline{\chi \phi}$ is a geometric factor. To show that the concentration profile actually approaches a normal distribution, Aris continues the derivation for higher moments, but we will stop here.

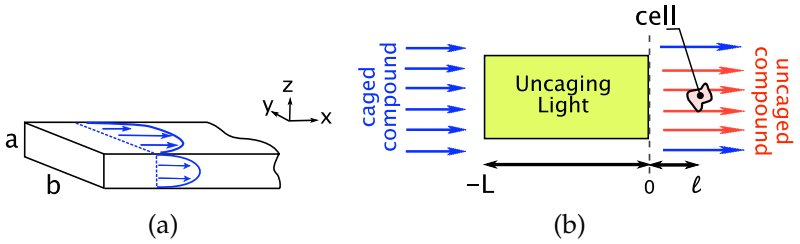

Figure 6.2: (a) Geometry of a rectangular microfluidic flow chamber. The reference frame is chosen such that x increases in the direction of fluid flow, y increases across the channel, and z points vertically up the channel. (b) Schematic top view of a photo-uncaging setup (x–y plane). The area illuminated by the uncaging light source is indicated in yellow and extends over a length of L in flow direction. For stimulation the cell is placed a distance l downstream of the illuminated region. Fluid flow runs from left to right.

6.2 Application to high aspect ratio micro-channels

Let us consider a micro-channel of height a and width b. Our reference frame is chosen such that x increases in the direction of flow (from left to right), y increases across the channel, and z points vertically from the bottom to the top of the channel, see figure 6.2(a).

The low Reynolds number flow profile in the channel is given by

$$\nabla^2 u = \frac{1}{\mu}\frac{dP}{dx} \equiv -\alpha, \tag{6.22}$$

where P is the pressure, and μ is the dynamic viscosity.

On the boundary ∂S, we have the no slip condition $u = 0$. The Fourier series for u then looks like

$$u(y,z) = \sum_{m=0}^{\infty}\sum_{n=0}^{\infty} A_{mn} \cos\left[\frac{\pi}{b}(2m+1)y\right] \cos\left[\frac{\pi}{a}(2n+1)z\right], \tag{6.23}$$

where

$$A_{mn} = \frac{4\alpha\gamma^2 a^2}{\pi^4} \cdot \frac{1}{(2m+1)(2n+1)} \cdot \frac{(-1)^m(-1)^n}{(2m+1)^2+\gamma^2(2n+1)^2}, \tag{6.24}$$

and $\gamma \equiv b/a$ is the aspect ratio.

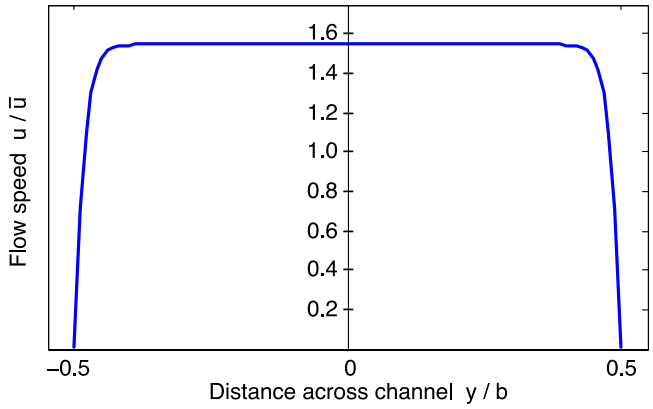

Figure 6.3: The flow profile across a high aspect ratio channel. Here $\gamma = 20$ and $z = a/2$. Notice that for most of the channel, the flow is independent of the y component, with the maximum flow speed being close to the standard, flat plate, parabolic flow value of $3\bar{u}/2$.

For high aspect ratio geometries, we see that, over most of the channel, the flow is independent of the y coordinate. See figure 6.3. In the case of y-independence, the flow profile is parabolic in z. That is,

$$u(y,z) = u_0 \left[1 - \left(\frac{2z}{a}\right)^2\right], \tag{6.25}$$

where $u_0 = a^2\alpha/8$ is the maximum velocity. The average flow velocity $\bar{u} = 2u_0/3$.

When using microfluidics for physiological applications, shear stresses must be kept below certain limits [43, 40]. The wall shear stress is given by $\tau = \mu\partial u/\partial n$. For high aspect ratio geometries, this becomes

$$\tau = 6\mu\bar{u}/a. \tag{6.26}$$

Appendix A, contains code for calculating the flow profile and wall shear stress for arbitrary aspect ratio micro-channels.

Let's assume that, in this channel, there is a cell located downstream of a chemical stimulant source. How quickly does the stimulant concentration seen by the cell change? The parameters that characterize this problem are the

height a and the width b of the micro-channel, the distance l that the cell is placed downstream of the source, the diffusion coefficient D of the solute, and the average flow velocity $\bar{u}$. From these, we can construct the Péclet numbers, $Pe = \bar{u}l/D$, $Pe_a = \bar{u}a/D$, and $Pe_b = \bar{u}b/D$. If parameters are changed such that the Péclet numbers remain constant, both the flow and the concentration profiles scale.

For wide and shallow microfluidic channels (large $\gamma = b/a$), we showed that, far from the sidewalls, the flow profile is independent of the y coordinate. With respect to the height coordinate z, the flow profile takes on a parabolic shape. Assuming that the concentration varies slowly in the y direction, the problem can be analyzed in two dimensions; i.e., the role of Pe_b is negligible.[3]

We can apply Taylor-Aris theory to further reduce the problem to one dimension. Recall that the effective one dimensional diffusion (dispersion) coefficient is given by

$$K = D(1 + \kappa Pe_a^2), \tag{6.27}$$

where $\kappa = \overline{\chi\varphi}$,

$$\chi(y, z) = \frac{u(y, z)}{\overline{u}} - 1, \tag{6.28}$$

and φ is the solution to

$$\begin{aligned} a^2\nabla^2\varphi &= -\chi, \quad \text{on } S \\ \tfrac{\partial\varphi}{\partial n} &= 0 \qquad \text{on } \partial S. \end{aligned} \tag{6.29}$$

We calculate χ for our high aspect ratio geometry:

$$\begin{aligned} \chi(y, z) &= \frac{1 - \left(\frac{2z}{a}\right)^2}{\int_{-1/2}^{1/2} [1 - (2\zeta)^2]\, d\zeta} - 1 \\ &= \frac{1}{2} - \frac{6z}{a}. \end{aligned} \tag{6.30}$$

[3]The switching time predicted under these assumptions should provide a lower limit on switching time in geometries where these conditions are not fulfilled.

The equations (6.29) for φ now read

$$\left.\begin{array}{ll} a^2\frac{d^2\varphi}{dz^2} & = \frac{1}{2} - \frac{6z}{a}, \quad \text{for } -a/2 < z < a/2 \\ d\varphi/dz & = 0, \qquad\quad \text{at } z = \pm a/2 \end{array}\right\}. \tag{6.31}$$

The solution is

$$\varphi = \frac{1}{2}\left(\frac{z}{a}\right)^4 - \frac{1}{4}\left(\frac{z}{a}\right)^2 + \frac{7}{480}. \tag{6.32}$$

We can now calculate the geometric factor κ:

$$\begin{aligned} \kappa &= \int_{-1/2}^{1/2} \left(\frac{\zeta^4}{2} - \frac{\zeta^2}{4} + \frac{7}{480}\right)\left(\frac{1}{2} - 6\zeta^2\right) d\zeta \\ &= \frac{1}{210}. \end{aligned} \tag{6.33}$$

Now we have the effective longitudinal diffusion:[4]

$$K = D + \frac{1}{210}\frac{a^2\overline{u}^2}{D}. \tag{6.34}$$

The Taylor-Aris theory is applicable only when diffusive transport across the channel height a is much faster than convective transport over the length l. The characteristic convective transport time, $t_{\text{convect}} = l/\bar{u}$, where l is the characteristic length scale. To calculate the characteristic vertical diffusion time, let us look at the evolution of a symmetric[5] concentration profile that only has z dependence:

$$\frac{\partial^2 c}{\partial z^2} = \frac{1}{D}\frac{\partial c}{\partial t}. \tag{6.35}$$

The solution is of the form

$$c(z,t) = \sum_{n=0}^{\infty} C_n \cos\left(\frac{2\pi n z}{a}\right) \exp\left(-\frac{4\pi^2 n^2 D}{a^2} t\right). \tag{6.36}$$

[4]This is the classic flat plate result [14, 47, 49]. For a pipe of rectangular cross section, we would expect to get this result as the aspect ratio $\gamma = b/a \to \infty$. However, this is not always the case. If you look a distance $l \gg b$ downstream, as $b/a \to \infty$, $\kappa \to 7.95/210$ [49, 47, 167]. Here, we have tacitly assumed that $l \ll b$, in which case the flat plate result holds. When this is not the case, the theory still provides a lower limit for switching times.

[5]Since the flow itself is symmetric about $z = 0$, the concentration profile it generates is also symmetric.

The slowest decaying mode, $n = 1$, has a time constant of

$$t_{\text{diffuse}} = \frac{a^2}{4\pi^2 D}. \tag{6.37}$$

Thus, we get the Taylor condition

$$\frac{a^2}{4\pi^2 D} \ll \frac{l}{\bar{u}}. \tag{6.38}$$

In terms of the Péclet numbers,

$$Pe_a^2 \ll 4\pi^2 Pe\,. \tag{6.39}$$

When this condition is satisfied, diffusion will remove vertical distortions of the concentration profile due to the parabolic flow profile. In the § 6.3.4, we will examine what the '$\ll$' means in greater detail.

6.3 Rapid switching by flow photolysis

Based on Taylor-Aris theory, we will perform a detailed analysis of the concentration switching times that can be obtained in flow photolysis setups. In § 6.4, these results will be compared to the temporal resolution in other live cell stimulation devices.

6.3.1 Device geometry and governing equations

Flow photolysis is a microfluidics-based approach for single cell stimulation with high spatiotemporal resolution. Here, we will briefly introduce the underlying principle. For more details, see [21]. The main idea of flow photolysis is illustrated in figure 6.2(b). A flow is established in a microfluidic channel that carries a physiologically inert, caged compound of initial concentration c_0. In the flow, a rectangular region, of length L, is illuminated with short wavelength

light (uncaging region). The wavelength of the uncaging light source is chosen such that it cleaves the photoliable bond between the caging group and the physiologically active part of the caged compound. The released active substance is then carried across the cell downstream by the fluid flow. A distance l downstream of the uncaging region, the target for chemical stimulation—in most cases a living cell—is placed.

If we turn on the uncaging light at $t = 0$, then we can describe the evolution of the concentrations for uncaged (c) and caged (c_2) material in the channel as follows:

$$\frac{\partial c}{\partial t} = -\bar{u}\frac{\partial c}{\partial x} + K\frac{\partial^2 c}{\partial x^2} + c_2 f(x,t) \tag{6.40a}$$

$$\frac{\partial c_2}{\partial t} = -\bar{u}\frac{\partial c_2}{\partial x} + K_2\frac{\partial^2 c_2}{\partial x^2} - c_2 f(x,t) \tag{6.40b}$$

with the initial conditions

$$c(x,0) = 0 \tag{6.41a}$$

$$c_2(x,0) = c_0. \tag{6.41b}$$

The function $f(x,t)$ describes the release of material under uncaging region:[6]

$$f(x,t) = \begin{cases} \sigma\phi I & \text{for } -L \le x \le 0 \text{ and } t > 0 \\ 0 & \text{otherwise} \end{cases}, \tag{6.42}$$

here I is the light intensity, σ is the absorption cross-section, and ϕ is the quantum yield.

If the diffusivity of the caged compound is markedly different from that of the uncaged species, e.g. caged calcium, we should solve the coupled equations (6.40) numerically.

[6]We have assumed that the time-scale for the bond cleavage is insignificant compared to the other time scales involved in the problem.

If we can assume that the diffusion coefficients of the caged and uncaged substance are comparable, as is the case for many nucleotides, then $K = K_2$. By adding equations (6.40a) and (6.40b), we can see that the total concentration follows the convection-diffusion equation. Furthermore, we see that the initial condition is uniform—add (6.41a) and (6.41b) together. Therefore, the total concentration is constant in time and space: $c + c_2 = c_0$. We can rewrite (6.40) as

$$\frac{\partial c}{\partial t} = -\bar{u}\frac{\partial c}{\partial x} + K\frac{\partial^2 c}{\partial x^2} + (c_0 - c)f(x,t) \tag{6.43}$$

Let's introduce the dispersive length scale $\eta_K = K/\bar{u}$, dispersive time scale $\tau_K = K/\bar{u}^2$, photolysis time scale $\tau_p = (\sigma\phi I)^{-1}$, and residence time $\tau_r = L/\bar{u}$. By expressing all lengths in units of η_K, all times in τ_K, and concentration in units of c_0 we get the dimensionless form of (6.43):

$$\frac{\partial c}{\partial t} = -\frac{\partial c}{\partial x} + \frac{\partial^2 c}{\partial x^2} + (1 - c)f(x,t)\,, \tag{6.44}$$

where

$$f(x,t) = \begin{cases} {\tau_p}^{-1} & \text{for } -\tau_r \le x \le 0 \text{ and } t > 0 \\ 0 & \text{elsewhere.} \end{cases} \tag{6.45}$$

Note that here, $\tau_r = L$. Unless it is stated otherwise, we will continue to use dimensionless variables for the rest of this section.[7]

6.3.2 Steady state solution

Before we examine the time dependent solutions to the (6.44), let's look at the steady state. By setting $\frac{\partial c}{\partial t} = 0$, we get

$$\frac{d^2 c}{dx^2} - \frac{dc}{dx} + (1 - c)f(x) = 0. \tag{6.46}$$

[7] Don't confuse the dimensionless form used here with that used in §6.1.

The full solution to this equation, with the condition that $c \to 0$ when $x \to -\infty$, is

$$c = \begin{cases} A_0 e^x & \text{for } x < -\tau_r \\ A_1 e^{\lambda_1 x} + A_2 e^{\lambda_2 x} + 1 & \text{for } -\tau_r \leq x \leq 0 \\ A_3 & \text{for } x > 0 \end{cases} \tag{6.47}$$

Here,

$$\lambda_{1,2} = \frac{1}{2}\left(1 \pm \sqrt{1 + 4/\tau_p}\right), \tag{6.48}$$

and the A_i's are given by the continuity of c and dc/dx at $x = -\tau_r$ and $x = 0$:

$$\begin{aligned} A_0 &= \frac{\lambda_1(-\lambda_2)e^{\tau_r}(e^{-\lambda_2\tau_r} - e^{-\lambda_1\tau_r})}{\lambda_1^2 e^{-\lambda_2\tau_r} - \lambda_2^2 e^{-\lambda_1\tau_r}} \\ A_1 &= -\frac{-\lambda_2}{\lambda_1^2 e^{-\lambda_2\tau_r} - \lambda_2^2 e^{-\lambda_1\tau_r}} \\ A_2 &= -\frac{\lambda_1}{\lambda_1^2 e^{-\lambda_2\tau_r} - \lambda_2^2 e^{-\lambda_1\tau_r}} \\ A_3 &= 1 - \frac{\lambda_1 - \lambda_2}{\lambda_1^2 e^{-\lambda_2\tau_r} - \lambda_2^2 e^{-\lambda_1\tau_r}} \end{aligned} \tag{6.49}$$

There are two interesting limiting cases. The first case is when the uncaging light intensity is high, where we would expect everything to be uncaged. The second case is that of low light intensity, where we expect to see a linear dependence of the uncaged concentration with the length and brightness of the uncaging region.

Low Light Intensity Regime: When $\tau_p \gg 1$, we have that $\lambda_1 = 1 + 1/\tau_p$ while $\lambda_2 = -1/\tau_p$. Using this with $|\lambda_1| \gg |\lambda_2|$, we get the concentration to the right of the uncaging region

$$c(x > 0) = 1 - \exp\left(-\frac{\tau_r}{\tau_p}\right). \tag{6.50}$$

Under the additional limiting condition that the photolysis time scale is greater than the residence time, $\tau_p \gg \tau_r$, we obtain:

$$c(x > 0) = \frac{\tau_r}{\tau_p}. \tag{6.51}$$

Restoring our original units for length, time, and concentration,

$$c(x > 0) = \frac{c_0 \sigma \phi I L}{\bar{u}}. \tag{6.52}$$

C. Beta et al. demonstrated that the concentration profile of the uncaged substance downstream of the illuminated region can be modified by changing the shape of the uncaging area [21]. In the low light, low residence time regime, we see that the extension of the uncaging area in the flow direction (x) is linearly mapped to the amount of uncaged substance.

Saturating Regime: When $\tau_p \ll 1$, we see that

$$\begin{aligned} \lambda_1 &= -\lambda_2 \\ &= \sqrt{1/\tau_p} \gg 1. \end{aligned} \tag{6.53}$$

The concentration to the right of the uncaging region

$$c(x > 0) = 1 - \frac{2\lambda_1}{\lambda_1^2 (e^{\lambda_1 \tau_r} + e^{-\lambda_1 \tau_r})} \tag{6.54}$$

The second term is negligible, and thus,

$$c(x > 0) = 1, \tag{6.55}$$

or in original units, $c(x > 0) = c_0$.

6.3.3 Time dependent solution

We will now turn to the dynamics of the switching event. For both the linear and the stationary regime, the derivations of the time dependent solutions of (6.44) are presented.

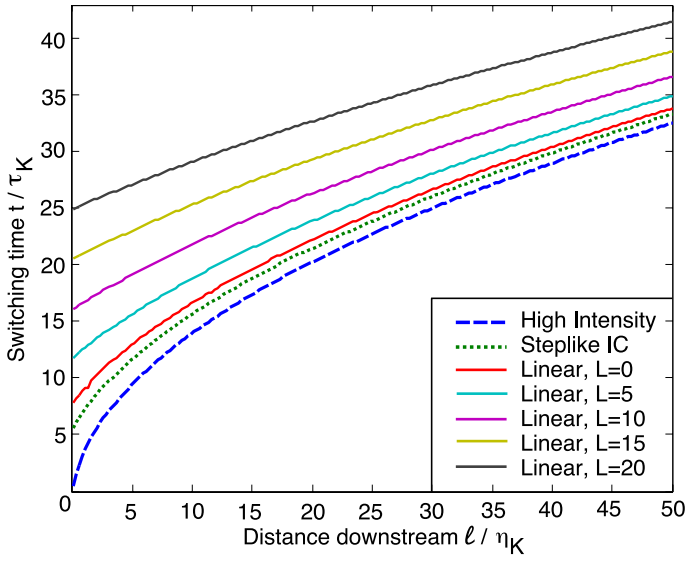

Figure 6.4: Switching time as a function of the distance downstream of the source. The switching time is defined as the time interval for the concentration to rise from 5% to 95% of its final value. The dashed blue line shows switching in a flow photolysis device in the saturating regime (for high light intensities). The dynamics of valve-mediated switching and interface shifting, i.e., for a step-like initial condition, is displayed with the green dashed line. The red, light blue, purple, yellow, and black curves show switching times in a flow photolysis device that is operated in the linear regime (for low light intensities) for different uncaging region lengths, $L = 0$, 5, 10, 15, and 20 η_K.

Linear regime: In the linear regime ($\tau_p \gg 1$ and $\tau_p \gg \tau_r$), the uncaged concentration is far from being saturated, i.e. $c \ll 1$. Then, equation 6.44 reads

$$\frac{\partial c}{\partial t} + \frac{\partial c}{\partial x} - \frac{\partial^2 c}{\partial x^2} = \begin{cases} {\tau_p}^{-1} & \text{for } -\tau_r \le x \le 0 \\ 0 & \text{elsewhere} \end{cases} \tag{6.56}$$

We get the solution to this equation by convolving the inhomogeneous source term with the Green function:

$$\begin{aligned} c(x,t) &= \int_0^t \int_{-\tau_r}^0 \left\{ \frac{{\tau_p}^{-1}}{\sqrt{4\pi(t-\tau)}} \exp\left[-\frac{(x-\xi-t+\tau)^2}{4(t-\tau)} \right] \right\} d\xi d\tau \\ &= \frac{1}{2\tau_p} \int_0^t \left[\text{erf}\left(\frac{x+\tau_r-t+\tau}{2\sqrt{t-\tau}} \right) - \text{erf}\left(\frac{x-t+\tau}{2\sqrt{t-\tau}} \right) \right] d\tau \end{aligned} \tag{6.57}$$

We obtain the switching time, which we define as the time interval for the concentration $c(l,t)$ to rise from 5% to 95% of its final value. The switching time

increases with increasing residence time $L/\bar{u}$. In figure 6.4, the switching time in the linear regime for $L = 0, 5, 10, 15$, and $20\,\eta_K$ is shown by the red, light blue, purple, yellow, and black lines.

Saturating Regime: In the high light intensity case ($\tau_p \ll 1$), everything underneath the light source is uncaged, so we can find the concentration to the right of the uncaging light by solving the convection-diffusion equation

$$\frac{\partial c}{\partial t} = -\frac{\partial c}{\partial x} + \frac{\partial^2 c}{\partial x^2}, \tag{6.58}$$

with the boundary condition

$$c(x = 0, t) = 1, \tag{6.59}$$

and the initial condition

$$c(x > 0, 0) = 0. \tag{6.60}$$

The equation can be solved by taking a Laplace transform in time and solving the ordinary differential equation in space.[8] The solution reads

$$c(x,t) = \frac{e^{x/2}}{2}\left[e^{x/2}\text{erfc}\left(\frac{x+t}{2\sqrt{t}}\right) + e^{-x/2}\text{erfc}\left(\frac{x-t}{2\sqrt{t}}\right)\right]. \tag{6.61}$$

Again we define the switching time as the time for the concentration to rise from 5% to 95% of its final value. This switching time, as a function of the distance l, is shown by the dashed blue line in figure 6.4. Note that switching in the linear regime is always slower than in the saturating regime. Yet, for generating spatially varying concentration profiles, it is often desirable to operate in the linear regime.

[8] For example, see [119].

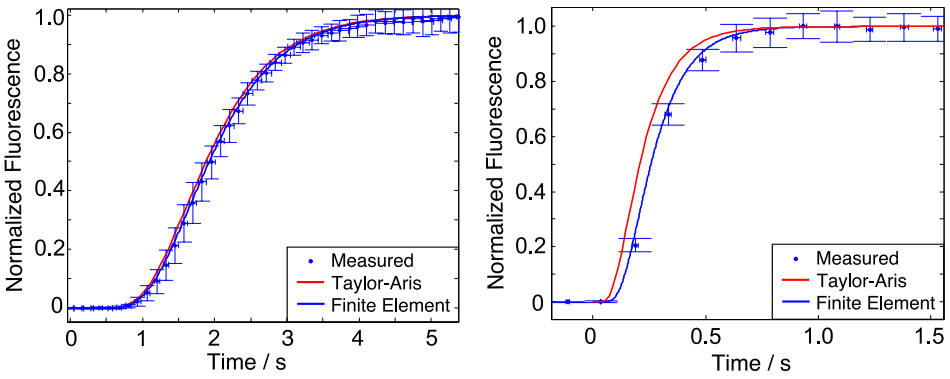

(a) $Pe = 14$, $Pe_a = 4.2$ (b) $Pe = 9.8$, $Pe_a = 10$.

Figure 6.5: Concentration switching in the flow photolysis device. Comparison between experimental data (blue points), numerical finite element simulation (blue line), and analytic prediction according to the Taylor-Aris dispersion theory.

6.3.4 Limits of the Taylor-Aris prediction

To explore the limits of the theoretical predictions presented above, we have conducted photo-activation measurements with a caged dye and performed numerical finite element simulations of the flow photolysis setup.

Experimental results: We used a large aspect ratio microchannel of height $a = 26\,\mu$m and width $b = 500\,\mu$m. A continuous fluid flow, carrying a 10 μM solution of dextran conjugated 4,5-dimethoxy-2-nitrobenzyl (DMNB)-caged fluorescein, $D = 267\,\mu m^2/s$ was established in the channel. Switching events were initiated by a 405 nm laser uncaging light source. We measured the increase of fluorescence intensity a distance l downstream of the uncaging region, near the bottom of the channel. Two sets of measurements were acquired at different distances l and different flow velocities $\bar{u}$. In both cases, the width of the uncaging region is negligible compared to the length scale l; i.e., $L \ll l$.

The first measurement set was taken at a distance $l = 86\,\mu$m downstream of the uncaging region. The flow velocity was $\bar{u} = 43\,\mu$m/s, so the corresponding

Péclet numbers were $Pe_a = 4.2$ and $Pe = 14$. In this case, $Pe_a^2/Pe = 1.3 \ll 4\pi^2$, satisfies the Taylor condition (6.39). Consequently, in figure 6.5(a), we see excellent agreement between the experimental results and the Taylor-Aris prediction. The rise in fluorescence intensity, which reflects the concentration of uncaged material, is shown as blue points. The red line displays the theoretical prediction according to Taylor and Aris.

The second measurement set was taken at $l = 25\,\mu$m with flow velocity $\bar{u} = 104\,\mu$m/s. The corresponding Péclet numbers were $Pe_a = 10$ and $Pe = 9.8$. In this case, the ratio $Pe_a^2/Pe = 11$ only weakly satisfies the Taylor condition (6.39). The switching event for this choice of parameters is displayed in figure 6.5(b). A clear discrepancy between the prediction and the experimental result is observed. To further investigate the accuracy of Taylor-Aris theory, we have performed numerical simulations of the photolysis induced switching events using the finite element method (FEM).

Numerical simulations: We solved the convection-diffusion equation in two dimensions (x, z) for the photo-uncaging geometry used in our experiments. The solid blue lines in figures 6.5(a) and 6.5(b) display the numerical results. They correspond to the values of Pe and Pe_a that describe the experiments. In both cases, the agreement between the FEM solution and experiment is excellent.

We extended these simulations and obtained a systematic set of data to characterize deviations from Taylor-Aris theory as a function of the Péclet numbers Pe and Pe_a. In figure 6.6, we summarize the results in terms of the relative switching time: the ratio of the switching time, taken on the bottom boundary of the FEM solution, and the switching time predicted by the one dimensional Taylor-Aris theory. For the two experimental cases discussed above Taylor-Aris

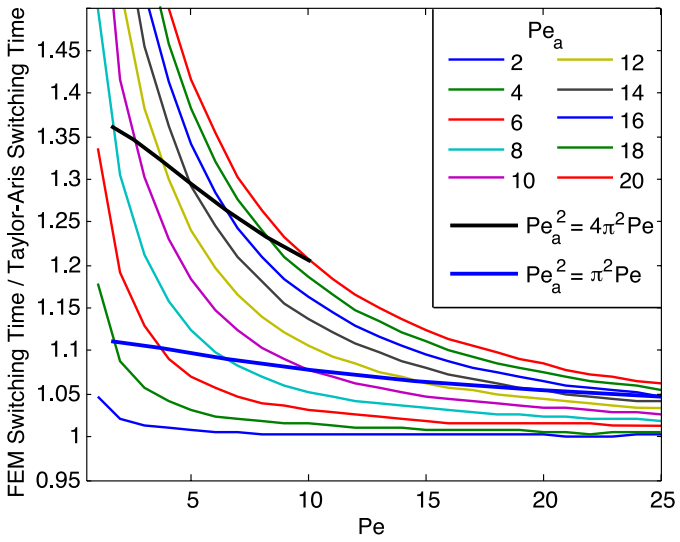

Figure 6.6: Comparison of switching times obtained from finite element simulations and Taylor-Aris theory. Relative switching times are shown as a function of Pe for different values of Pe_a. The bold lines correspond to a constant ratio of $Pe_a^2 = 4\pi^2 Pe$ (black) and $\pi^2 Pe$ (blue).

theory underestimates the switching time by 1% in the first ($Pe_a = 4.2$, $Pe = 14$) and by 8% in the second case ($Pe_a = 10$, $Pe = 9.8$). In addition, two examples of constant ratio Pe_a^2/Pe are displayed by the bold black and blue lines. They correspond to $Pe_a^2 = 4\pi^2 Pe$ and $Pe_a^2 = \pi^2 Pe$. It can be seen that the Taylor-Aris theory remains accurate within about 10% by choosing $Pe_a^2 = \pi^2 Pe$.

Even in cases where the switching times predicted by Taylor-Aris theory are not particularly accurate, they still provide a useful lower bound—in figure 6.6, all the curves remain above unity. This can be understood by a simple consideration: the Taylor-Aris approximation assumes that vertical diffusion removes the dependence of the concentration on the z coordinate. If this approximation is not fulfilled, the concentration profile reflects the parabolic flow profile. Compared to the Taylor-Aris limit, the concentration front now advances faster in the center and slower at the top and bottom walls of the channel, where the cells are placed for stimulation.

Table 6.1: The wall shear stress τ and theoretical switching time t_{switch} for representative parameters a, l, $\bar{u}$, and D corresponding to (1) the flow photolysis method, (2a)-(3a) valve mediated switching [86, 79], and (4a) interface sweeping [109]. Examples (2b)-(4b) compare the performance of these devices when we match the diffusivity and shear stress to example (1).

Example	a (μm)	l (μm)	$\bar{u}$ (μm/s)	D (μm^2/s)	τ (mPa)	t_{switch} (s)
1	26	25	104	267	24	0.4
2a	100	1.8×10^3	370	425	22	3.5
3a	25	250	200	425	48	0.7
4a	50	10^3	3×10^4	270	3.6×10^3	0.1
2b	100	1.8×10^3	400	267	24	4.2
3b	25	250	100	267	24	1.4
4b	50	10^3	200	267	24	2.3

6.4 Extension of theory to other methods

The more traditional microfluidics based methods for applying a temporally varying chemical signal rely on one of two principles: (i) *Valve-mediated switching*—a valve system is used to switch between flows of different concentration [86]. (ii) *Interface shifting*—an interface is formed between two adjacent streams of fluid with differing chemical concentrations. By changing the relative flow speeds at the fluid inlets, the interface between regions of different concentration can be swept across a cell, changing the cell's chemical surroundings [198, 108, 104]. In this section, we extend the theory to these techniques, and compare the performance of each. Examples are given in table 6.1.

Valve-mediated switching: Let us first consider microfluidic systems, where the chemical agent is introduced by opening a valve. Similar to the flow photolysis setup, the dynamics of the solute is described by (6.44). Here, $x = 0$ is the location of the valve that introduces the agent. Since there is no uncaging light, we set $I = 0$. Rather, we have an initial condition $c(x, 0) = c_0 H(-x)$, where H is the Heaviside function. Again, expressing x and t in units of η_K and τ_K, we

obtain the solution

$$c(x,t) = \frac{1}{2}\text{erfc}\left(\frac{x-t}{2\sqrt{t}}\right). \tag{6.62}$$

The resulting dependence of the switching time on l is displayed in figure 6.4 by the green dotted line. The rise time for the valve-mediated system is always longer than for the photolysis device operating in the saturating regime.

A microfluidic system that implements rapid switching of concentration gradients using valves was developed by Irimia et al. [86]: Their channel is $100\ \mu m$ tall with an average flow speed $\bar{u} = 370\ \mu m/s$. They characterized their device with fuorescein, $D = 425\ \mu m^2/s$ [39]. Their observation window was a distance $l \approx 1750\ \mu m$ away from the valves.

With these values, we calculate that $Pe_a = 87$ and $Pe = 1524$. The Taylor condition is satisfied, as $Pe_a^2/Pe = 5.0$. The effective diffusion coefficient

$$K = D\left(1 + \frac{Pe_a^{\,2}}{210}\right) = 1.57 \times 10^4 \mu m^2/s. \tag{6.63}$$

We can write the distance as $l = 42.5\eta_K$. From figure 6.4, we see that the switching time

$$t = 31\tau_K = 3.5\ s, \tag{6.64}$$

which is in excellent agreement with the experimentally observed switching time of approximately 4 s.

Interface sweeping: The second major class of microfluidic switching devices employs pressure induced changes in flow speed to shift the interface between regions of different concentration. As the prototypical design of such a device, a Y-junction can be considered. Via the Y-junction, two fluids of different concentration are injected into the rectangular main channel. An interface forms between the two fluids. The location of this interface in the channel depends directly on the ratio of the injection flow rates. If a cell is placed in the center of the

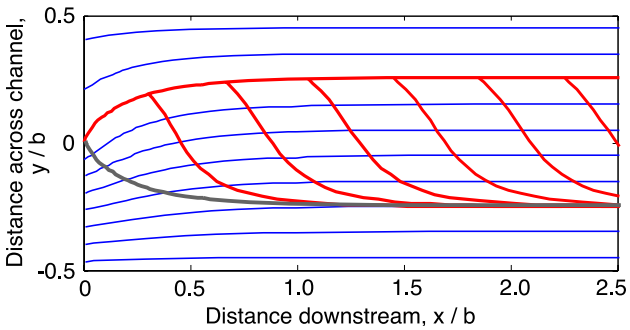

Figure 6.7: Interface sweeping. The initial interface is shown as a solid gray line and results from a ratio of inlet flow rates of $q_1/q_2 = 3$. The blue lines show the streamlines after switching of the inlet flow rates to a ratio of $q_1/q_2 = 1/3$. The red lines display the interface evolution following the switch in the ratio of inlet flow rates at evenly spaced points in time ($\Delta t = b/2v$).

channel, we may sweep the interface across the cell by adjusting the flow rates and thus expose the cell to a switching of ambient chemical concentrations.

What are the short time limits of switching that can be reached in such devices? Kuczenski et al. have experimentally characterized laminar interface shifting in a microfluidic setup, using ink and water to visualize the interface [108]. They obtained switching times of less than 0.1 s, which was their measurement resolution. These extremely quick events were achieved by using an average flow velocity of $\bar{u} \approx 2 \times 10^5$ μm/s—three orders of magnitude higher than the flow velocities that we used in the experiments presented in § 6.3.4. We must note that, for most live cell experiments the flow induced wall shear stress imposes upper limits on the flow velocities that we can use. Detailed studies of shear induced cell detachment have been performed, e.g., for the social amoeba *Dictyostelium discoideum*, a strongly adherent chemotactic microorganism. It was found that half of a population of adherent *Dictyostelium* cells are washed away at a shear stress of $\tau_{1/2} = 2.4$ Pa [43]. The shear stress in the experiments by Kuczenski et al. was $\tau \approx 30$ Pa, i.e., ten times higher than the critical detachment value reported in [43]. Furthermore, it has been

shown that at shear stresses around 1 Pa, living cells may exhibit mechanotactic responses [40, 69, 113]. Therefore, flow speeds in the range that was used in [108] are not suitable for many live cell experiments. In a recent publication, [109], Kuckzenski et al. have applied their approach to fibroblast stimulation experiments using strongly reduced flow speeds.

Let us consider the limits of fast concentration changes that can be achieved in such devices using the framework of Taylor-Aris theory. Ideally, the inlet pressures that drive the flow and determine the position of the interface can be adjusted immediately. Upon a change in the ratio of inlet pressures, the velocity field changes instantaneously, compared to the time it takes for the material to be convectively displaced. This is shown in figure 6.7. The solid gray line shows the interface that forms when the ratio of flow rates between the top and bottom inlets of the channel is $q_1/q_2 = 3$. If this ratio is changed to $q_1/q_2 = 1/3$, a new velocity field emerges, the streamlines of which are illustrated as blue curves. In figure 6.7, the resulting time evolution of the interface is shown by red lines that are evenly spaced in time. We note that the interface is shifting to its new position in the form of an oblique traveling wave. The wavefront propagates with the average downstream flow velocity, and as it moves, it undergoes dispersion. Therefore, Taylor-Aris theory can be applied to estimate the switching times at various positions in the channel. In particular, in cases where one of the input flow rates is switched to zero, the method of interface shifting becomes identical to valve-based switching. Thus, the same general limits apply for the switching time that were discussed for valve-based switching. Consequently, also in this case, flow photolysis provides the fastest switching events.

6.5 Application to flattening device

In this section, we analyze the switching time for a 14 μm tall single layer chamber, through which the flow rate required for collapsing the ceiling was found to be 250 μL/hr [193].[9]

Typically, flattened cells are around 3 μm tall, so in the height of the flattening chamber will droop from 14 μm at the borders, down to 3 μm in the center. We can model the height by assuming, to first approximation, that the ceiling is a surface of constant mean curvature H. Using the Monge representation for the ceiling height, i.e. $z = a(x, y)$, we get Poisson's equation:

$$\nabla^2 a = 2H. \tag{6.65}$$

We can solve this equation numerically using Jacobi's relaxation method [142]. Setting $a = 14\,\mu$m on the boundaries, and choosing $H = 0.125\,\text{cm}^{-1}$, we end up with the height profile shown in figure 6.8a. See Appendix C for details.

The fluid in this chamber is governed by the Stokes equation:

$$\nabla^2 \vec{u} = \frac{1}{\mu} \nabla P. \tag{6.66}$$

The vertical dimensions in our problem are much smaller than any of the lateral dimensions. Consquently, the $\partial^2/\partial z^2$ term dominates the left hand side. The right hand side has virtually no dependence on z. Integrating both sides of the Stokes equation, and using the no-slip boundary conditions to set the constants

[9] The attentive reader will recall that the chambers used in the response time experiments of chapter 5 were 5 μm tall. The choice to analyze the 14 μm tall chamber is threefold. Firstly, the chamber heights and flow rates needed to collapse the ceiling were carefully characterized for the taller chamber [193, 194]. The analysis in the section adds nicely to this body of work. Secondly, the flow speeds involved in collapse the ceiling for the taller device is much higher. This means that the Taylor condition 6.38 is more likely to fail for this geometry. Since it does not, the Taylor-Aris theory holds for the shorter device. Third, it is nice to leave to the reader an exercise: to show that in the 5 μm tall chambers, a the flow rate of 3 μL/hr translates into a switching time of 1.4 s.

of integration, we get

$$\vec{u} = \frac{\nabla P}{2\mu} z(z-a). \tag{6.67}$$

Next, let's calculate the height averaged velocity:

$$\vec{\mathfrak{u}} \equiv \frac{1}{a}\int_0^a \vec{u} dz = -\frac{\nabla P}{12\mu} a^2 \tag{6.68}$$

We also need the continuity equation, which in two dimensions looks like

$$\frac{\partial \rho_2}{\partial t} + \nabla \cdot (\rho_2 \vec{\mathfrak{u}}) = 0, \tag{6.69}$$

where ρ_2 represents the two-dimensional fluid density. The flow is incompressible, so in three dimensions, we would set the density to be constant. In the two-dimensional case, ρ_2 is constant in time, but not in space: the amount of material at a given location is proportional to the height a of the chamber. Thus, the continuity equation reads

$$\nabla \cdot (a\vec{\mathfrak{u}}) = 0. \tag{6.70}$$

Finally, plugging (6.68) into this equation yields

$$\nabla^2 P + 3\left(\frac{\nabla a}{a}\right) \cdot \nabla P = 0. \tag{6.71}$$

When the height is constant, this expression reduces to the Laplace equation. This case is the well known Hele-Shaw flow [78].

As before, this equation for pressure can be solved numerically using the relaxation method. We simply plug in the height information we calculated earlier, and use mixed boundary conditions: Dirichlet boundary conditions for pressure on the inlet and outlet of the geometry, and the Neumann boundary condition, $\partial P/\partial n = 0$ on the walls (appendix C). Once we have the pressure field, we can compute the velocities using (6.68). See in figure 6.8.

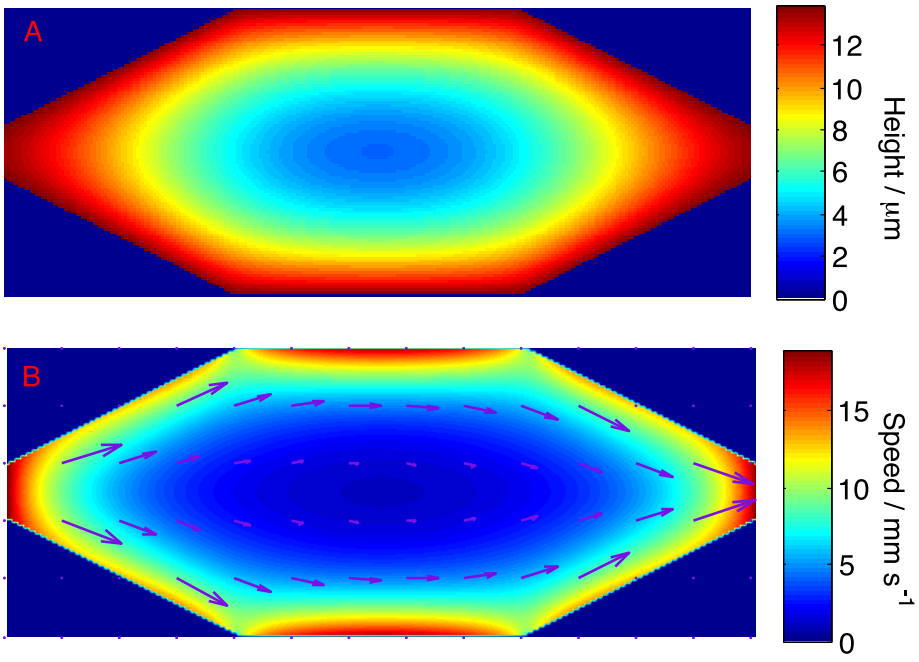

Figure 6.8: (a) The computed height and (b) The computed flow profile in the microfluidic flattening device.

We find that the flow rate of $250\,\mu$L/hr translates into a flow speed of 1.1 mm/s in the center of the flattening device. This number increases as we move away from the center. If we remain in a section of the device which is lower than 5 μm, the maximum flow speeds approach 2.5 mm/s. We choose a characteristic length $l = 25\,\mu$m, height $a = 5\,\mu$m, and speed $\overline{u} = 2000\,\mu$m/s. Using the diffusion coefficient of cAMP, $D = 444\,\mu\text{m}^2/\text{s}$ [51], we get the Péclet numbers $Pe = 113$ and $Pe_a = 22.5$. Although these numbers are quite large, the Taylor condition is satisfyed, as $Pe_a^2/Pe = 0.1 \ll 4\pi^2$. The Taylor-Aris dispersion coefficient is $K = 1520\,\mu\text{m}^2/s$. We enter the numbers into the linear uncaging model, along with $L = 93\,\mu$m, to find a switching time of 0.056 s in the $14\,\mu$m tall devices.

The devices used in chapter 5 were shorter, $a_0 = 5\,\mu$m, and used a lower flow rate of $3\,\mu$L/hr. With these parameters, the switching time is 1.4 s. Clearly, no reasonable amount of variability in this switching time can account for the large variation in the response time of the cells in chapter 5. Therefore the experimental variability must be either due to internal fluctuations, or to the individuality of the cells in the population. We will further discuss these possibilities in chapter 9: Summary and Outlook.

CHAPTER 7

ON THE SWIMMING OF *D. DISCOIDEUM*

In a classic lecture [143], E.M. Purcell familiarized us with the counterintuitive low Reynolds number world occupied by microorganisms.[1] At these low Reynolds numbers, inertia can be neglected, and the equation describing fluid flow loses any explicit time dependence. A consequence is Purcell's scallop theorem: a swimmer that performs reciprocal motion will end up where it started. Therefore, in order to propel itself forward, a micro-swimmer must undergo a sequence of shape changes which is asymmetric under time reversal. This swimming motion typically consists of the movement of appendages – rotation of helical flagella in bacteria like *E. coli*, and whiplike motion in flagella or coordinated, wave propogation in cilia of eukaryotes. In some species of *Euglena*, however, it has been conjectured that the cells can swim by changing the shape of their body in a process called metaboly [8, 70, 60].

Recently, N. P. Barry and M. S. Bretscher showed that *D. discoideum* amoebae and neutrophils, floating in a dense polysaccharide (Ficoll) solution, are capable of swimming towards a source of chemoattractant with speeds that rival those of crawling [13]. These cells lack flagella and cilia, so the authors suggested two mechanisms for how the cells may propel themselves forward: (i) There might be flow of plasma membrane from the front to the back of the cell (see §4.3). As the membrane is dragged backwards, it encounters a forward-pushing skin friction. (ii) Cellular protrusions, e.g. pseudopodia, moving from front to back act as paddles, propelling the cell forward. Although for us humans, crawling

[1] E.M. Purcell [143] and G.I. Taylor [171] are usually credited for developing the theory of low Reynolds number swimming. H.C. Berg [16] points out that this credit actually belongs to W. Ludwig, whose work predates Taylor's by some 20 years [115].

* This chapter consists of work published in Ref. [11]: A. J. Bae and E. Bodenschatz, *Proc. Natl. Acad. Sci.* **107**:E165-6.

and swimming are fundementally different, Barry and Bretscher postulate that the mechanisms used in swimming are likely to be the same ones active during crawling – it is unlikely that amoeba have developed two separate programs for locomotion.

We can test this postulate: If we could acquire the shape of a cell as it crawls on a substrate, then we could input these shape changes into a low Reynolds number fluid dynamics simulation to calculate a virtual swimming velocity. By doing so, we would answer the following question: if a cell executes the same motions to swim as it does for crawling, will it go anywhere?

7.1 Materials and methods

Ideally, we would have liked to obtain the three-dimensional geometry of cells as they crawl, but this would involve taking images at several different heights (z-stack), necessitating a lower frame rate. As it is crucial to use a frame rate high enough to capture details such as pseudopod formation, we opted instead to examine cells crawling in a microfluidic flatland.

D. discoideum (cytosolic GFP in AX2) cells were developed in shaking culture (§2.1) and loaded into the lower layer of a flattening device (closed-end actuator, §2.2). A 5 μL/hr flow of phosphate buffer was applied to supply the cells with oxygen and to wash away any waste products generated by the cells. Pressure was applied to the top layer to flatten the cells down to $\sim$4 μm. These flattened cells were imaged every second at a resolution of 0.2 μm/pixel using an inverted confocal laser scanning microscope (FV1000 Olympus). This frame rate is sufficiently high for capturing pseudopod formation (see figure 7.1b).

The images were thresholded to separate the region corresponding to the cell from the background. Then, the Active Contour Toolbox was used to extract

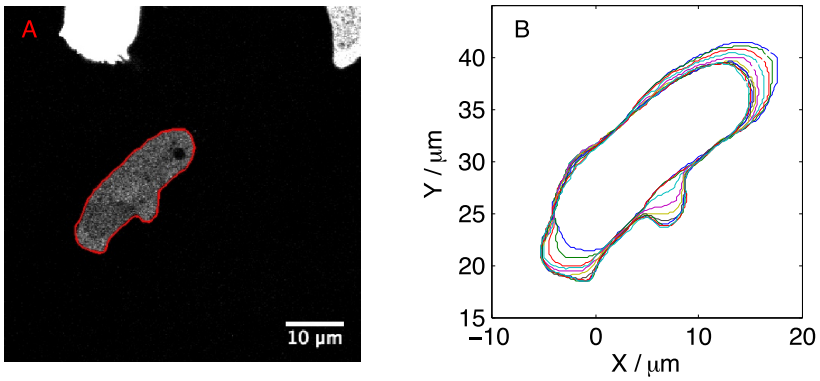

Figure 7.1: Contour of a typical cell. (a) The cell contour (in red) is overlaid on the original confocal image. (b) The evolution of the cell contour over a 10 s interval shows the formation of the lateral psuedopod. Note that the frame rate ($f_{image} = 1/s$) was sufficient to capture this process.

the cell boundary [42]. An example of a cell boundary, overlayed on the original confocal image is shown in figure 7.1a.

Once the cell boundaries were retrieved, A. Shapere and F. Wilczek's framework for analyzing low Reynolds number propulsion was applied [159]. The first step in this analysis was to choose a "standard location" for each shape $S_0(t)$, i.e. to assign the shape an origin with axes. We chose this origin to coincide with the centroid, and we chose axes parallel to original image axes.

Next, we created an evenly spaced, 250 point parameterization of the shape, $S_0(\sigma, t) = [x(\sigma, t), y(\sigma, t), 1]^T$, $\sigma = 1, 2, ..., 250$. At each time step, this parameterization was chosen to minimize the total distance

$$\rho(t)^2 \equiv \sum_{\sigma} [x(\sigma, t) - x(\sigma, t - \Delta t)]^2 + [y(\sigma, t) - y(\sigma, t - \Delta t)]^2, \tag{7.1}$$

or equivalently, to maximize the cross-correlation

$$c(t) \equiv \sum_{\sigma} x(\sigma, t)x(\sigma, t - \Delta t) + y(\sigma, t)y(\sigma, t - \Delta t). \tag{7.2}$$

Note that the use of this parameterization precluded any net membrane flow from our simulation.

Now, any rotation, R, of S_0, followed by a translation, $\vec{d}$, can be represented with a 3×3 matrix $\mathfrak{R}$:

$$\mathfrak{R}S_0(\sigma) = \begin{bmatrix} R & \vec{d} \\ 0 & 1 \end{bmatrix} \begin{bmatrix} \vec{r}(\sigma) \\ 1 \end{bmatrix} = \begin{bmatrix} R\,\vec{r}(\sigma) + \vec{d} \\ 1 \end{bmatrix}. \tag{7.3}$$

If we denote the position of the swimmer by $S(t)$, then the problem reduces down to finding the $\mathfrak{R}(t)$ that rotates and translates the standard shape into the proper location:

$$S(t) = \mathfrak{R}(t)S_0(t). \tag{7.4}$$

If a swimmer, starting at $S_0(t - \delta t)$, ends up at $\Delta\mathfrak{R}(t)S_0(t)$ after a time δt, then a swimmer starting at $S(t - \delta t) = \mathfrak{R}(t - \delta t)S_0(t - \delta t)$ should end up at $S(t) = \mathfrak{R}(t - \delta t)\Delta\mathfrak{R}(t)S_0(t)$. Therefore, it follows that

$$\mathfrak{R}(t) = \Delta\mathfrak{R}(\delta t)\Delta\mathfrak{R}(2\delta t) \cdots \Delta\mathfrak{R}(t). \tag{7.5}$$

For infinitesimal dt,

$$d\mathfrak{R}(t) = \mathfrak{R}(t - dt)\left(\Delta\mathfrak{R}(t) - \mathbb{I}\right) \tag{7.6}$$

$$= \mathfrak{R}(t)A(t)dt. \tag{7.7}$$

Here $A(t) = (\Delta\mathfrak{R}(t) - \mathbb{I})/dt$. Let's look explicitly at the matrix elements:

$$A(t) = \frac{1}{dt}\begin{bmatrix} \cos(d\theta) - 1 & \sin(d\theta) & dx \\ -\sin(d\theta) & \cos(d\theta) - 1 & dy \\ 0 & 0 & 1 - 1 \end{bmatrix} \tag{7.8}$$

$$= \begin{bmatrix} 0 & \omega & v_x \\ -\omega & 0 & v_y \\ 0 & 0 & 0 \end{bmatrix}. \tag{7.9}$$

Note that x and y are in the reference frame of $S_0(t)$.

To recover $\mathfrak{R}(t)$ from $A(t)$, we use 7.5:

$$\mathfrak{R} = (\mathbb{I} + A(dt)dt)(\mathbb{I} + A(2dt)dt) \cdots (\mathbb{I} + A(t)dt) \tag{7.10}$$

$$= \mathbb{I} + \sum_{n_1}^{t/dt} A(n_1) + \sum_{n_1<n_2}^{t/dt} A(n_1)A(n_1) + ... \tag{7.11}$$

$$= \overline{\mathcal{P}} \left\{ \exp \left[\int_0^t A(t)dt \right] \right\}, \tag{7.12}$$

where $\overline{\mathcal{P}}$ represents inverse path ordering.

The cell cannot "pull itself by its bootstraps" – as the cell swims through the fluid, the net force and torque on the cell must be zero. This condition, along with the boundary condition at infinity, determines the rotation $\omega(t)dt$ and translation $\vec{v}(t)dt$ the cell undergoes as it changes shape from $S_0(t)$ to $S_0(t + dt)$.

The finite element method (COMSOL) was used to solve a trial flow $\vec{u}(\vec{r}, t)$ – the Stokes flow around an cell changing its shape from $S_0(t)$ to $S_0(t + \Delta t)$. See figure 7.2. The geometry $S_0(\sigma, t)$ was entered in a circular domain ($r_0 = 250\,\mu$m). The boundary, Γ, of this domain was an open, zero normal stress boundary. On the surface of the cell, the no-slip boundary condition was applied:

$$\vec{u}|_{\vec{r}=S_0(\sigma,t)} = \frac{\partial S(\sigma, t)}{\partial t} = \frac{S(\sigma, t + \Delta t) - S(\sigma, t)}{\Delta t}. \tag{7.13}$$

The open boundary condition on the outer wall ensured that the force and torque on the cell was negligible. On the other hand, the fluid velocity, far from the cell, was appreciable. From the fluid velocity at the outer boundary, we determined the $\vec{v}$ and ω necessary to remove this flow:[2]

$$\vec{v} = -\frac{1}{2\pi r_0} \oint_\Gamma \vec{u} ds \tag{7.14}$$

$$\omega = -\frac{1}{2\pi {r_0}^3} \oint_\Gamma (\vec{r} \times \vec{u}) \cdot d\vec{s} \tag{7.15}$$

[2]Equivalently, we may view this as a shift in reference frame, from one in which the swimmer's centroid is not moving, to one in which the fluid, far away is not moving on average.

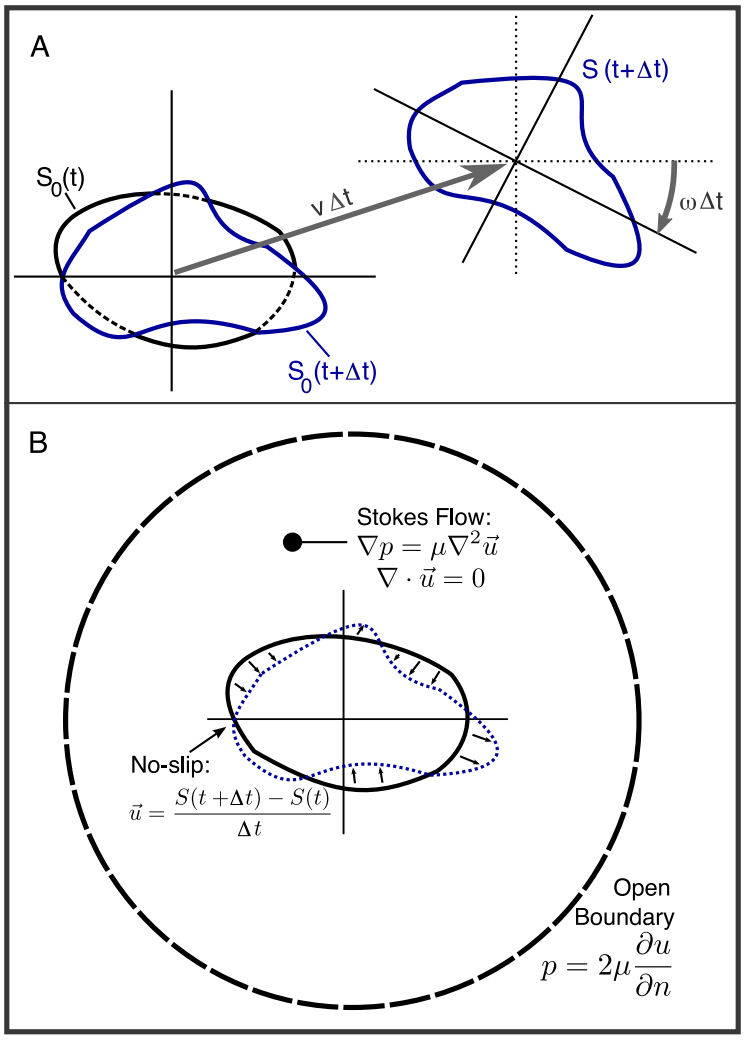

Figure 7.2: The virtual swimming simulation. (a) At each time step t, we would like to know how much the swimmer is displaced when its shape changes from $S_0(t)$ to $S_0(t+\Delta t)$. (b) We solve the Stokes flow on a $500\,\mu$m wide circular domain with an open outer boundary, and a no-slip boundary where the cell is situated. Figures not drawn to scale.

The velocity was divided into a component along the direction of the cell's polarization $\vec{v}_{\parallel}$, and a component perpendicular $\vec{v}_{\perp}$. The polarization was defined as the direction from the cell's back to its centroid. The cell's back was defined from the space-time plots of curvature $\kappa(\sigma, t)$ for $S(\sigma, t)$ See figure 7.4. These space-time plots show regions of high curvature (pseudopodia) moving

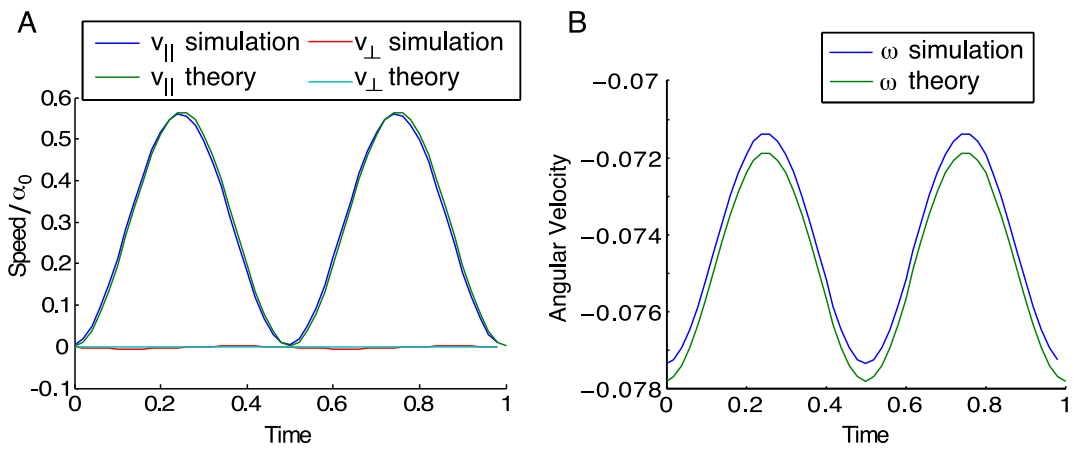

Figure 7.3: Comparison between simulation and the theoretical solution for the (a) translation velocity and (b) angular velocity of Shapere and Wilczek's example swimmer.

from the front to the back of the cell, where they are absorbed into a region of persistently high curvature. We defined the back as the local maximum in this region.

To verify the accuracy of the finite element method, Shapere and Wilczek's two dimensional swimmer,

$$S(\sigma, t) = \alpha_0\sigma + \alpha_{-2}\sigma^{-1} + \alpha_{-3}\sigma^{-2}, \tag{7.16}$$

$$\alpha_0(t) = 10\,\mu\text{m}, \tag{7.17}$$

$$\alpha_{-2}(t) = \alpha_0[0.3\cos(2\pi t) + i0.015\sin(2\pi t)], \tag{7.18}$$

$$\alpha_{-2}(t) = \alpha_0[-0.3\sin(2\pi t) + i0.015\sin(2\pi t)], \tag{7.19}$$

was entered into the simulation. The comparison with between simulation and theory is shown in figure 7.3. Note the excellent agreement.

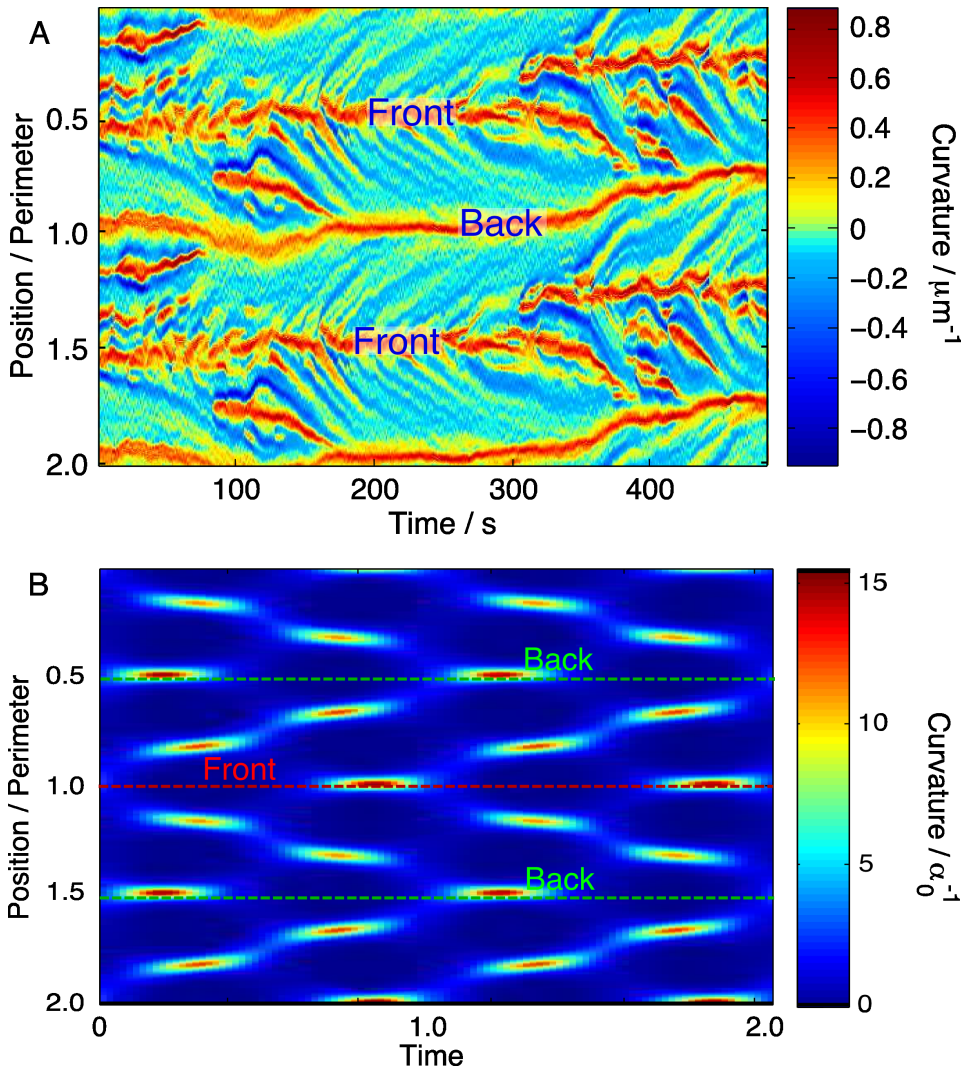

Figure 7.4: Curvature space-time plots for the contours of (a) a typical crawling cell and (b) the Shapere-Wilczek swimmer. To prevent a loss of detail at the edges, the curvature has been plotted over two contour lengths. Note the herringbone structure—regions of high curvature bifurcate at the front and travel towards the back.

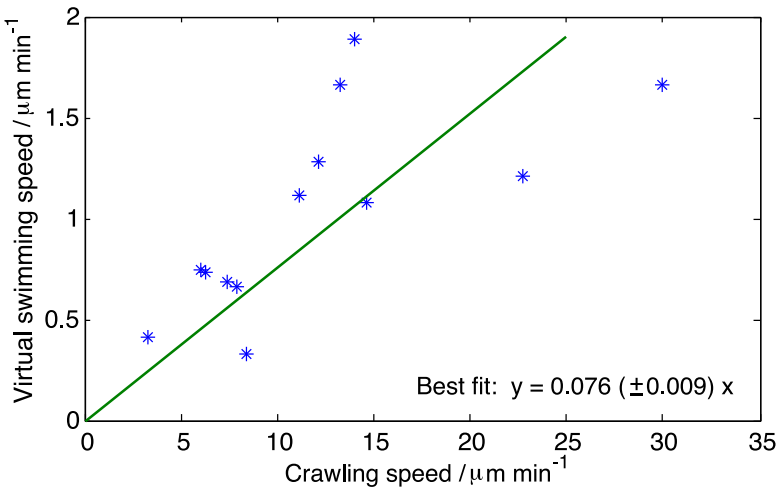

Figure 7.5: The crawling and virtual swimming velocities along the direction of polarization. Constrained least squares regression shows that the cells crawl 12 times faster than they swim.

7.2 Results

We analyzed the virtual swimming velocity of $n = 13$ cells, and found that, for all cells, the time-averaged component along the direction of polarization was positive. The average directed swimming speed was 1.0($\pm$0.5) μm/min. The crawling speed was found to be 12($\pm$7) μm/min. The correlation coefficient $r = 0.6943$ with $p = 0.009$. Therefore, cells that crawl faster are also faster swimmers (figure 7.5).

In [13], the cells swim at 4.2 μm/min and crawl at 3.8 μm/min. Our measured crawling speed is 3 times higher, and our virtual swimming speed is 4 times lower. The difference in speeds can be attributed to the vertical confinement of our cells, as flattened cells migrate faster and have a lower rate of pseudopod production. There may also be a contribution to swimming from a membrane flow, which has not been included here.

CHAPTER 8

SORTING OF *D. DISCOIDEUM* IN TWO DIMENSIONS

As the chemotactic stage proceeds, the cells come into end-to-end contact, forming a loose aggregate. This loose aggregate is composed of several streams which converge at the aggregation center, figure 8.1. As time evolves, the streams wind around the center to form a hemispherical mound. In this mound, *D. discoideum* has differentiated into an 80:20 ratio of prespore to prestalk cells. These two populations are initially mixed in a salt-and-pepper distribution [131, 177]. Then, the prestalk cells sort out from the prespore cells to form an apical tip on the aggregate. How this organization occurs is still not completely understood, although there are two proposed mechanisms.

One theory is that cell sorting is driven by differential chemotaxis [187]. Prestalk cells were shown to have higher chemotactic velocities towards cAMP [53], and spiral waves of cAMP have been observed in mounds [48, 160]. Therefore, the faster prestalk cells should be expected to rush towards the signaling center, leaving the slower prespore cells in the periphery. Experiments supporting this viewpoint include observations that GFP-tagged prestalk cells move independently and directionally to form a cluster [37]. Furthermore, it has been shown, using temperature sensitive mutants, that adenylate cyclase A (ACA) activity is required for the formation of the apical tip [135]. Adenylate cyclase synthesizes cAMP, so this result indicates that cAMP signaling is necessary for cell sorting.

The other theory for cell sorting is the differential adhesion hypothesis [165, 90]. In this theory, the two cell types have five different contact energies, two for the interactions between cells and the surrounding medium, $J_{pst,0}$ and $J_{psp,0}$; two for interactions between like cells (cohesion), $J_{pst,pst}$ and $J_{psp,psp}$; and one between the cell types, $J_{pst,psp}$. Macroscopically, these in-

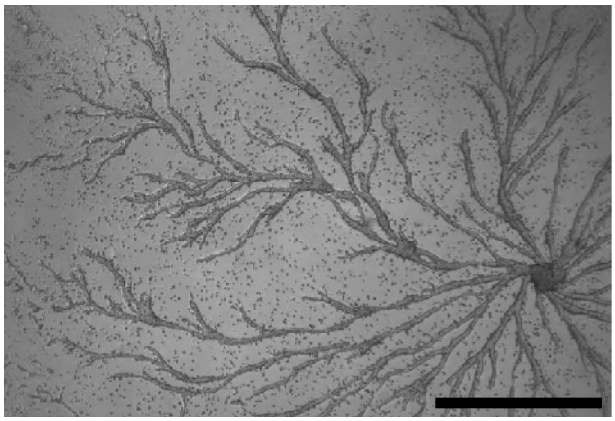

Figure 8.1: Loose aggregate of developing *D. discoideum* (AX-3) cells. Scale bar = 1 mm. This image was produced in collaboration with Duane Loh.

teractions can be written as three surface tensions: $\sigma_{pst} = J_{pst,0} - (J_{pst,pst}/2)$, $\sigma_{psp} = J_{psp,0} - (J_{psp,psp}/2)$, and $\sigma_{pst,psp} = J_{pst,psp} - (J_{pst,pst} + J_{psp,psp})/2$ [75, 82]. In this model, interactions occur locally, with cells exchanging one type of interface with another in an effort to minimize free energy, analogous to phase separation in mixtures of immiscible fluids.

Evidence supporting the differential adhesion hypothesis include experiments which show that the contact proteins LagC and LagD are essential for tip formation [52, 161, 101]. Observation of cells sorting in flattened mounds show that the cells rotate around the aggregate in a vortex state [148]. Over time, a group of a few prestalk cells slow down. As the remaining cells continue to vortex, prestalk cells pile up when they encounter this obstacle [131]. This cell sorting behavior suggests that the prestalk cells are adhering to the substrate and to each other more strongly than with the prespore cells. Finally, in contrast with the aforementioned experiments on temperature-sensitive ACA mutants, there are experiments which show that ACA null mutants that overexpress the downstream effector PKA (acaA/PKA) will develop into fruiting bodies, even though they do not produce detectable amounts of cAMP [188, 148].

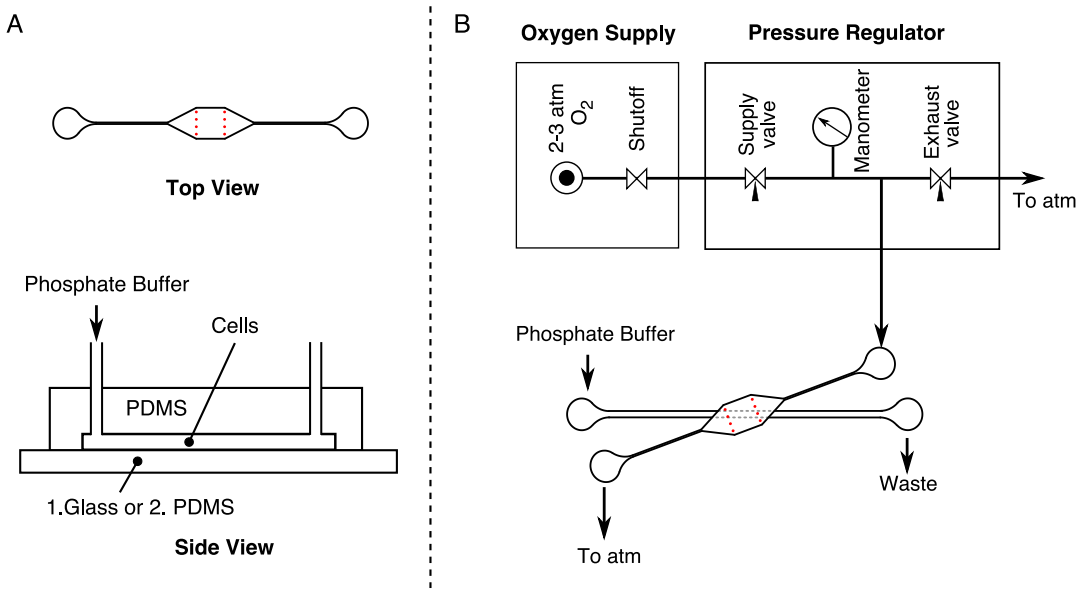

Figure 8.2: Microfluidic devices for investigating cell sorting: (a) Single-layer, wide aspect ratio chamber with a 1. glass or 2. PDMS floor. (b) Double-layer, through-flow actuator. Figure adapted from [194].

The question of how cells sort is open, and whether the mechanism is differential chemotaxis or differential adhesion or something else is unclear. Most likely, both chemotaxis and adhesion are important [99, 191]. If we could track individual prespore and prestalk cells, then we could quantitatively discern the long-range chemotaxis from short-range adhesive interactions. To make this goal more tractable we attempted to flatten mounds of prestalk-labeled cells down to a monolayer. This ensures that the cells remain in one focal plane. Cell sorting in a flattened mounds has been reported previously by A. Nicol et al. (1999), but these aggregates were always a few cell layers thick [131].

8.1 Materials and Methods

The cbpD::gfp strain of *D. discoideum* was a kind gift from William Loomis. The cbpD gene encodes a small calcium binding protein, and is expressed by prestalk cells, four hours into development [85]. The cells were developed in

shaken suspension as discussed in §2.1. These developed cbpD::gfp cells were loaded into one of three different microfluidic systems: (i) a 5 μm tall, single layer, wide aspect ratio channel with a 0.15 mm thick glass or (ii) $\sim$ 0.5 mm thick PDMS membrane bottom, or the cells were loaded into the lower layer of a (iii) double-layer, through-flow actuator. See figure 8.2. To rinse away waste products, a gentle flow of 0.5 μL/hr was applied in the wide aspect ratio channels, and 0.1 μL/hr in the straight channels. Note that in devices (ii) and (iii), oxygen could reach the cells by permeating through the thin PDMS membrane [150].

Once the cells aggregated to form a mound, images were taken on an inverted confocal scanning laser microscope (FV1000 Olympus), using a frame rate f_{image}= 0.5/min or 1/min.

8.2 Results

In the 5 μm tall glass-bottomed single-layer device, cells aggregated to form rotating mounds 1-2 layers thick. Cells in these mounds, however, did not differentiate and sort into prespore and prestalk regions. It has been previously observed that differentiation does not normally occur for *D. discoideum* in submerged conditions due to oxygen depletion [25, 166]. Could oxygen depletion be the reason why we don't see differentiation?

We replaced the glass bottom with an $\sim$ 0.5 mm thick PDMS membrane. Air should easily permeate through this thin membrane. As the bottom wall is no longer rigid, the mound that formed when cells aggregated was several layers thick. The cells in this aggregate differentiated and sorted in a manner consistent with the observations of Nicol et al. [131]:

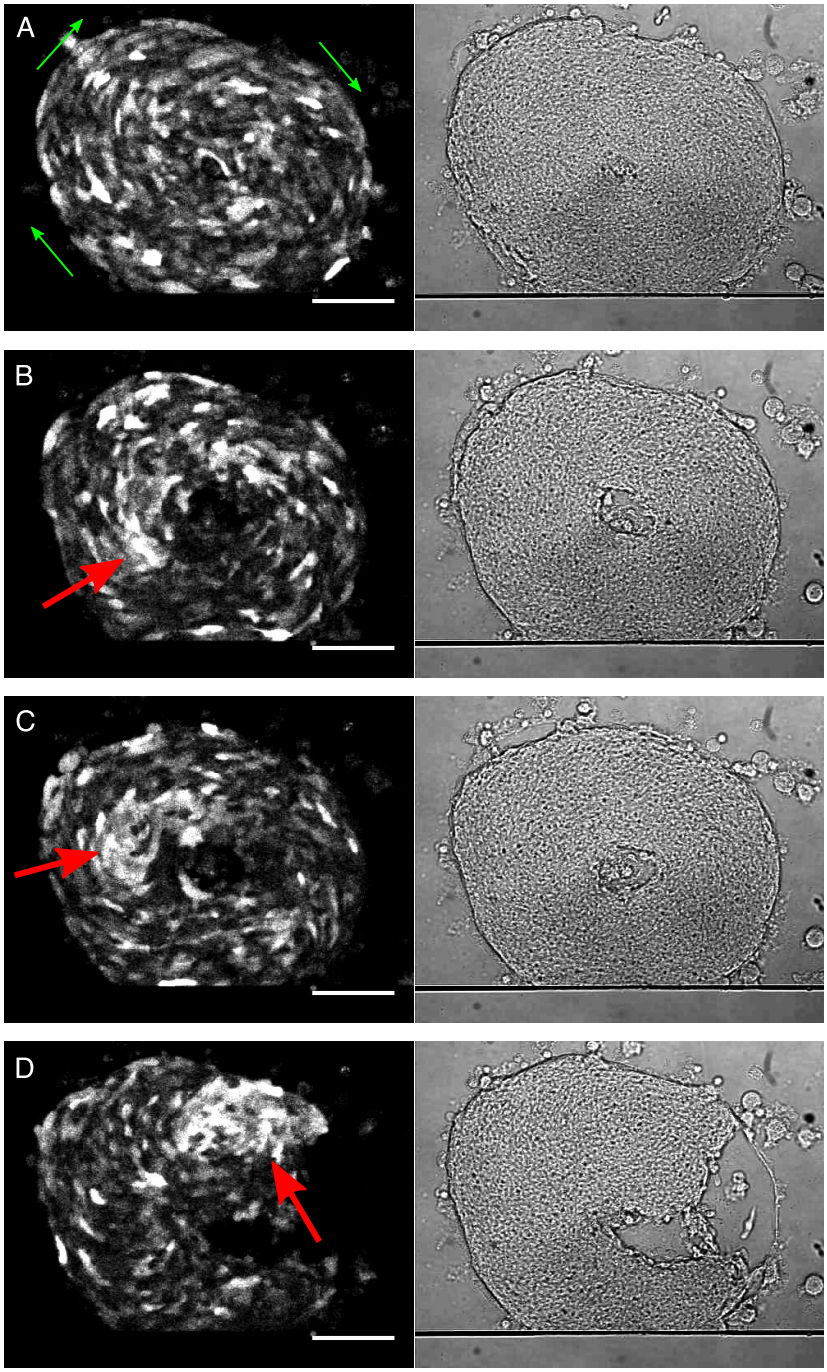

Figure 8.3: The sorting of cbpD::GFP cells in a PDMS-bottomed micro-channel. On the left are fluorescence images, in which bright cells are prestalk, and dark cells are prespore. On the right are the corresponding bright field images, taken at (a) 15.2 hrs, (b) 17.1 hrs, (c) 17.5 hrs, and (d) 18.1 hrs into development. In figure (a), arrows indicate direction of rotation. Arrows in figures (b)-(d) indicate region of aggregating prestalk cells. Scale bar=50 μm.

Initially prestalk and prespore cells were well mixed, rotating in a vortex (figure 8.3a). Over the next two hours, the aggregate took on a toroidal shape as the rotation speeded up. Around this time, a group of prestalk cells suddenly slowed down (figure 8.3b). Over the next half hour to hour, prestalk cells piled up in this region (figure 8.3c). Finally, the torroidal mound broke, and the group of prestalk cells moved to the front of a flattened slug (figure 8.3d).

Replacing the glass bottom of the single layer micro-channel with PDMS permitted the cells to differentiate and sort. Unfortunately, the aggregates were three dimensional, and it was difficult to track cells to accurately determine what each cell is actually doing. To address this issue, we developed the double-layer through-flow device, figure 8.2b. In this device, the aggregates were situated in the lower channel, where they were flattened between a glass cover slip below and a PDMS membrane above. Oxygen flowing in the channel above was used to apply the pressure to the PDMS membrane. Some of this gas should have permeated through the membrane, preventing the cells from becoming oxygen depleted.

In these double layer devices, the cells aggregated to form a mound, 1-2 cell layers thick. Differentiated prespore and prestalk cells were observed rotating in a vortex state (figure 8.4), but they did not sort into two separate populations.

This result indicates that cell sorting in *D. discoideum* could be a three dimensional process. This might be understood within the context of the differential adhesion hypothesis. M. S. Hutson et al., [82], recently reported that a high interfacial tension $\sigma_{pst,psp}$ may hinder the kinetics of cell sorting in two dimensions, but not in three dimensions. The reason is that in two dimensions, the connectivity of the minority population – the prestalk cells – is low, and in order to sort, the prestalk cells must find each other by making their way through

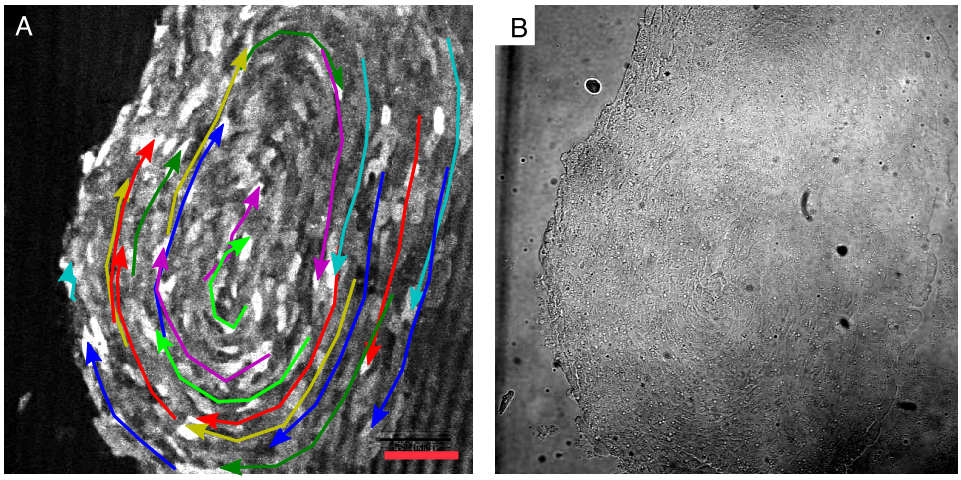

Figure 8.4: The (a) fluorescence and (b) brightfield images of a mound of cbpD::GFP cells flattened down to a layer, ca. 1-2 cells thick using the double layer through-flow actuator. Note that the low contrast in the bright field image is due to the flatness of the mound. Scale bar = 50 μm.

regions of prespore cells. This is prohibitively difficult when $\sigma_{pst,psp}$ is high. In three dimensions, the connectivity is much higher. In fact, Hutson et al. say that if the ratio of differentiated cells were 70:30, then more than 95% of the minority population would in contact with one another in a single domain – a structure which contains many loops and tunnels [82]. Therefore, the process for sorting in three-dimensions was proposed to be driven by instabilities, which separate the prestalk and prespore domains by pinching off the loops and tunnels, similar to how the Plateau-Rayleigh instability breaks thin lines of fluid into droplets.

In our cell sorting experiments we did not see any direct evidence for this instability driven sorting. Rather, the sorting appeared to be driven by prestalk cells piling up behind an obstacle, while the other cells continue to rotate in the mound. Yet, the idea that connectivity in three dimensions is vastly different from that in two dimensions may help us to understand how the prestalk cells find each other in the taller, multilayer aggregates.

CHAPTER 9

SUMMARY AND OUTLOOK

In chapter 3, we saw that, contrary to conventional wisdom, cell growth is not a solitary activity. Rather, growth is stimulated by interactions with neighbors, and these interactions are most likely based on cell-to-cell contact or short range paracrine signaling.

In chapter 5, we investigated the timing of the biochemical signals involved in direction sensing, and we attempted to alter this timing by flattening cells to various degrees, applying an external pulse of chemoattractant, and looking at the response time of various proteins that are involved in chemotaxis. We expected to see a relation between the response time and the degree of flattening, because as the cell's area increases, so should the time it takes for the messengers involved in chemotaxis to diffuse across the cell. Unfortunately, the variability in the response times prevented us from reaching a definitive conclusion. In chapter 6, we ruled out the possibility that this variability might be due to the experimental setup itself. Rather, the variability in response times may be intrinsic, or it may be due to variations between cells.

If further response time experiments are conducted, then they should be done on individual cells. First, we should investigate the reproducibility in the response of a single, unflattened cell to a pulse of chemoattractant (similar to the long period experiments in [195]). Then, repeating this individual cell response measurement for a few different cells should give us an indication of whether the variability in the experiments of chapter 5 was intrinsic to the cell, or if it was due to cell to cell variations. Provided that the results of these single cell measurements are reproducible, we should investigate the reproducibility in the response time for a cell, flattened to a fixed height, to ensure that the

applied mechanical stress doesn't cause the cell to misbehave. A double layer, closed-end actuation flattener should be used, due to the high degree of control it provides. Finally, we can proceed to make measurements on single cells undergoing various degrees of flattening, to see if there is a dependence of response time on the cell's area.

In chapter 7, we showed that swimming and crawling are likely to be driven by the same motility mechanisms. We took images of flattened cells, and showed that two-dimensional virtual swimmers, executing the same shape changes as the flattened cells, would also swim forward. However, our virtual swimmers move four time slower than the actual swimming amoebae in [13]. This leaves some open questions. Is the discrepancy due to the fact that we modeled two-dimensional swimmers? A two-dimensional swimmer might not be very physical – it would correspond to an object infinitely long in three dimensions. Or is the discrepancy due to a membrane flow that we did not account for in our computations?

We should be able to resolve these questions using confocal spinning disk microscopy to quickly obtain three-dimensional shape data from swimming cells. We would compute the virtual swimming speed of actual swimmers. If the speeds match, then there is no membrane flow. If the speeds do not match, then we could ask what type of membrane flow do we need to add to the simulations to make the swimming velocities agree? Finally, to complete the story, we would then take three-dimensional data on crawling cells, and compare the virtual swimming speeds of these cells with the speeds of the previously measured swimmers.

In chapter 8, we examined cell sorting in the mound stage. We confirmed the observations of [131], for cell sorting in flattened, multi-layer mounds. How-

ever, we were unable to observe cell sorting in mounds flattened down to 1-2 layers. This could indicate that cell sorting is a three-dimensional process [82]. To better examine the role of dimensionality, it may be fruitful to systematically investigate whether or not cell sorting takes place, and if so, how long it takes as a function of mound height.

Further insight into the role of adhesion may also be provided with tools like the AFM [15]. We could attach a prestalk cell to the cantilever, bring the cell in contact with another prestalk or prespore cell, then measure how much work needs to be done to pull the two apart. From this, we would get an idea of the adhesive energies involved. Then we can investigate how these energies change for lagC-null or lagD-null cells.

To probe the role of chemotaxis in cell sorting, it might be useful to observe the cAMP-based signaling in mounds using the highly sensitive monomeric cAMP FRET sensor cells developed by Bagorda et al. (2009), [12]. Also informative would be to transfect the acaA/PKA cells with cbpD::gfp, to observe how cells sort without cAMP-based signaling.

To conclude, let's discuss two fascinating topics for future research. In figure 9.1a, we see an example of a spinning cell, rotating at $\sim$3 rpm. The cell is under flattening in a double-layer, closed-end actuation microfluidic device. The bottom right side is in contact with a cluster of cells. The question is, what is causing the rotation? Is it a circulation in the micro-flow? Is it that the cells on the bottom right are exerting a torque on the cell? This rotational state is not a common occurrence. Therefore I implore you, the reader, if you see this rotational state in an experiment you're conducting, and you don't already know the answer to this riddle, then take some time out to figure out what is going on. If the cell is in a microfluidic device, try adjusting the flow rate to see if the

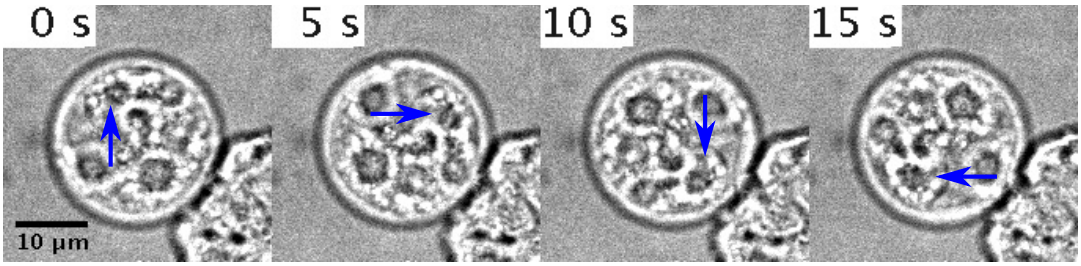

(a) A spinning cell. The blue arrow marks a feature as the cell rotates.

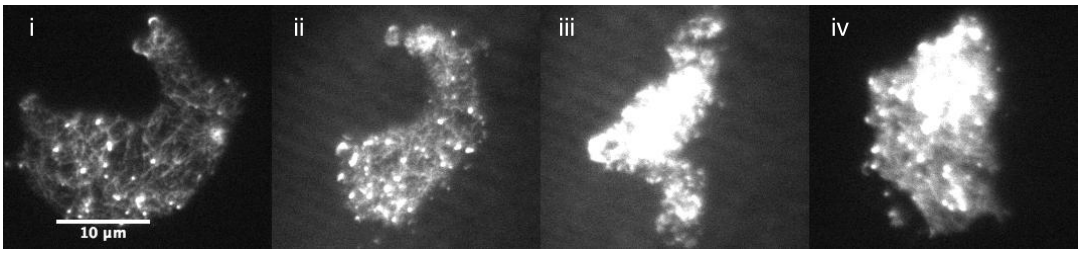

(b) Actin response to osmoshock. A LimE-GFP cell was observed in TIRF microscopy (i) 0.5 min before, (ii) 1.0 min into, (iii) 3.0 min into, and (iv) 3.0 min after a 400 mOsM shock.

Figure 9.1: Topics for future investigations

rotational speed changes. Check to see if the cell has neighboring cells. There just might be something really interesting happening.

The other topic of inquiry is osmoregulation in the cell. How does a *Dictyostelium* cell respond to osmotic shock? In figure 9.1b, we see the response of LimE:GFP, a marker for filamentous actin, observed with TIRF microscopy, in response to a 400 mOsM shock. We see that the activity in actin polymerization skyrockets when the shock is applied – it is as if the cell is mobilizing the cytoskeleton to prevent itself from collapsing inward. Also, when cells are treated with latrunculin A to dissolve the actin cytoskeleton, the volume of the cells decreases.[1] These observations indicate that actin plays an important role in osmoregulation – one which should be better investigated.

[1]Two 20 ml shaking cultures, grown to $\sim 10^7$ cells/ml were centrifuged. The supernatent was removed. The two pellets were consolidated in 20 mL of phosphate buffer, and mixed. This suspension was split into two tubes, a control, and one containing 10 μM latrunculin A (latA). The cells were treated for 5-10 min, then centrifuged. The latA pellet was $\sim 18\%$ smaller than the control.

APPENDIX A

CALCULATING FLOW PROFILE AND SHEAR STRESS IN A RECTANGULAR CHANNEL

```
% -------------------- flowprofile.m ---------------------------%
%                                                               %
% This matlab script calculates the flow profile and bottom     %
% wall shear stress inside a rectangular cross-section channel. %
%                                                               %
% ---------------------------------------------------------------%

ubar = 104e-6;      % Speed (m/s)
a =     26e-6;      % Channel height (m)
b =    500e-6;      % Channel width  (m)
visc = 1.0e-3       % Dynamic viscosity of water (Pa*s)
sumterms = 40;      % Number of entries to sum over in m and n

gam = b/a;          % Aspect ratio

[M,N] = meshgrid(0:sumterms,0:sumterms);
clear sumterms;

% First, let's get the average flow velocity normalization
ubar2=4/(ubar*pi^2)*sum(sum((1).^M./...
        ((2*M+1).^2.*(2*N+1).^2.*((2*M+1).^2+...
        gam*gam*(2*N+1).^2))));

% Next, we calculate the flow in the middle of the channel
i=1;
z=0;
for y=-0.5:0.01:0.5  % in units of channel width
    u(i)=sum(sum((-1).^M.*(-1).^N.*cos(pi*(2*M+1)*y).*...
         cos(pi*(2*N+1)*z)./((2*M+1).*(2*N+1).*((2*M+1).^2+...
         gam*gam*(2*N+1).^2))));
    i=i+1;
end
u=u/ubar2;  % Normalize u to get the correct mean velocity

% Display the flow speed
y=-0.5:0.01:0.5;
plot(y,u); % Plot it
xlabel('y / b');
ylabel('Flow speed u / (m/s)');

% Next, we calculate the shear at the bottom of the channel
i=1;
z=0;
for y=-0.5:0.01:0.5
    stress(i)=(pi/a)*sum(sum((-1).^M.*cos(pi*(2*M+1)*y)./...
```

```
                ((2*M+1).*((2*M+1).^2+gam*gam*(2*N+1).^2))));
    i=i+1;
end
stress=visc*stress/ubar2;

% Display the shear
figure
y=-0.5:0.01:0.5;
plot(y,stress);
xlabel('y / b');
ylabel('Wall shear stress \tau / Pa');
```

APPENDIX B

CALCULATING TAYLOR-ARIS SWITCHING TIMES

```
% ------------------- switchTimeExample.m ------------------- %
%                                                             %
% This Matlab script demonstrates how to calculate the Taylor %
% Aris switching time for valve based systems, linear regime  %
% and saturating regime flow photolysis systems.              %
%                                                             %
% Note that all lengths are in units of eta_K = K/u, and all  %
% times are in units of tau_K = K/u^2                         %
% ----------------------------------------------------------- %


l = 30;  % The distance from the cell to the uncaging light
L = 20;  % The length of the uncaging region

% First example is the valve based switching
t1 = fzero(@(t) (valveSwitchC(l,t)-0.05),l);
t2 = fzero(@(t) (valveSwitchC(l,t)-0.95),l);
swT1=t2-t1

% The next example is the linear regime photolysis
t1 = fzero(@(t) (LowIntensityC(L,l,t)-0.05),L,l);
t2 = fzero(@(t) (LowIntensityC(L,l,t)-0.95),L,l);
swT2=t2-t1

% The last example is the saturating regime photolysis
t1 = fzero(@(t) (HighIntensityC(l,t)-0.05),l);
t2 = fzero(@(t) (HighIntensityC(l,t)-0.95),l);
swT3=t2-t1
```

```
function y = valveSwitchC(x,t)
    %Deal with problematic nonpositive t's
    t=t.*(t>0);
    t=t+(t≤0)*1e-50;

    y = 0.5*erfc((x-t)./(2*sqrt(t)));
```

```
function y = LowIntensityC(L,x,t)
    %Deal with problematic nonpositive t's
    t=t.*(t>0);
    t=t+(t≤0)*1e-50;
    %High Intensity Uncaging concentration
    y = quad(@(tau)(0.5*(erf((t-x-tau)./(2*sqrt(t-tau)))+...
        erf((L-t+x+tau)./(2*sqrt(t-tau))))),0,t)/L;
```

```
function y = HighIntensityC(x,t)
    %Deal with problematic nonpositive t's
    t=t.*(t>0);
    t=t+(t≤0)*1e-50;
    %High Intensity Uncaging concentration
    y = 0.5*exp(x/2).*(exp(x/2).*erfc((x+t)./(2*sqrt(t)))+...
        exp(-x/2).*erfc((x-t)./(2*sqrt(t))));
```

APPENDIX C

CALCULATION OF THE FLOW PROFILE IN A HEXAGONAL FLATTENING CHANNEL

The code for two C language programs is listed in this appendix. The first program uses Jacobi's relaxation method to solve Poisson's equation to give us the height of the channel. The second program takes this height information, and calculates the velocity field.

Both programs require the file *chamber.txt*. This is a text file containing a 300×101 pixel image of the geometry. Values along a row are separated by tabs (\t), and successive rows are separated by the new line character (\n). The values range from 0 to 9, with 0 corresponding to the exterior, 9 corresponding to the interior, and 1-8 corresponding to each of the boundaries shown in figure C.1.

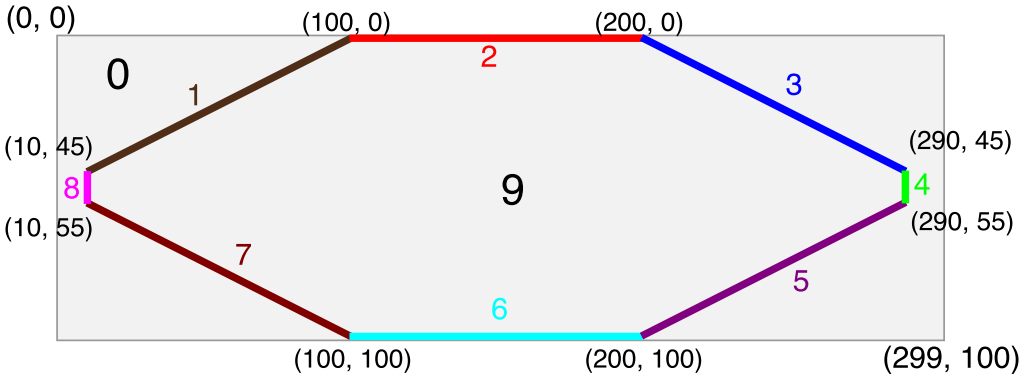

Figure C.1: Boundary conditions for flattening chamber flow calculations.

```c
/* ------------------------------
   --- Poisson equation solver ---
   ------------------------------ */
// Solves the poisson equation using
// the Jacobi relaxation method
// AJB, 07 October 2010

#include <stdio.h>
#include <string.h>
#include <math.h>

// Define the size of the grid
#define M 300
#define N 101

// 100 pixels is 2 mm
#define dx 0.02

// Basically the diffusion coefficient (pix^2/step).  Setting
// it high will speed up the computation, but can be unstable.
#define Δ  0.2

// The mean curvature (1/mm) ... or half of the inhomogeneous
// term in the Poisson equation.
#define H   0.0125

// The height of the unflattened channel (mm)
#define a0  0.0140

int main() {
    int geoGrid[M][N];
    double f[M][N];
    double fOld[M][N];
    double df;

    int i, j, t;

    FILE *fin;
    FILE *fout;
    char fname[100];

    // Let's read in the geometry, and
    // also initialize the other grids
    fin=fopen("chamber.txt", "r");
    if(!fin) {
        fprintf(stderr, "Geometry file not found\n");
        return 0;
    }
    for(j=0;j<N;++j) {
        for(i=0;i<M;++i) {
            fscanf(fin,"%d", &(geoGrid[i][j]));
            f[i][j]=0;
```

```
53              fOld[i][j]=0;
54          }
55      }
56      fclose(fin);
57
58      // We are ready to start solving
59      for(t=0;t≤100000;++t) {
60          // Step through the grid
61          for(j=0;j<N;++j) {
62              for(i=0;i<M;++i) {
63                  // look for interior points
64                  if(geoGrid[i][j]==9) {
65                      df=Δ*(fOld[i-1][j]+fOld[i+1][j]
66                              +fOld[i][j-1]+fOld[i][j+1]
67                              -4*fOld[i][j]-2*H*dx*dx);
68                      f[i][j]=fOld[i][j]+df;
69                  }
70              }
71          }
72          // Make a copy
73          for(j=0;j<N;++j) {
74              for(i=0;i<M;++i) {
75                      fOld[i][j]=f[i][j];
76              }
77          }
78
79          if(t%10000==0) {
80              printf("Saving data.\n");
81              sprintf(fname,"height%.2d.txt",t/10000);
82              fout=fopen(fname,"w");
83              for(j=0;j<N;++j) {
84                  for(i=0;i<M;++i) {
85                      fprintf(fout, "%le", a0+f[i][j]);
86                      if(i<M-1)
87                          fprintf(fout, "\t");
88                      else
89                          fprintf(fout, "\n");
90                  }
91              }
92              fclose(fout);
93          }
94      }
95
96      return 0;
97  }
```

```c
/* ------------------------------
   --- Pressure equation solver ---
   ------------------------------ */
// Solves the pressure equation using
// the Jacobi relaxation method
// AJB, 07 October 2010

#include <stdio.h>
#include <string.h>
#include <math.h>

// Define the size of the grid
#define M 300
#define N 101

// Basically the diffusion coefficient (pix^2/step).  Setting
// it high will speed up the computation, but can be unstable.
#define Δ  0.2

// The rate at which the boundary adjusts
#define Δ2 0.5

#define nx  0.4472
#define ny  0.8944

int main() {
    // geometry grid
    int geoGrid[M][N];

    // height grid
    double a[M][N];

    // 3 a^-1 da/dx
    double bx[M][N];
    // 3 a^-1 da/dy
    double by[M][N];

    double p[M][N];
    double pOld[M][N];
    double dp;

    int i, j, t;

    FILE *fin;
    FILE *fout;
    char fname[100];

    // Let's read in the geometry, and
    // also initialize the pressure grid
    fin=fopen("chamber.txt", "r");
    if(!fin) {
        fprintf(stderr, "Geometry file not found\n");
```

```
53          return 0;
54      }
55      for(j=0;j<N;++j) {
56          for(i=0;i<M;++i) {
57              fscanf(fin,"%d", &(geoGrid[i][j]));
58              p[i][j]=0;
59              pOld[i][j]=0;
60          }
61      }
62      fclose(fin);
63
64      // Next, let's read in the height grid
65      fin=fopen("height10.txt", "r");
66      if(!fin) {
67          fprintf(stderr, "Height file not found.\n");
68          return 0;
69      }
70      for(j=0;j<N;++j) {
71          for(i=0;i<M;++i) {
72              fscanf(fin,"%le", &(a[i][j]));
73          }
74      }
75      fclose(fin);
76
77      // Calculate the derivatives
78      for(j=0;j<N;++j) {
79          for(i=0;i<M;++i) {
80              // x-derivative
81              if(i==0)
82                  bx[i][j]=3*(a[i+1][j]-a[i][j])/a[i][j];
83              else if(i==M-1)
84                  bx[i][j]=3*(a[i][j]-a[i-1][j])/a[i][j];
85              else
86                  bx[i][j]=1.5*(a[i+1][j]-a[i-1][j])/a[i][j];
87
88              // y-derivative
89              if(j==0)
90                  by[i][j]=3*(a[i][j+1]-a[i][j])/a[i][j];
91              else if(j==N-1)
92                  by[i][j]=3*(a[i][j]-a[i][j-1])/a[i][j];
93              else
94                  by[i][j]=1.5*(a[i][j+1]-a[i][j-1])/a[i][j];
95          }
96      }
97      fclose(fin);
98
99
100     // We are ready to start solving
101     for(t=0;t≤400000;++t) {
102         // Step through the grid
103         for(j=0;j<N;++j) {
104             for(i=0;i<M;++i) {
```

```
                // look for boundary points
                if(geoGrid[i][j]==1) //left
                    p[i][j]=1.0;
                if(geoGrid[i][j]==2) //top-left
                    p[i][j]=pOld[i][j]+Δ2*
                                (nx*(pOld[i+1][j]-pOld[i][j])
                                +ny*(pOld[i][j+1]-pOld[i][j]));
                if(geoGrid[i][j]==3) //top
                    p[i][j]=pOld[i][j]+Δ2*
                                (pOld[i][j+1]-pOld[i][j]);
                if(geoGrid[i][j]==4) //top-right
                    p[i][j]=pOld[i][j]+Δ2*
                                (nx*(pOld[i-1][j]-pOld[i][j])
                                +ny*(pOld[i][j+1]-pOld[i][j]));
                if(geoGrid[i][j]==5) //right
                    p[i][j]=0.0;
                if(geoGrid[i][j]==6) //bottom-right
                    p[i][j]=pOld[i][j]+Δ2*
                                (nx*(pOld[i-1][j]-pOld[i][j])
                                +ny*(pOld[i][j-1]-pOld[i][j]));
                if(geoGrid[i][j]==7) //bottom
                    p[i][j]=pOld[i][j]+Δ2*
                                (pOld[i][j-1]-pOld[i][j]);
                if(geoGrid[i][j]==8) //bottom-left
                    p[i][j]=pOld[i][j]+Δ2*
                                (nx*(pOld[i+1][j]-pOld[i][j])
                                +ny*(pOld[i][j-1]-pOld[i][j]));
                // deal with the interior
                if(geoGrid[i][j]==9) {
                    dp=Δ*(pOld[i-1][j]+pOld[i+1][j]
                          +pOld[i][j-1]+pOld[i][j+1]-4*pOld[i][j]
                          +0.5*bx[i][j]*(pOld[i+1][j]-pOld[i-1][j])
                          +0.5*by[i][j]*(pOld[i][j+1]-pOld[i][j-1]));
                    p[i][j]=pOld[i][j]+dp;
                }
            }
        }
        // Make a copy
        for(j=0;j<N;++j) {
            for(i=0;i<M;++i) {
                    pOld[i][j]=p[i][j];
            }
        }

        if(t%20000==0) {
            printf("Saving data.\n");
            sprintf(fname,"pressure%.2d.txt",t/20000);
            fout=fopen(fname,"w");
            for(j=0;j<N;++j) {
                for(i=0;i<M;++i) {
                    fprintf(fout, "%le", p[i][j]);
                    if(i<M-1)
```

```
157                         fprintf(fout, "\t");
158                     else
159                         fprintf(fout, "\n");
160                 }
161             }
162             fclose(fout);
163 
164             sprintf(fname,"ux%.2d.txt",t/20000);
165             fout=fopen(fname,"w");
166             for(j=0;j<N;++j) {
167                 for(i=0;i<M;++i) {
168                     if(geoGrid[i][j]==9) {
169                         fprintf(fout, "%le", 0.04167
170                             *(p[i-1][j]-p[i+1][j])*a[i][j]*a[i][j]);
171                     }
172                     else {
173                         fprintf(fout, "%le",0.0);
174                     }
175                     if(i<M-1)
176                         fprintf(fout, "\t");
177                     else
178                         fprintf(fout, "\n");
179                 }
180             }
181             fclose(fout);
182 
183             sprintf(fname,"uy%.2d.txt",t/20000);
184             fout=fopen(fname,"w");
185             for(j=0;j<N;++j) {
186                 for(i=0;i<M;++i) {
187                     if(geoGrid[i][j]==9) {
188                         fprintf(fout, "%le", 0.04167
189                             *(p[i][j-1]-p[i][j+1])*a[i][j]*a[i][j]);
190                     }
191                     else {
192                         fprintf(fout, "%le",0.0);
193                     }
194                     if(i<M-1)
195                         fprintf(fout, "\t");
196                     else
197                         fprintf(fout, "\n");
198                 }
199             }
200             fclose(fout);
201 
202         }
203     }
204 
205     return 0;
206 }
```

BIBLIOGRAPHY

[1] M. Abercrombie, J. E. M. Heaysman, and S. M. Pegrum. The locomotion of fibroblasts in culture. III Movements of particles on the dorsal surface of the leading lamella. *Exp. Cell. Res.*, 62:389–98, 1970.

[2] M. A. Allessie, F. I. Bonke, and F. J. Schopman. Circus movement in rabbit atrial muscle as a mechanism of tachycardia. *Circ. Res.*, 41:9–18, 1977.

[3] M. Almagor, A. Ron, and J. Bartana. Chemotaxis in *Tetrahymena thermophila*. *Cell Motility and the Cytoskeleton*, 1(2):261–268, 1981.

[4] G. Amselem. *Directional sensing and chemotaxis in eukaryotic cells*. PhD dissertation, Georg August Universität Göttingen, 2010.

[5] N. Andrew and R. H. Insall. Chemotaxis in shallow gradients is mediated independently of PtdIns 3-kinase by biased choices between random protrusions. *Nature Cell Biology*, 9(2):193–U91, February 2007.

[6] B. W. Andrews and P. A. Iglesias. An information-theoretic characterization of the optimal gradient sensing response of cells. *PLoS Computational Biology*, 3:e153, 2007.

[7] R. Aris. On the dispersion of a solute in a fluid flowing through a tube. *Proc. Roy. Soc. Lond. A*, 235:67, 1956.

[8] J. E. Avron, O. Kenneth, and D. H. Oaknin. Pushmepullyou: an efficient micro-swimmer. *New Journal of Physics*, 7:234, 2005.

[9] K. Bacia, S. A. Kim, and P. Schwille. Fluorescence cross-correlation spectroscopy in living cells. *Nature Methods*, 3:83–9, 2006.

[10] A. J. Bae, C. Beta, and E. Bodenschatz. Rapid switching of chemical signals in microfluidic devices. *Lab Chip*, 9:3059–3065, 2009.

[11] A. J. Bae and E. Bodenschatz. On the swimming of *Dictyostelium* amoebae. *Proc. Natl. Acad. Sci.*, 107:E165–6, 2010.

[12] A. Bagorda, S. Das, E. C. Rericha, D. Chen, J. Davidson, and C. A. Parent. Real-time measurements of camp production in live *Dictyostelium* cells. *Journal of Cell Science*, 122:3907, 2009.

[13] N. P. Barry and M. S. Bretscher. Dictyostelium amoebae and neutrophils can swim. *Proc. Natl. Acad. Sci.*, 107:11376–80, 2010.

[14] D. A. Beard. Taylor dispersion of a solute in a microfluidic channel. *J. Appl. Phys.*, 89:4667, 2001.

[15] M. Benoit, D. Gabriel, G. Gerish, and H. E. Gaub. Discrete interactions in cell adhesion measured by single-molecule force spectroscopy. *Nature Cell Biology*, 2:313–7, 2000.

[16] H. C. Berg. Symmetries in bacterial motility. *Proc. Natl. Acad. Sci.*, 93:14225–8, 1996.

[17] H. C. Berg and E. M. Purcell. Physics of chemoreception. *Biophys J*, 20(2):193–219, 1977.

[18] H.C. Berg. *Random walks in biology*. Princeton University Press, 1993.

[19] H.C. Berg. *E. Coli in motion*. Springer, 2004.

[20] C. Beta, G. Amselem, and E. Bodenschatz. A bistable mechanism for directional sensing. *New Journal of Physics*, 10:083015, 2008.

[21] C. Beta, D. Wyatt, W.-J. Rappel, and E. Bodenschatz. Flow photolysis for spatiotemporal stimulation of single cells. *Analytical Chemistry*, 79:3940–3944, 2007.

[22] H. Beug, F. E. Katz, A. Stein, and G. Gerisch. Quantitation of membrane sites in aggregating *Dictyostelium* cells by use of tritiated univalent antibody. *Proc. Natl. Acad. Sci.*, 70:3150–4, 1973.

[23] J. G. Black. *Microbiology*. Prentice Hall, 4th edition, 1999.

[24] N Blackburn and T Fenchel. Modelling of microscale patch encounter by chemotactic protozoa. *Protist*, 150(3):337–343, October 1999.

[25] J. T. Bonner. Evidence for the formation of cell aggregates by chemotaxis in the development of the slime mold Dictyostelium discoideum. *J. Exp. Zool.*, 106:1–26, 1947.

[26] J. T. Bonner, W. W. Clarke, C. L. Neeley, and M. K. Slifkin. The orientation to light and the extremely sensitive orientation to temperature gradients

in the slime mold *Dictyostelium discoideum*. *Journal of Cellular and Comparative Physiology*, 36:149–58, 1950.

[27] J. T. Bonner and D. S. Lamont. Behavior of cellular slime molds in the soil. *Mycologia*, 97:178–84, 2005.

[28] J.T. Bonner. A note on the number of cells in a slug of *Dictyostelium discoideum*. Retrieved from http://dictybase.org/Bonner%20paper.pdf.

[29] Å. Brämmström and U. Dieckmann. Evolutionary dynamics of altruism and cheating among social amoebas. *Proc. Roy. Soc. B*, 272:1609–16, 2005.

[30] M. S. Bretscher. Endocytosis - relation to capping and cell locomotion. *Science*, 224:681–6, 1984.

[31] M. S. Bretscher. Getting membrane flow and the cytoskeleton to cooperate in moving cells. *Cell*, 87:601–6, 1996.

[32] G. Charras and E. Paluch. Blebs lead the way: how to migrate without lamellipodia. *Nature Reviews Molecular Cell Biology*, 9:730–6, 2008.

[33] L. Chen, M. Iijima, M. Tang, M. A. Landree, Y. E. Huang, Y. Xiong, P. A. Iglesias, and P. N. Devreotes. PLA_2 and PI3K/PTEN pathways act in parallel to mediate chemotaxis. *Developmental Cell*, 12:603–14, 2007.

[34] R. L. Chisholm and R. A. Firtel. Insights into morphogenesis from a simple developmental system. *Nature Reviews Molecular Cell Biology*, 5:531–41, 2004.

[35] R. L. Chisholm, S. Hopkinson, and H. F. Lodish. Superinduction of the *Dictyostelium discoideum* cell surface cAMP receptor by pulses of cAMP. *Proc. Natl. Acad. Sci.*, 84:1030–4, 1987.

[36] R. A. F. Clark, editor. *The Molecular and Cellular Biology of Wound Repair*. Plenum Press, 2nd edition, 1996.

[37] P. A. Clow, T. Chen, R. L. Chisholm, and J. G. McNally. Three-dimensional in vivo analysis of dictyostelium mounds reveals directional sorting of prestalk cells and defines a role for the myosin ii regulatory light chain in prestalk cell sorting and tip protrusion. *Development*, 127:2715–28, 2000.

[38] J. C. Coates and A. J. Harwood. Cell-cell adhesion and signal transduction during dictyostelium development. *Journal of Cell Science*, 114:4349–58, 2001.

[39] C. T. Culbertson, S. C. Jacobson, and J. M. Ramsey. Diffusion coefficient measurements in microfluidic devices. *Talanta*, 56:365–373, 2002.

[40] J. Dalous, E. Burghardt, A. Müller-Taubenberger, F. Bruckert, G. Gerisch, and T. Bretschneider. Reversal of cell polarity and actin-myosin cytoskeleton reorganization under mechanical and chemical stimulation. *Biophys J*, 94:1063–1074, 2008.

[41] J. Davies. *Mechanisms of Morphogenesis*. Academic Press, 2005.

[42] É. Debreuve. Active contour toolbox. Retrieved from http://www.i3s.unice.fr/∼debreuve/code.php.

[43] E. Décavé, D. Garrivier, Y. Bréchet, B. Fourcade, and F. Bruckert. Shear flow-induced detachment kinetics of *Dictyostelium discoideum* cells from solid substrate. *Biophys J*, 82(2383-2395), 2002.

[44] P. Devreotes and C. Janetopoulos. Eukaryotic chemotaxis: Distinctions between directional sensing and polarization. *Journal of Biological Chemistry*, 278(23):20445–20448, June 2003.

[45] P. N. Devreotes. Chemotaxis. In W. F. Loomis, editor, *The development of Dictyostelium discoideum*. Academic Press, 1982.

[46] P. N. Devreotes and S. H. Zigmond. Chemotaxis in eukaryotic cells. *Annual Review of Cell Biology*, 4:649–686, 1988.

[47] K. D. Dorfman and H. Brenner. Comment on "Taylor dispersion of a solute in a microfluidic channel". *J. Appl. Phys.*, 90:6553, 2001.

[48] D. Dormann, G. Weijer, C. A. Parent, P. N. Devreotes, and C. J. Weijer. Visualizing PI3 kinase-mediated cell-cell signaling during *Dictyostelium* development. *Current Biology*, 12:1178, 2002.

[49] M. R. Doshi, P. M. Daiyas, and W. N. Gill. Three dimensional laminar dispersion in open and closed rectangular conduits. *Chemical Engineering Science*, 33:795–804, 1978.

[50] D. B. Dusenbery. Spatial sensing of stimulus gradients can be superior to temporal sensing for free-swimming bacteria. *Biophys J*, 74(5):2272–2277, May 1998.

[51] M. Dworkin and K. H. Keller. Solubility and diffusion coefficient of adenosine 3':5'-monophosphate. *Journal of Biological Chemistry*, 252:864–5, 1977.

[52] J. L. Dynes, A. M. Clark, G. Shaulsky, A. Kuspa, W. F. Loomis, and R. A. Firtel. LagC is required for cell-cell interactions that are essential for cell-type differentiation in *Dictyostelium*. *Genes & Development*, 8:948, 1994.

[53] A. Early, T. Abe, and J. Williams. Evidence for positional differentiation of prestalk cells and for a morphogenetic gradient in dictyostelium. *Cell*, 83:91–9, 1995.

[54] L. Eichinger, J. A. Pachebat, G. Glockner et al. The genome of the social amoeba *Dictyostelium discoideum*. *Nature*, 435(7038):43–57, May 2005.

[55] T. Fenchel. Microbial behavior in a heterogeneous world. *Science*, 296(5570):1068–1071, May 2002.

[56] P. Fey, A. S. Kowal, P. Gaudet, K. E. Pilcher, and R. L. Chisholm. Protocols for growth and development of *Dictyostelium discoideum*. *Nature Protocols*, 2:1307–16, 2007.

[57] P. R. Fisher, R. Merkl, and G. Gerisch. Quantitative-analysis of cell motility and chemotaxis in *Dictyostelium discoideum* by using an image processing system and a novel chemotaxis chamber providing stationary chemical gradients. *Journal of Cell Biology*, 108(3):973–984, March 1989.

[58] P. R. Fisher, E. Smith, and K. L. Williams. An extracellular chemical signal controlling phototactic behaviour by *D. discoideum* slugs. *Cell*, 23:799–807, 1981.

[59] D. A. Fletcher and R. D. Mullins. Cell mechanics and the cytoskeleton. *Nature*, 463:485–92, 2010.

[60] D. A. Fletcher and J. A. Theriot. Introduction to cell motility for the physical scientist. *Phys. Biol.*, 1:T1, 2004.

[61] C. Franck, W. Ip, A. Bae, N. Franck, E. Bogart, and T. Thi Le. Contact-mediated cell-assisted cell proliferation in a model eukaryotic single-cell organism: An explanation for the lag phase in shaken cell culture. *Physical Review E*, 77:041905, 2008.

[62] J. Franke and R. Kessin. A defined minimal medium for axenic strains of *Dictyostelium discoideum*. *Proc. Natl. Acad. Sci.*, 74:2157–61, 1977.

[63] H. Freeze and W. F. Loomis. Isolation and characterization of a component of the surface sheath of *Dictyostelium discoideum*. *Journal of Biological Chemistry*, 252:820–4, 1977.

[64] D. Fuller, W. Chen, M. Adler, and A. Groisman. External and internal constraints on eukaryotic chemotaxis. *Proc. Natl. Acad. Sci.*, 107:9656–59, 2010.

[65] S. Funamoto, R. Meili, S. Lee, L. Parry, and R. A. Firtel. Spatial and temporal regulation of 3-phosphoinositides by PI 3-kinase and PTEN mediates chemotaxis. *Cell*, 109(5):611–623, May 2002.

[66] A. Gamba, A. de Candia, S. Di Talia, A. Coniglio, A. Bussolino, and G. Serini. Diffusion-limited phase separation in eukaryotic chemotaxis. *Proc. Natl. Acad. Sci.*, pages 16927–32, 2005.

[67] A. Gamba, I. Kolokolov, V. Lebedev, and G. Ortenzi. Patch coalescence as a mechanism for eukaryotic directional sensing. *Physical Review Letters*, 99:158101, 2007.

[68] A. Gamba, I. Kolokolov, V. Lebedev, and G. Ortenzi. Universal features of cell polarization. *J. Stat. Mech. Theor. Exp.*, 2009:P02019, 2009.

[69] Jeffrey S. Garanich, Rishi A. Mathura, Zhong-Dong Shi, and John M. Tarbell. Effects of fluid shear stress on adventitial fibroblast migration. *Am J Physiol Heart Circ Physiol*, 292:H3128, 2007.

[70] Garland Science. Swimming eutreptiella. [video]. Retrieved from http://www.youtube.com/watch?v=hbsBAKaycJ8.

[71] G. Gerisch, D. Hulser, D. Malchow, and U. Wick. Cell communication by periodic cyclic-amp pulses. *Philosophical Transactions of the Royal Society of London Series B-Biological Sciences*, 272(915):181–&, 1975.

[72] A. Gholami, M. Falcke, and E. Frey. Velocity oscillations in actin-based motility. *New Journal of Physics*, 10:1–12, 2008.

[73] A. Gierer and H. Meinhardt. Theory of biological pattern formation. *Kybernetik*, 12(1):30–39, 1972.

[74] R. H. Gomer and R. A. Firtel. Cell-autonomous determination of cell-type choice in *Dictyostelium* development by cell-cycle phase. *Science*, 237:758–62, 1987.

[75] F. Graner. Can surface adhesion drive cell rearrangement? *J Theor Biol*, 164:455–76, 1993.

[76] O. Hazeki, T. Okada, H. Kurosu, S. Takasuga, T. Suzuki, and T. Katada. Activation of PI-3-kinase by G protein betagamma subunits. *Life Sci.*, 62:1555–9, 1998.

[77] J. P. Heath and B. F. Holifield. Cell locomotion: New research tests old ideas on membrane and cytoskeletal flow. *Cell Motility and the Cytoskeleton*, 18:245–57, 1991.

[78] H. S. Hele-Shaw. The flow of water. *Nature*, 58:34–6, 1898.

[79] P. Herzmark, K. Campbell, F. Wang, K. Wong, H. El-Samad, A. Groisman, and H. R. Bourne. Bound attractant at the leading vs. the trailing edge determines chemotactic prowess. *Proc. Natl. Acad. Sci.*, 104:13349–13354, 2007.

[80] O. Hoeller and R. R. Kay. Chemotaxis in the absence of PIP3 gradients. *Current Biology*, 17:813–7, 2007.

[81] T. Höfer, P. K. Maini, J. A. Sherratt, M. A. J. Chaplain, and J. D. Murray. Resolving the chemotactic wave paradox: A mathematical model for chemotaxis of *Dictyostelium* amoebae. *Journal of Biological Systems*, 3:967–73, 1995.

[82] M. S. Hutson, G. W. Brodland, J. Yang, and D. Viens. Cell sorting in three dimensions. *Physical Review Letters*, 101:148105, 2008.

[83] P. A. Iglesias and A. Levchenko. Modeling the cell's guidance system. *Science STKE*, 2002:re12, 2002.

[84] M. Iijima, Y. E. Huang, and P. Devreotes. Temporal and spatial regulation of chemotaxis. *Developmental Cell*, 3(4):469–478, October 2002.

[85] N. Iranfar, D. Fuller, and W. F. Loomis. Genome-wide expression analysis of gene regulation during early development of *Dictyostelium discoideum*. *Eukaryotic Cell*, 2:664–70, 2003.

[86] D. Irimia, S.-Y. Liu, W. G. Tharp, A. Samadani, M. Toner, and M. C. Poznansky. Microfluidic system for measuring neutrophil migratory responses to fast switches of chemical gradients. *Lab Chip*, 6:191–198, 2006.

[87] C. Janetopoulos, T. Jin, and P. Devreotes. Receptor-mediated activation of heterotrimeric g-proteins in living cells. *Science*, 291(5512):2408–2411, March 2001.

[88] C. Janetopoulos, L. Ma, P. N. Devreotes, and P. A. Iglesias. Chemoattractant-induced phosphatidylinositol 3,4,5-trisphosphate accumulation is spatially amplified and adapts, independent of the actin cytoskeleton. *Proc. Natl. Acad. Sci.*, 101(24):8951–8956, June 2004.

[89] K. A. Jermyn and J. G. Williams. An analysis of culmination in *Dictyostelium* using prestalk and stalk-specific cell autonomous markers. *Development*, 111:779–87, 1991.

[90] Y. Jiang, H. Levine, and J. Glazier. Differential adhesion and chemotaxis in mound formation of *Dictyostelium*. *Biophys J*, 75:2615, 1998.

[91] T. Jin, N. Zhang, Y. Long, C. A. Parent, and P. N. Devreotes. Localization of the G protein beta gamma complex in living cells during chemotaxis. *Science*, 287(5455):1034–1036, February 2000.

[92] R. L. Johnson, C. L. Saxe, R. Gollop, A. R. Kimmel, and P. N. Devreotes. Identification and targeted gene disruption of cAR3, a cAMP receptor subtype expressed during multicellular stages of *Dictyostelium* development. *Genes & Development*, 7(2):273–282, February 1993.

[93] R. L. Johnson, R. A. Vaughan, M. J. Caterina, P. J. Van Haastert, and P. N. Devreotes. Overexpression of the cAMP receptor-1 in growing *Dictyostelium* cells. *Biochemistry*, 30(28):6982–6986, July 1991.

[94] D. Kaiser. Control of multicellular development: *Dictyostelium* and *Myxococcus*. *Annual Review of Genetics*, 20:539–66, 1986.

[95] H. E. Kaiser and A. Nasir, editors. *Selected Aspects of Cancer Progression: Metastasis, Apoptosis and Immune Response*. Springer, 2008.

[96] Y. Kamimura, Y. Xiong, P. A. Iglesias, O. Hoeller, P. Bolourani, and P. N. Devreotes. PIP3-independent activation of TorC2 and PKB at the cell's leading edge mediates chemotaxis. *Current Biology*, 18:1034–43, 2008.

[97] J. M. Kavran, D. E. Klein, A. Lee, M. Falasca, S. J. Isakoff, E. Y. Skolnik, and M. A. Lemmon. Specificity and promiscuity in phosphoinositide binding by pleckstrin homology domains. *Journal of Biological Chemistry*, 273(46):30497–30508, November 1998.

[98] R. R. Kay, P. Langridge, D. Traynor, and O. Hoeller. Changing directions in the study of chemotaxis. *Nature Reviews Molecular Cell Biology*, 9:455–63, 2008.

[99] R. R. Kay and C. R. Thompson. Forming patterns in development without morphogen gradients. *Cold Spring Harb Perspect Biol*, 1:a001503, 2009.

[100] R. H. Kessin. *Dictyostelium: evolution, cell biology, and the development of multicellularity*. Cambridge University Press, 2001.

[101] K. Kibler, J. Svetz, T.-L. Nguyen, C. Shaw, and G. Shaulsky. A cell-adhesion pathway regulates intercellular communication during *Dictyostelium* development. *Developmental Biology*, 264:506–21, 2003.

[102] A. R. Kimmel and C. A. Parent. *Dictyostelium discoideum* cAMP chemotaxis pathway. *Science STKE*, 2003:194, 2003.

[103] J. S. King and R. H. Insall. Chemotaxis: finding the way forward with *Dictyostelium*. *Trends in Cell Biology*, 19:523–30, 2009.

[104] K. R. King, S. Wang, A. Jayaraman, M. L. Yarmush, and M. Toner. Microfluidic flow-encoded switching for parallel control of dynamic cellular microenvironments. *Lab Chip*, 8:107–116, 2008.

[105] D. A. Knecht, D. L. Fuller, and W. F. Loomis. Surface glycoprotein, gp24, involved in early adhesion of *Dictyostelium discoideum*. *Developmental Biology*, 121:277–83, 1987.

[106] J. Krishnan and P. A. Iglesias. Analysis of the signal transduction properties of a module of spatial sensing in eukaryotic chemotaxis. *Bulletin of Mathematical Biology*, 65(1):95–128, January 2003.

[107] D. F. Kucik, E. L. Elson, and M. P. Sheetz. Cell migration does not produce membrane flow. *Journal of Cell Biology*, 111:1617–22, 1990.

[108] B. Kuczenski, P. R. LeDuc, and W. C. Messner. Pressure-driven spatiotemporal control of the laminar flow interface in a microfluidic network. *Lab Chip*, 7:647–649, 2007.

[109] B. Kuczenski, W. C. Ruder, W. C. Messner, and P. R. LeDuc. Probing cellular dynamics with a chemical signal generator. *PLoS ONE*, 4:e4847, 2009.

[110] J. Lee, M. Gustafsson, K.-E. Magnusson, and K. Jacobson. The direction of membrane lipid flow in locomoting polymorphonuclear leukocytes. *Science*, 247:1229–33, 1990.

[111] A. Levchenko and P. A. Iglesias. Models of eukaryotic gradient sensing: Application to chemotaxis of amoebae and neutrophils. *Biophys J*, 82(1):50–63, January 2002.

[112] H. Levine, D. A. Kessler, and W.-J. Rappel. Directional sensing in eukaryotic chemotaxis: A balanced inactivation model. *Proc. Natl. Acad. Sci.*, 103(26):9761–9766, June 2006.

[113] Y.-S. J. Li, J. H. Haga, and S. Chien. Molecular basis of the effects of shear stress on vascular endothelial cells. *Journal of Biomechanics*, 38:1949, 2005.

[114] J. M. Louis, G. T. Ginsburg, and A. R. Kimmel. The cAMP receptor cAR4 regulates axial patterning and cellular differentiation during late development of *Dictyostelium*. *Genes & Development*, 8(17):2086–2096, September 1994.

[115] W. Ludwig. Zur Theorie der Flimmerbewegung. *Z. f. vergl. Physiol.*, 13:397–504, 1930.

[116] L. Ma, C. Janetopoulos, L. Yang, P. N. Devreotes, and P. A. Iglesias. Two complementary, local excitation, global inhibition mechanisms acting in parallel can explain the chemoattractant-induced regulation of PI(3,4,5)P-3 response in *Dictyostelium* cells. *Biophys J*, 87(6):3764–3774, December 2004.

[117] A. F. M. Marée and P. Hogeweg. Modelling *Dictyostelium discoideum* morphogenesis: the culmination. *Bulletin of Mathematical Biology*, 64:327–53, 2002.

[118] A. F. M. Marée, A. V. Panfilov, and P. Hogeweg. Migration and thermotaxis of *Dictyostelium discoideum* slugs, a model study. *J Theor Biol*, 199:297, 1999.

[119] M. Massabó, R. Cianci, and O. Paladino. Some analytical solutions for two-dimensional convection—dispersion equation in cylindrical geometry. *Environmental Modelling & Software*, 21:681, 2006.

[120] J. M. Mato, A. Losada, V. Nanjundiah, and T. M. Konijn. Signal input for a chemotactic response in cellular slime-mold dictyostelium-discoideum. *Proc. Natl. Acad. Sci.*, 72(12):4991–4993, 1975.

[121] R. Meili, C. Ellsworth, S. Lee, T. B. K. Reddy, H. Ma, and R. A. Firtel. Chemoattractant-mediated transient activation and membrane localization of Akt/PKB is required for efficient chemotaxis to cAMP in *Dictyostelium*. *The EMBO Journal*, 18(8), 2092-105 1999.

[122] H. Meinhardt. Orientation of chemotactic cells and growth cones: models and mechanisms. *Journal of Cell Science*, 112(17):2867–2874, September 1999.

[123] T. J. Mitchison and L. P. Cramer. Actin-based cell motility and cell locomotion. *Cell*, 84:371–9, 1996.

[124] A. Mogilner. Mathematics of cell motility: have we got its number? *J. Math. Biol.*, 58:105–34, 2009.

[125] Y. Mori, A. Jilkine, and L. Edelstein-Keshet. Wave-pinning and cell polarity from a bistable reaction-diffusion system. *Biophys J*, 94:3684–97, 2008.

[126] K. Müller and G. Gerisch. A specific glycoprotein as the target site of adhesion blocking fab in aggregating *Dictyostelium* cells. *Nature*, 274:445–9, 1978.

[127] K.P. Murphy, K.M. Murphy, P. Travers, M. Walport, and C. Janeway. *Janeway's immunobiology*. Garland Science, 7th edition, 2008.

[128] S. Nadkarni. Protocols for fabrication of microfluidic devices. June 2004.

[129] A. Narang, K. K. Subramanian, and D. A. Lauffenburger. A mathematical model for chemoattractant gradient sensing based on receptor-regulated membrane phospholipid signaling dynamics. *Annals of Biomedical Engineering*, 29(8):677–691, August 2001.

[130] P. C. Newell, A. Telser, and M. Sussman. Alternative developmental pathways determined by environmental conditions in the cellular slime mold *Dictyostelium discoideum*. *J. Bacteriol.*, 100:763, 1969.

[131] A. Nicol, W. Rappel, H. Levine, and W. F. Loomis. Cell-sorting in aggregates of dictyostelium discoideum. *Journal of Cell Science*, 112:3923–9, 1999.

[132] N. Oikawa, A. Bae, G. Amselem, and E. Bodenschatz. The relation between the onset of synchronization and signaling patterns mediated by diffusion. *In preparation*, 2010.

[133] C. A. Parent and P. N. Devreotes. Molecular genetics of signal transduction in *Dictyostelium*. *Annual Review of Biochemistry*, 65:411–440, 1996.

[134] C. A. Parent and P. N. Devreotes. A cell's sense of direction. *Science*, 284(5415):765–70, Apr 1999.

[135] H. Patel, K. Guo, C. Parent, J. Gross, P. N. Devreotes, and C. J. Weijer. A temperature-sensitive adenylyl cyclase mutant of *Dictyostelium*. *The EMBO Journal*, 19:2247–56, 2000.

[136] C. S. Peskin, G. M. Odell, and G. F. Oster. Cellular motions and thermal fluctuations: the brownian ratchet. *Biophys J*, 65:316–24, 1993.

[137] L. M. Pierini, M. A. Lawson, R. J. Eddy, B. Hendey, and F. R. Maxfield. Oriented endocytic recycling of alpha5beta1 in motile neutrophils. *Blood*, 95:2471–80, 2000.

[138] M. Postma, J. Roelofs, J. Goedhart, T. W. J. Gadella, A. J. W. G. Visser, and P. J. M. Van Haastert. Uniform camp stimulation of dictyostelium cells induces localized patches of signal transduction and pseudopodia. *Mol Biol Cell*, 14(12):5019–27, Dec 2003.

[139] M. Postma, J. Roelofs, J. Goedhart, H. M. Loovers, A. J. W. G. Visser, and P. J. M. Van Haastert. Sensitization of dictyostelium chemotaxis by

phosphoinositide-3-kinase-mediated self-organizing signalling patches. *J Cell Sci*, 117(Pt 14):2925–35, Jun 2004.

[140] M. Postma and P. J. Van Haastert. A diffusion-translocation model for gradient sensing by chemotactic cells. *Biophys J*, 81(3):1314–23, Sep 2001.

[141] L. M. Prescott, J. P. Harley, and D. A. Klein. *Microbiology*. McGraw Hill, 6th edition, 2005.

[142] W. H. Press, S. A. Teukolsky, W. T. Vetterling, and B. P. Flannery. *Numerical Recipes in C*. Cambridge University Press, 2nd edition, 1988.

[143] E. M. Purcell. Life at low Reynolds number. *Am. J. Phys.*, 45:3–11, 1977.

[144] I. Ràfols, Y. Sawada, A. Amagai, Y. Maeda, and H. K. MacWilliams. Cell type proportioning in *Dictyostelium* slugs: lack of regulation within a 2.5-fold tolerance range. *Differentiation*, 67:107–16, 2001.

[145] K. B. Raper. Pseudoplasmodium formation and organization in *Dictyostelium discoideum*. *Journal of the Elisha Mitchell Scientific Society*, 56:241–82, 1940.

[146] W.-J. Rappel. Personal communication. 28 July 2006.

[147] W.-J. Rappel and H. Levine. Receptor noise limitations on chemotactic sensing. *Proc. Natl. Acad. Sci.*, 105:19270–5, 2008.

[148] W.-J. Rappel, A. Nicol, and H. Levine. Self-organized vortex state in two-dimensional dictyostelium dynamics. *Physical Review Letters*, 83:1247–50, 1999.

[149] W.-J. Rappel, P. J. Thomas, H. Levine, and W. F. Loomis. Establishing direction during chemotaxis in eukaryotic cells. *Biophys J*, 83(3):1361–7, Sep 2002.

[150] W. L. Robb. Thin silicone membranes-their permeation properties and some applications. *Annals of the New York Acadamy of Sciences*, 146:119–37, 1968.

[151] J. Roelofs, J. Meima, P. Schaap, and P. J. M. Van Haastert. The *Dictyostelium* homologue of mammalian soluble adenylyl cyclase encodes a guanylyl cyclase. *EMBO Journal*, 20:4341–8, 2001.

[152] A. Samadani, J. Mettetal, and A. van Oudenaarden. Cellular asymmetry and individuality in directional sensing. *Proc. Natl. Acad. Sci.*, 103(31):11549–54, Aug 2006.

[153] A. T. Sasaki, C. Chun, K. Takeda, and R. A. Firtel. Localized Ras signaling at the leading edge regulates PI3K, cell polarity, and directional cell movement. *Journal of Cell Biology*, 167:505–18, 2004.

[154] S. Sawai, X.-J. Guan, A. Kuspa, and E. C. Cox. High-throughput analysis of spatio-temporal dynamics in *Dictyostelium*. *Genome Biology*, 8:R144, 2007.

[155] S. Sawai, P. A. Thomason, and E. C. Cox. An autoregulatory circuit for long-range self-organization in *Dictyostelium* cell populations. *Nature*, 433:323–6, 2005.

[156] C. L. Saxe, 3rd, G. T. Ginsburg, J. M. Louis, R. Johnson, P. N. Devreotes, and A. R. Kimmel. CAR2, a prestalk cAMP receptor required for normal tip formation and late development of *Dictyostelium discoideum*. *Genes Dev*, 7(2):262–72, Feb 1993.

[157] I. C. Schneider and J. M. Haugh. Mechanisms of gradient sensing and chemotaxis: conserved pathways, diverse regulation. *Cell Cycle*, 5(11):1130–4, Jun 2006.

[158] J. E. Segall, S. M. Block, and H. C. Berg. Temporal comparisons in bacterial chemotaxis. *Proc. Natl. Acad. Sci.*, 83(23):8987–91, Dec 1986.

[159] A. Shapere and F. Wilczek. Geometry of self-propulsion at low Reynolds number. *J. Fluid Mech.*, 198:557–85, 1989.

[160] F. Siegert and C. J. Weijer. Spiral and concentric waves organize multicellular *Dictyostelium* mounds. *Current Biology*, 5:937–43, 1995.

[161] C.-H. Siu, B. Des Roches, and T. Y. Lam. Involvement of a cell-surface glycoprotein in the cell-sorting process of *Dictyostelium discoideum*. *Proc. Natl. Acad. Sci.*, 80:6596, 1983.

[162] M. K. Slifkin and J. T. Bonner. The effect of salts and organic solutes on the migration time of the slime mold *Dictyostelium discoideum*. *Biol. Bull.*, 102:273–7, 1952.

[163] D. R. Soll, D. Wessels, and A. Sylvester. The motile behavior of amoebae in the aggregation wave in *Dictyostelium discoideum*. In H. G. Othmer, P. K. Maini, and J. D. Murray, editors, *Experimental and Theoretical Advances in Biological Pattern Formation*. Plenum Press, 1993.

[164] L. Song, S. M. Nadkarni, H. U. Bödeker, C. Beta, A. Bae, C. Franck, W.-J. Rappel, W. F. Loomis, and E. Bodenschatz. *Dictyostelium discoideum* chemotaxis: Threshold for directed motion. *European Journal of Cell Biology*, 85:981–989, 2006.

[165] M. S. Steinberg. Reconstruction of tissues by dissociated cells. *Science*, 141:401–8, 1963.

[166] J. Sternfeld and J. T. Bonner. Cell differentiation in *Dictyostelium* under submerged conditions. *Proc. Natl. Acad. Sci.*, 74:268–71, 1977.

[167] H. Stone. Personal communication. 29 March 2010.

[168] K. K. Subramanian and A. Narang. A mechanistic model for eukaryotic gradient sensing: spontaneous and induced phosphoinositide polarization. *J Theor Biol*, 231:49–67, Nov 2004.

[169] R. R. Sussman and M. Sussman. Cultivation of *Dictyostelium discoideum* in axenic medium. *Biochem. Biophys. Res. Commun.*, 29:53–5, 1967.

[170] I. A. M. Swinnen, K. Bernaerts, E. J. J. Dens, A. H. Geeraerd, and J. F. Van Impe. Predictive modelling of the microbial lag phase: a review. *International Journal of Food Microbiology*, 94:137–159, 2004.

[171] G. I. Taylor. Analysis of the swimming of microscopic organisms. *Proc. Roy. Soc. A*, 209:447–61, 1951.

[172] G. I. Taylor. Dispersion of soluble matter in solvent flowing slowly through a tube. *Proc. Roy. Soc. Lond. A*, 219:186, 1953.

[173] R. B. Taylor, W. P. H. Duffus, M. C. Raff, and S. de Petris. Redistribution and pinocytosis of lymphocyte surface immunoglobilin modules induced by anti-immunoglobulin antibody. *Nature New Biology*, 233:225–9, 1971.

[174] R. Thar and M. Kuhl. Bacteria are not too small for spatial sensing of chemical gradients: an experimental evidence. *Proc. Natl. Acad. Sci.*, 100(10):5748–53, May 2003.

[175] J. A. Theriot and T. J. Mitchison. Actin microfilament dynamics in locomoting cells. *Nature*, 352:126–31, 1991.

[176] M. Theves. Quantitative study of eukaryotic chemotaxis with microfluidic devices. Diploma thesis, Georg August Universität Göttingen, 2009.

[177] C. R. Thompson, S. Reichelt, and R. R. Kay. A demonstration of pattern formation without positional information in dictyostelium. *Dev Growth Differ*, 46:363–9, 2004.

[178] K. J. Tomchik and P. N. Devreotes. Adenosine 3′,5′-monophosphate waves in *Dictyostelium discoideum*: a demonstration by isotope dilution–fluorography. *Science*, 222:443–6, 1981.

[179] D. Traynor and R. R. Kay. Possible roles of the endocytic cycle in cell motility. *Journal of Cell Science*, 120:2318–27, 2007.

[180] Y. Tu. Personal communication. 30 April 2010.

[181] A. M. Turing. The chemical basis of morphogenesis. *Phil. Trans. B*, 237:37–72, 1952.

[182] M. Ueda and S. Ogihara. Microtubules are required in amoeba chemotaxis for preferential stabilization of appropriate pseudopods. *J Cell Sci*, 107:2071–9, Aug 1994.

[183] M. Ueda and T. Shibata. Stochastic signal processing and transduction in chemotaxic response of eukaryotic cells. *Biophys J*, 93:11–20, 2007.

[184] T. Umeda and K. Inouye. Cell sorting by differential cell motility. *J Theor Biol*, 226:215, 2004.

[185] B. Van Duijn and P. J. Van Haastert. Independent control of locomotion and orientation during *Dictyostelium discoideum* chemotaxis. *J Cell Sci*, 102:763–8, Aug 1992.

[186] P. J. M. van Haastert and M. Postma. Biased random walk by stochastic fluctuations of chemoattractant-receptor interactions at the lower limit of detection. *Biophys J*, 93:1787–96, 2007.

[187] B. Vasiev and C. J. Weijer. Modeling chemotactic cell sorting during *Dictyostelium discoideum* mound formation. *Biophys J*, 76:595, 1999.

[188] B. Wang and A. Kuspa. *Dictyostelium* development in the absence of cAMP. *Science*, 277:251, 1997.

[189] D. J. Watts and J. M. Ashworth. Growth of myxamoebae of the cellular slime mould *Dictyostelium discoideum* in axenic culture. *Biochem J*, 119:171–4, 1970.

[190] I. Weber. Is there a pilot in a pseudopod? *Eur J Cell Biol*, 85(9-10):915–24, Sep 2006.

[191] C. J. Weijer. The cellular basis of *Dictyostelium* morphogenesis. In S. Nakanishi et al., editor, *Systems Biology*. Springer, 2009.

[192] C. J. Weijer, G. Duschl, and C. N. David. Dependence of cell-type proportioning and sorting on cell cycle phase in *Dictyostelium discoideum*. *J Cell Sci*, 70:133–45, 1984.

[193] C. Westendorf. Personal communication. 08 October 2010.

[194] C. Westendorf, A. J. Bae, C. Erlenkämper, E. Galland, C. Franck, and E. Bodenschatz. Live cell flattening – traditional and novel approaches. *PMC Biophysics*, 3:9, 2010.

[195] C. Westendorf, A. J. Bae, R. Sandmann, E. Bodenschatz, and C. Beta. The actin cytoskeleton forced with short time periodic stimuli in *Dictyostelium discoideum*. *In preparation*, 2010.

[196] B. D. Whitaker and K. L. Poff. Thermal adaptation of thermosensing and negative thermotaxis in *Dictyostelium*. *Experimental Cell Research*, 128:87–93, 1980.

[197] A. T. Winfree. Spiral waves of chemical activity. *Science*, 175:634–6, 1972.

[198] D. Wyatt. *Chemotaxis in Microfluid Channels*. PhD dissertation, Cornell University, 2007.

[199] Y. Xia and G. M. Whitesides. Soft lithography. *Angew. Chem. Int. Ed.*, 37:550–75, 1998.

[200] J. Xu, F. Wang, A. Van Keymeulen, M. Rentel, and H. R. Bourne. Neutrophil microtubules suppress polarity and enhance directional migration. *Proc. Natl. Acad. Sci.*, 102(19):6884–9, May 2005.

[201] X. Xu, T. Meckel, J. A. Brzostowski, J. Yan, and M. Meier-Schellerscheim. Coupling mechanism of a GPCR and a heterotrimeric G protein during chemotactic gradient sensing in *Dictyostelium*. *Science Signaling*, 3:ra71, 2010.

[202] X. Xu, M. Meier-Schellersheim, X. Jiao, L. E. Nelson, and T. Jin. Quantitative imaging of single live cells reveals spatiotemporal dynamics of multistep signaling events of chemoattractant gradient sensing in dictyostelium. *Mol Biol Cell*, 16(2):676–88, Feb 2005.

[203] K. Yoshida and T. Soldati. Dissection of amoeboid movement into two mechanically distinct modes. *Journal of Cell Science*, 119:3833–44, 2006.

[204] A. N. Zaikin and A. M. Zhabotinsky. Concentration wave propagation in two-dimensional liquid-phase self-oscillating system. *Nature*, 225:535–7, 1970.